THE UNIVERSITY OF CALGARY

THREE-DIMENSIONAL STRESS INVESTIGATION IN FIBER COMPOSITE MODELS

BY

DALJIT SINGH RATTAN

A THESIS

SUBMITTED TO THE FACULTY OF GRADUATE STUDIES

IN PARTIAL FULFILLMENT OF THE REQUIREMENTS FOR THE

DEGREE OF MASTER OF SCIENCE

DEPARTMENT OF MECHANICAL ENGINEERING

CALGARY, ALBERTA

AUGUST, 1988

ISBN 0-315-46634-0

THE UNIVERSITY OF CALGARY

FACULTY OF GRADUATE STUDIES

The undersigned certify that they have read, and recommend to the Faculty of Graduate Studies for acceptance, a thesis entitled, "Three-Dimensional Stress Investigation In Fiber Composite Models", submitted by Daljit Singh Rattan in partial fulfillment of the requirements for the degree of Master of Science in Mechanical Engineering.

WJD Shaw

Chairman, Dr. W.J.D. Shaw
Department of Mechanical Engineering

E.W. Johnson

Dr. E.W. Johnson
Department of Mechanical Engineering

Dr. I. Le May
Department of Mechanical Engineering

R.L. Day

Dr. R.L. Day
Department of Civil Engineering

Date August 30, 1988

ABSTRACT

A three-dimensional stress investigation in fiber composite models was carried out. Photoelastic composite models with E_f/E_m of 26 were cast to simulate the behaviour of the graphite fiber composite AS4/3501-6. The standard stress freezing techniques were applied to the composite models with 40% fiber volume fraction.

It was observed that the slices from identical models could be combined for analysis and that a symmetric fiber arrangement results in a symmetrical stress distribution. Special care has to be taken in slicing the composite model to prevent the annealing of fringes and delamination along fiber direction. The shear stress, τ_{xy}, was observed to be zero under pure bending.

Both two-dimensional and three-dimensional finite element analysis was performed with certain simplifications. These results could be used in conjunction with photoelastic analysis since both showed good correlation. FEM analysis found the neutral axis of the composite model to coincide with that due to geometric symmetry.

Overall behaviour of the composite model showed a strong dependence on the three fiber plane. It was found that in order to obtain a complete analysis of three-dimensional stress distribution, reinforcing-fibers with photoelastic properties should be used.

ACKNOWLEDGEMENTS

The author wishes to acknowledge with sincere gratitude the advice and guidance of Dr. W.J.D. Shaw throughout the program.

Sincere thanks are owed to the technical staff of the Department of Mechanical Engineering for their help, especially Mr. R. Bechtold, A. Moehrle and G. East.

Special thanks are due to Dr. E.W. Johnson for his help and advice on photoelastic techniques.

Special thanks are also due to Mr. B. Allan for help and advice on photographic techniques.

Finally, the author is grateful for financial support provided by the Department of Mechanical Engineering, University of Calgary and the Natural Sciences and Engineering Research Council.

TABLE OF CONTENTS

Page

LIST OF TABLES

LIST OF FIGURES

Page

Page

Page

Page

Page

NOMENCLATURE

In addition to the nomenclature defined in this section, symbols have been defined throughout the text whenever it was felt necessary for clarity.

a	amplitude of plane polarised light
A	cross-sectional area
A_c	cross-sectional area of composite
A_f	cross-sectional area of fiber
A_m	cross-sectional area of matrix
c	distance from the neutral axis
C_1, C_2	Stress-optic coefficient
E	Young's modulus
E_c	Young's modulus for composite
E_f	Young's modulus for fiber
E_m	Young's modulus for matrix
f_σ	material fringe constant
G	Shear modulus
I	Light intensity
'I'	Moment of inertia
M	Bending moment
n_o	Initial index of refraction
n_1, n_2, n_3	Principal indices of refraction
N	Fringe order
N_x	Fringe order in x-direction

N_z — Fringe order in z-direction

P — Applied load

P_c — Load carried by composite

P_f — Load carried by fibers

P_m — Load carried by matrix

R — Radius of cam

S_{xy} — Shear stress used in FEM output

S_x, S_y — Principal stress in x- and y-direction used in FEM output

t — Thickness of slice/specimen

T — Temperature of the oven

V — Volume of material

V_f — Volume fraction of fibers

V_m — Volume fraction of matrix

V_{crit} — Critical volume fraction of fibers

V_{min} — Minimum volume fraction of fibers

GREEK LETTERS

α — coefficient of thermal expansion

α — retardation angle introduced by the stressed model

Δ — relative retardation

ϵ — true strain

ϵ_c — strain in composite

ϵ_f — strain in fiber

ϵ_m — strain in matrix

λ	wavelength of light
ν	Poisson's ratio
σ	applied stress
σ_1, σ_2	principal stresses acting on planes
σ_{cu}	ultimate tensile strength of composite
σ_{fu}	ultimate tensile strength of fibers
σ_{mu}	ultimate tensile strength of matrix
σ_x	principal stress in x-direction
σ_{xy}	shear stress in xy-plane
σ_y	principal stress in y-direction
σ_z	principal stress in z-direction
θ	angle of principal stress direction with the axis of the polarizer
τ	shear stress
τ_{max}	maximum shear stress
τ_{xy}	shear stress in the xy-plane
τ_{yz}	shear stress in the yz-plane

CHAPTER ONE

INTRODUCTION

Fiber-reinforced composites are one of the most widely used in the family of composite materials. Fibre-reinforced materials have become important structural materials, and their utilization in the aerospace and transport industries is continuously increasing. Their study and development has been largely carried out due to their vast structural potential. In a fibre-reinforced composite, strong fibres are dispersed in a softer, more ductile matrix. In general, the fibres are brittle, or have little ductility prior to fracture, but when combined with a ductile matrix, the resulting material has excellent strength and toughness. Such composites are usually intended to be used where high strength and high strength to weight ratios are needed, where high temperature strength is desired, and where other special properties are required.

The structural behaviour of a composite is intimately related to the internal stress level and stress distribution and depends on the load transfer between the constituent parts. The field of micromechanics comprises the study of these internal stresses and mechanics of internal reactions and interactions of the constituent parts due to imposed forces. Knowledge of internal states of stress serve two main purposes; first, it contributes to the evaluation of average (macroscopic) response and, secondly, it provides the basis for understanding failure modes and establishing failure criteria.

Stresses in the matrix are of great importance when loads act in a direction normal to the fibres, since in this case initial failure may be governed by stress and strain concentration in the matrix. Failure initiation is related to the internal state of stress which is determined by the geometry, loading, and properties of the constituent materials. The state of stress may be very complex and difficult to determine by analysis, thus, experimental means are essential and sometimes indispensable. Experimental methods applicable to the study of mechanics of composites include photoelasticity, strain gauge analysis, moire fringe analysis, and holography. Because of its whole-field character, the use of photoelasticity would obviously be very advantageous for the evaluation of the stresses in composite materials.

Photoelasticity [1-3]*, one of the traditional experimental

---

*Numbers refer to the references at the end of this thesis.

methods, has been used for many years to analyse stress problems using models made from transparent plastics. The stress-optic relations, stated very simply, linearly relate the principal stress difference to the birefringence produced in the loaded model. The stress-optic relations of conventional photoelasticity do not apply to orthotropic materials. However, orthotropic elastic behaviour does not preclude the use of photoelasticity methods.

The application of photo-orthotropic-elasticity to stress analysis of structures fabricated from composite materials involves the development of a model which is sufficiently transparent for light to be transmitted in a polariscope. Also, the model material must exhibit the required degree of anisotropy and show an adequate degree of birefringence.

This thesis explores the use of a three-dimensional photo-elastic model to study orthotropic stress behaviour in fibre-reinforced composite materials. Scaled up models of composites are fabricated by casting PLM-4[1] epoxy around Nylatron GS[2] rods. These models are loaded in four-point

---

[1]Product trade name of Intertechnology.

[2]Product trade name of Polypenco.

bending to get the desired pure bending effect. The standard stress-freezing techniques are applied to the composite models with 40% fibre volume fraction. The models are then sliced and fringe patterns are observed in the polariscope. The shear-difference method in three-dimensions and the limited use of finite elements is applied in the analysis.

Due to limited resources and time constraints this study is intended to lay groundwork for overall stress distribution in fiber-reinforced composites. Hence, establishing the scaling factors and application of results to the prototype is recommended for future work.

CHAPTER TWO

BACKGROUND OF THEORETICAL METHODS

Composite materials have fully established themselves as workable engineering materials and are now quite commonplace around the world. The success of fibre composites results from the ability to make use of the outstanding strength, stiffness, and low specific gravity of fibres such as glass, graphite, or kevlar. Properties of composites are strongly influenced by the properties of their constituent materials, their distribution, and the interaction between materials. Besides specifying the constituent materials and their properties, in describing a composite material as a system, one needs to specify the geometry of the reinforcement with reference to the system. The geometry of the reinforcement may be described by the shape, size, distribution, and orientation.

Composite materials can be classified on the basis of the geometry of a representative unit of reinforcement. Figure 2.1 represents a commonly accepted classification scheme for composite materials. This particular study involves the use of unidirectional fibre-reinforced composites.

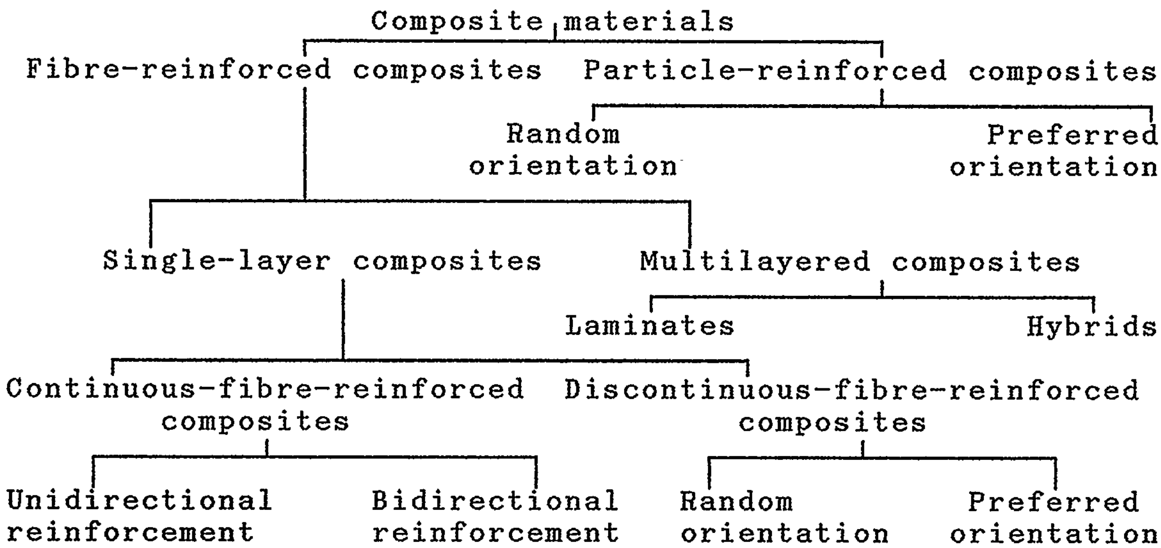

Figure 2.1: Classification of composite materials [4].

2.1 THEORY OF UNIDIRECTIONAL FIBRE REINFORCED COMPOSITES

A unidirectional composite may be modeled by assuming fibres to be uniform in properties and diameter, continuous and parallel throughout the composite. It may be further assumed that a perfect bonding exists between the fibres and the matrix so that no slippage occurs at the interface and strains experienced by the fibre, matrix, and composite are equal:

$$\epsilon_f = \epsilon_m = \epsilon_c \qquad (2.1)$$

where, ϵ is the strain, and subscripts c, f, and m stand for composite, fibre, and matrix respectively.

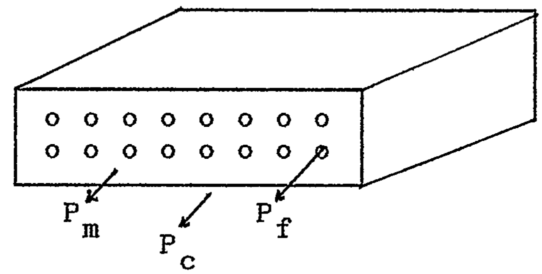

Figure 2.2 : Cross-section of a unidirectional fibre composite.

If the fibres and matrix behave elastically and linearly, the stresses are

$$\sigma_f = E_f \epsilon_f \quad \& \quad \sigma_m = E_m \epsilon_m \qquad (2.2)$$

and the load carried by the fibres is

$$P_f = \sigma_f A_f = E_f \epsilon_f A_f \qquad (2.3)$$

where:

A cross-sectional area

P applied load

The resultant carried by the composite is the sum of the components, thus

$$P_c = P_f + P_m \qquad (2.4)$$

$$\sigma_c A_c = \sigma_f A_f + \sigma_m A_m \qquad (2.5)$$

Equation (2.5) can be written in terms of volume fraction, V_f and V_m as follows:

$$\sigma_c = \sigma_f V_f + \sigma_m V_m \qquad (2.6)$$

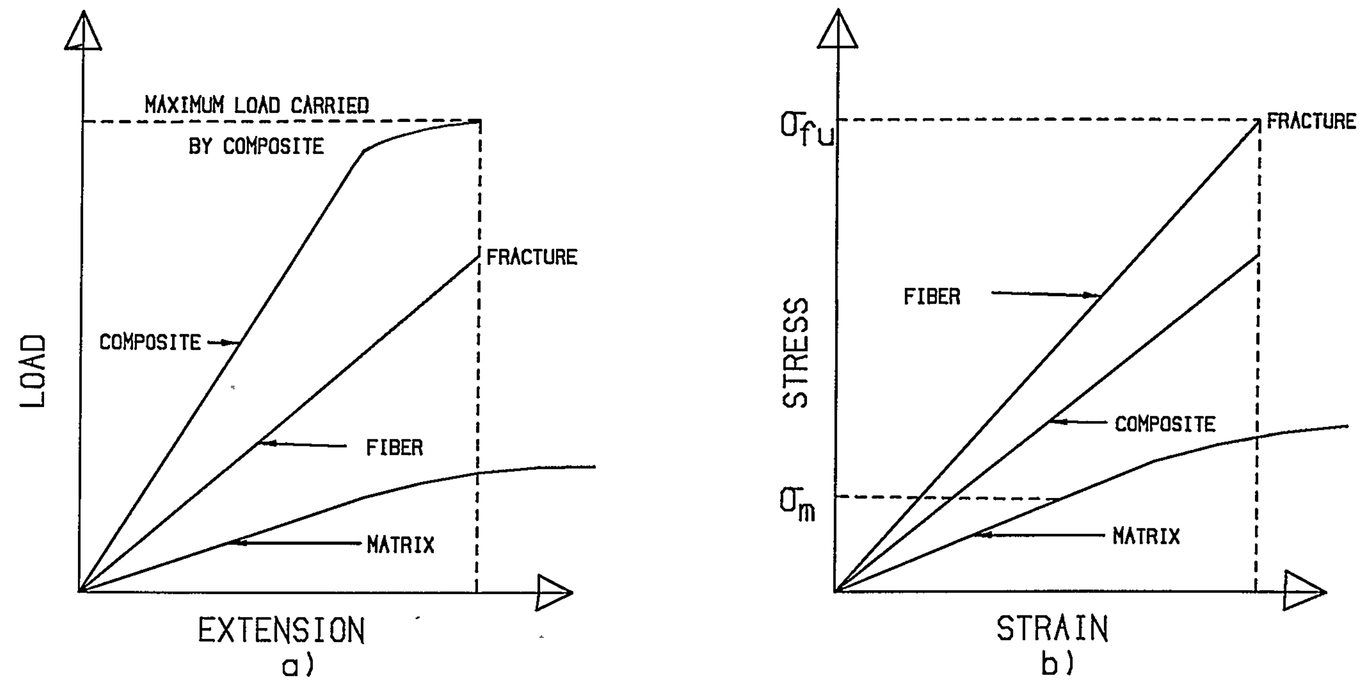

FIGURE 2.3: CURVES FOR IDEALISED FIBER COMPOSITE CONSISTING OF CONTINUOUS BRITTLE FIBERS IN A DUCTILE MATRIX.[5]

a) LOAD VS EXTENSION, AND

b) CORRESPONDING STRESS VS STRAIN

Differentiation of equation (2.6) yields

$$\frac{d\sigma_c}{d\epsilon} = \frac{d\sigma_f}{d\epsilon} V_f + \frac{d\sigma_m}{d\epsilon} V_m \tag{2.7}$$

where, $(d\sigma/d\epsilon)$ represents the slope of stress-strain diagrams which are constant in the elastic region and can be replaced by corresponding elastic moduli.

$$E_c = E_f V_f + E_m V_m \tag{2.8}$$

The relationships in equations (2.6) and (2.8) are called the rule of mixtures. These equations can be generalised as

$$\sigma_c = \sum_{i=1}^{n} \sigma_i V_i \tag{2.9}$$

$$E_c = \sum_{i=1}^{n} E_i V_i \tag{2.10}$$

The deformation of a composite may proceed in four stages.

1.) Both fiber and matrix deform elastically.

2.) Fibers continue to deform elastically, but matrix deforms plastically.

3.) Fibers and matrix both deform plastically.

4.) Fibers fracture followed by composite fracture.

Stage 2 has a stress-strain curve that is no longer linear.

The composite modulus must be predicted at each strain level by

$$E_c = E_f V_f + \frac{d\sigma_m}{d\epsilon_m}\Bigg|_{\epsilon_m=\epsilon_f} V_m \tag{2.11}$$

where, $d\sigma_m/d\epsilon_m$ is the slope of the stress-strain curve of the matrix at the given strain of the composite. For stage 3, the elastic modulus of the composite can be predicted by using equation (2.7).

The ultimate strength of the composite, σ_{cu}, can be predicted by the rule of mixtures as:

$$\sigma_{cu} = \sigma_{fu} V_f + (\sigma_m)_{\epsilon_m} (1-V_f) \tag{2.12}$$

The strengthening effect of the fibres is obtained only when the ultimate strength of the composite exceeds that of the matrix alone; i.e.

$$\sigma_{cu} = \sigma_{fu} V_f + (\sigma_m)_{\epsilon_f}(1-V_f) \geq \sigma_{mu} \tag{2.13}$$

This defines a critical volume fraction of fibres, V_{crit}, that must be exceeded for strengthening:

$$V_{crit} = \frac{\sigma_{mu} - (\sigma_m)_{\epsilon_f}}{\sigma_{fu} - (\sigma_m)_{\epsilon_f}} \tag{2.14}$$

If the fibre volume fraction is less than V_{min}, then

$$\sigma_{cu} = \sigma_{mu}\,(1-V_f) \qquad (2.15a)$$

and, the ultimate strength of the composite, σ_{cu}, with $V_f > V_{min}$ is given by

$$\sigma_{cu} \geq \sigma_{mu}\,(1-V_f) \qquad (2.15b)$$

The equation (2.6) is applicable only when the fibre volume fraction exceeds the minimum fibre volume fraction; where,

$$V_{min} = \frac{\sigma_{mu} - (\sigma_m)|\epsilon_f}{\sigma_{fu} + \sigma_{mu} - (\sigma_m)\epsilon_f} \qquad (2.16)$$

All these ultimate composite values have been plotted in figure 2.4 as a function of fibre volume fraction.

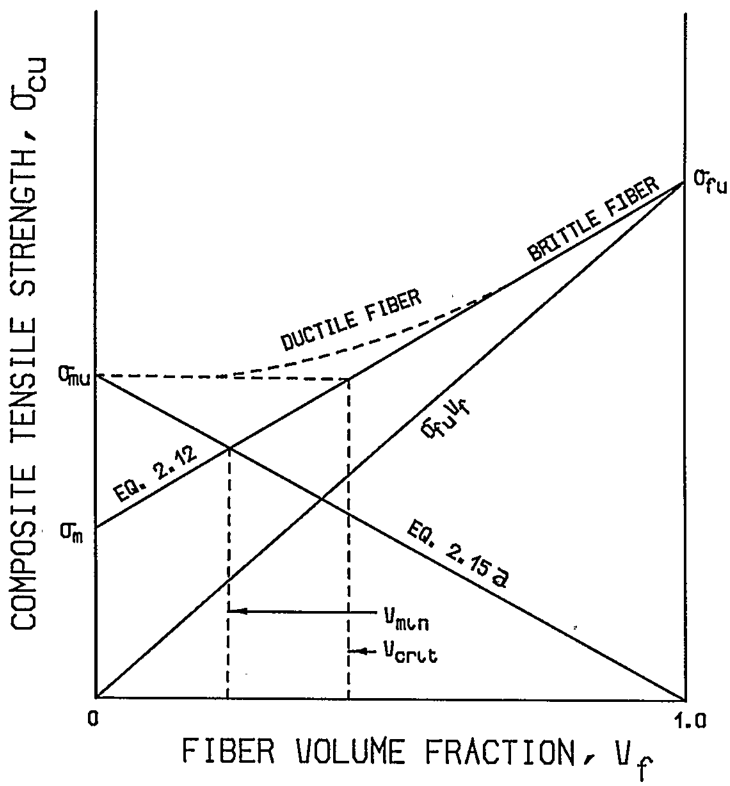

FIGURE 2.4: IDEALISED VARIATION IN TENSILE STRENGTH OF COMPOSITE WITH VOLUME FRACTION OF BRITTLE FIBERS.

2.2 THEORY OF PHOTOELASTICITY

Photoelasticity [1-3] is based on the phenomenon of temporary double refraction (optical anisotropy) which certain isotropic transparent materials exhibit when subjected to stress. This optical phenomenon, when viewed in a field of polarised monochromatic light, is manifested in the form of interference fringes or alternate dark and light bands. These fringes, referred to as "isochromatic fringes" are ordered according to the number of darkness-brightness cycles that appear at a point as load is increased from zero to its final value. The fringe order represents relative light retardation in wavelengths. The principal optical axes as found by Maxwell, coincide with the principal stress directions.

Photoelastic models are examined in the polariscope. The simplest one, the plane polariscope, consists of a light source, a polariser, and an analyser. The last two elements convert ordinary light to plane polarised light. If a stressed model is placed in the field (figure 2.5) with one principal stress direction at an angle θ with the axis of the polarizer, the light intensity at a point O is given by

$$I = 2a^2 \sin^2 2\theta \, \sin^2 \alpha/2 \qquad (2.17)$$

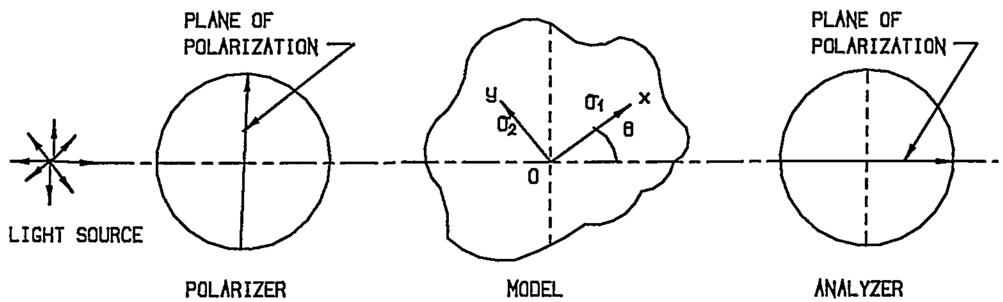

Figure 2.5: Schematic arrangement of the elements of a plane polariscope (σ_1, σ_2, are principal stresses).

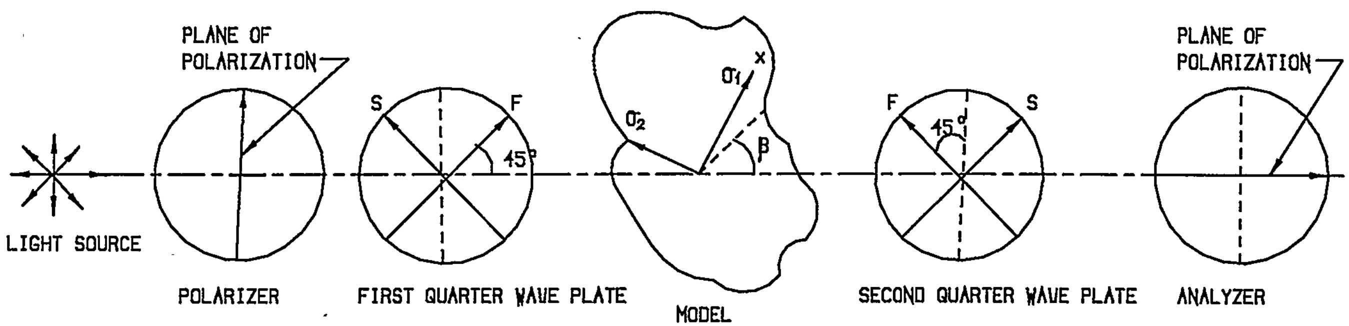

Figure 2.6: Schematic arrangement of elements of a circular polariscope.

where 'a' is the amplitude of the plane polarized light emerging from the polarizer and 'α' is the retardation introduced by the stressed model. Extinction occurs either when $\theta = 0, \pi/2$, or when $\alpha = 2n\pi$, i.e., the retardation is an integral number of wavelengths (integral fringe orders). These points of extinction form two families of fringes, <u>isoclinics</u> (loci of points of constant inclination of principal stresses) and <u>isochromatics</u> (loci of points of constant number of wavelengths of retardation, and therefore of equal principal stress-difference).

The isoclinic family is eliminated in the so called "circular polariscope" by introducing two properly oriented quarter-wave plates (figure 2.6). The optical transformation that takes place in this polariscope can be described as follows:

(1) The polarizer transforms the ordinary light into plane polarized light.

(2) The first quarter-wave plate transforms the plane polarised light into circularly polarised light.

(3) The second quarter-wave plate restores the original plane polarised light or rotates it through 90 degrees depending on whether it is crossed or parallel to the first plate.

(4) The analyser blocks or lets through the plane polarized

light according to the desired background.

Isochromatic fringes are related to the state of stress by means of the stress-optic law. Motivated from the stress-strain relations,

$$
\begin{aligned}
\epsilon_1 &= \frac{1}{E}[\sigma_1 - \nu(\sigma_2 + \sigma_3)] \\
\epsilon_2 &= \frac{1}{E}[\sigma_2 - \nu(\sigma_1 + \sigma_3)] \\
\epsilon_3 &= \frac{1}{E}[\sigma_3 - \nu(\sigma_1 + \sigma_2)]
\end{aligned}
\tag{2.18}
$$

we can write,

$$
\begin{aligned}
n_1 - n_0 &= C_1 \sigma_1 + C_2(\sigma_2 + \sigma_3) \\
n_2 - n_0 &= C_1 \sigma_2 + C_2(\sigma_1 + \sigma_3) \\
n_3 - n_0 &= C_1 \sigma_3 + C_2(\sigma_1 + \sigma_2)
\end{aligned}
\tag{2.19}
$$

where C_1, C_2 are the stress-optic coefficients; n_1, n_2, n_3 are the principal indices of refraction; and, n_0 is the initial index of refraction in the isotropic unstressed body.

Due to the difficulties involved in measuring the principal indices and the principal optical directions, photoelasticity is usually confined to measuring relative birefringence. From equations (2.19)

$$
n_1 - n_2 = (C_1 - C_2)\ (\sigma_1 - \sigma_2) \tag{2.20}
$$

Also,

$$n_1 - n_2 = \frac{\lambda \Delta}{2\pi t} \tag{2.21}$$

By substituting,

$$\Delta = \frac{2\pi t}{\lambda} (C_1 - C_2)(\sigma_1 - \sigma_2) \tag{2.21a}$$

If $C_1 - C_2$ is set equal to 'c', the relative stress optic coefficient,

$$\Delta = \frac{2\pi t c}{\lambda} (\sigma_1 - \sigma_2) \tag{2.21b}$$

or $$N = (t/f_\sigma)(\sigma_1 - \sigma_2) = \frac{2t}{f_\sigma}(\sigma_1 - \sigma_2)/2$$

$$= (2t/f_\sigma)\, \tau_{max} \tag{2.22}$$

or $$\sigma_1 - \sigma_2 = Nf_\sigma/t \tag{2.23}$$

where,

$N = \Delta/2\pi$ is the fringe order,

t is the length of optical path or, in some cases, thickness of specimens,

Δ is the relative retardation,

λ is the wavelength of light,

σ_1, σ_2 are the principal stresses acting on planes parallel to axis of light propagation,

τ_{max} is the maximum shear stress, and,

f_σ is a constant, called material fringe value, kPa/fringe/m (psi./fringe/in)

When the stress field is uniaxial, as it is on the nonzero boundaries, one of the principal stresses is zero and the nonzero component is determined directly from the stress-optic law above. In general, separation of principal stresses requires knowledge of some complimentary information or the use of some auxiliary numerical operations.

2.3 Three-Dimensional Photoelasticity

Photoelastic techniques are applicable to two- and three-dimensional problems. A two-dimensional analysis is justified when the state of stress in the structure can be approximated by a plane stress or a generalised plane stress condition. However, for the photoelasticity solution of three-dimensional problems, a somewhat more involved technique is necessary. The observation of the loaded model in a field of polarized light does not result in a fringe pattern which can readily be interpreted.

For three-dimensional problems, a three-dimensional scaled model of the prototype is machined or cast out of certain epoxies having the desired stress-freezing properties. The principle of stress freezing takes advantage of the visco-elastic, time and temperature dependent material properties of certain transparent epoxy resins which may be used to make accurate scale models of engineering components. In the frozen stress method, the loaded model is slowly heated to a critical temperature, held there for some time, and, finally, slowly cooled to room temperature. This process freezes or locks-in the state of deformation corresponding to the elastic state of stress at the elevated temperature. This state of stress is not disturbed by careful slicing of the model. Thin slices are removed from the model wherever the stress distribution is required. The material is calibrated by subjecting a loaded calibration specimen to the same temperature cycle as the model and observing the frozen fringe pattern.

The fringe pattern from the slices can be interpreted in much the same manner as in the case of a two-dimensional model. Shear stress distributions throughout the slice and principal stresses on free and pressure-loaded boundaries can be determined directly from the patterns. The determination of principal stresses at interior points is considerably more complicated and requires the use of auxiliary methods.

2.4 The Shear-Difference Method in Three Dimensions [1,6]

To determine the complete state of stress (that is, σ_{xx}, σ_{yy}, σ_{zz}, τ_{xy}, τ_{yz}, τ_{zx}) at an arbitrary point in a three-dimensional model, the shear-difference method is the most practical technique available. It should be noted, however, that the method involves a stepwise numerical integration procedure which tends to accumulate error. Hence, considerable care must be taken in collecting the input data.

The shear-difference method is based on the numerical integration of the first differential equation of equilibrium,

$$\frac{\partial \sigma_{xx}}{\partial x} + \frac{\partial \tau_{xy}}{\partial y} + \frac{\partial \tau_{xz}}{\partial z} = 0 \qquad (2.24)$$

If an arbitrary line OP is selected in the model in the manner illustrated in Figure 2.7, equation 2.24 can be integrated to obtain the stress σ_{xx} at the interior point x_1. Integrating,

$$\int_{x_o}^{x_1} \frac{\partial \sigma_{xx}}{\partial x}\, dx + \int_{x_o}^{x_1} \frac{\partial \tau_{xy}}{\partial y}\, dx + \int_{x_o}^{x_1} \frac{\partial \tau_{xz}}{\partial z}\, dx = 0 \qquad (2.25)$$

or,

$$\sigma_{xx}\Big|_{x_1} = \sigma_{xx}\Big|_{x_o} - \int_{x_o}^{x_1} \frac{\partial \tau_{xy}}{\partial y}\, dx - \int_{x_o}^{x_1} \frac{\partial \tau_{xz}}{\partial z}\, dx = 0 \quad (2.26)$$

where, $\sigma_{xx}|_{x_o}$ denotes the stress at point O and $\sigma_{xx}|_{x_1}$, the stress at point x_1 on the line AB. The partial derivative $\partial\tau_{xy}/\partial y$ is the rate of change of τ_{xy} with respect to y and $\partial\tau_{xz}/\partial z$ is the rate of change of τ_{xz} with respect to z. If finite but small values of Δx, Δy, and Δz are substituted for the partial differentials, it is possible to write,

$$\sigma_{xx}|_{x_1} = \sigma_{xx}|_{x_o} - \frac{\Delta\tau_{xy}}{\Delta y}\,\Delta x\, \Big|_{x_o}^{x_1} - \frac{\Delta\tau_{xz}}{\Delta z}\,\Delta x\Big|_{x_o}^{x_1} \qquad (2.27)$$

The value of $\Delta\tau_{xy}/\Delta y$ is obtained by measuring the value of τ_{xy} along lines AB and CD (shown in Fig. 2.7), subtracting the difference, and dividing by Δy. Similarly, the value of $\Delta\tau_{xz}/\Delta z$ is obtained by determining τ_{xz} along lines EF and GH, subtracting the difference, and dividing by Δz. For convenience, Δy and Δz may be taken numerically equal to Δx. Then equation (2.27) becomes

$$\sigma_{xx}|_{x_1} = \sigma_{xx}|_{x_o} - \Delta\tau_{xy}|_{(x_o+x_1)/2} - \Delta\tau_{xz}|_{(x_o+x_1)/2} \quad (2.28a)$$

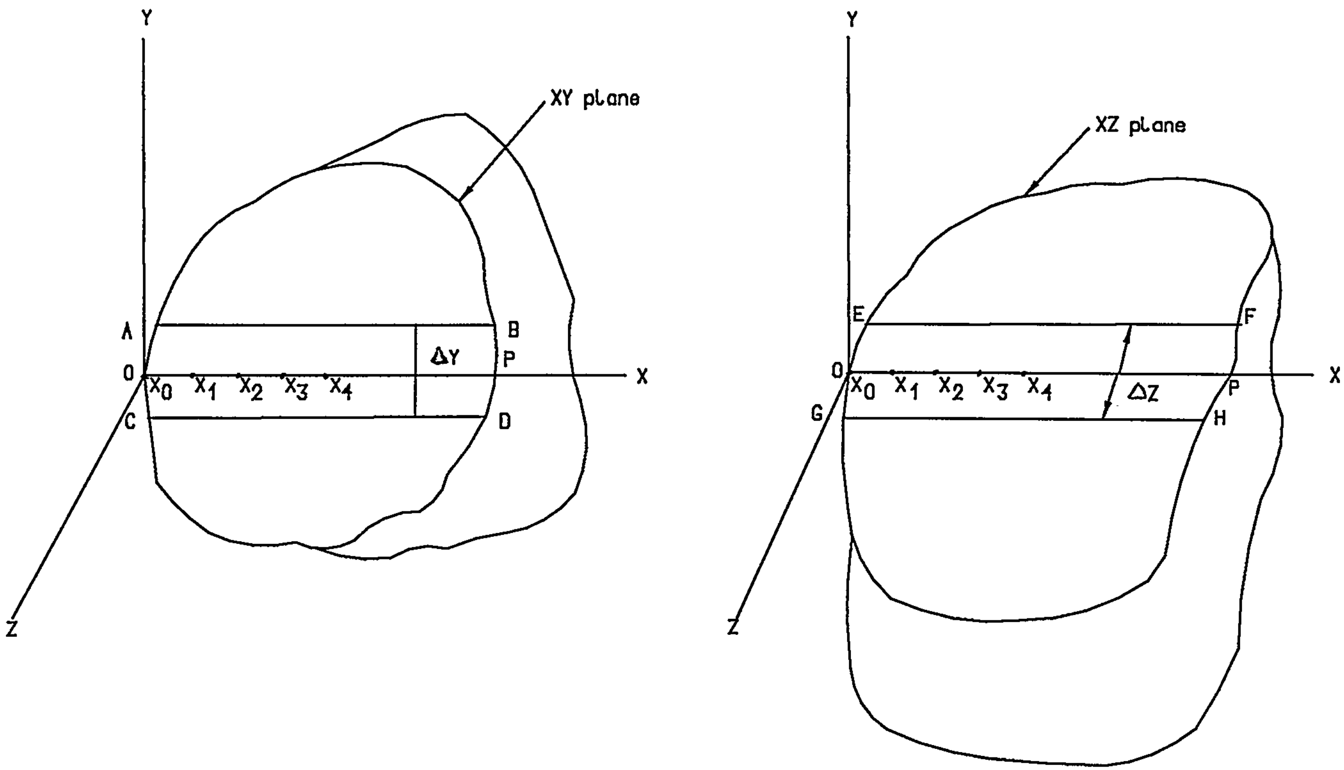

Figure 2.7: An arbitrary line OP and associated auxiliary lines in a general three-dimensional body.

in which $\Delta\tau_{xy}$ and $\Delta\tau_{xz}$ have the mean value in each interval Δx. By continuing this integration in a stepwise procedure, it is possible to write

$$\sigma_{xx}\big|_{x_2} = \sigma_{xx}\big|_{x_1} - \Delta\tau_{xy}\big|_{(x_1+x_2)/2} - \Delta\tau_{xz}\big|_{(x_1+x_2)/2} \tag{2.28b}$$

....

In concept the shear-difference method expressed in terms of Eqns. (2.28) is extremely simple; however, in application the method requires considerable input data obtained along lines OP, AB, CD, EF, and GH. To show the procedure for collecting these data, consider a slice taken from the model which contains the xy-plane shown in Fig. 2.7. This slice is then observed in normal incidence, and the isoclinic parameters and isochromatic fringe orders are established along lines OP, AB and CD. These data can be employed to obtain the shear stresses τ_{xy} along these three lines by using the following equation,

$$\tau_{xy} = \frac{1}{2}(\sigma_1' - \sigma_2')\sin 2\theta_z = \frac{1}{2}\frac{N_z f_\sigma}{t}\sin 2\theta_z \tag{2.29}$$

where,

N_z is the isochromatic fringe order observed by passing light through the xy-plane in the z-direction

θ_z is the angle which σ_1' makes with the z-axis as provided by the isoclinic parameter

σ_1', σ_2' secondary principal stresses

A second slice lying in the xz-plane and containing line AB would furnish similar information for τ_{xz}. Here a practical difficulty arises since the first slice removes an essential part of the second slice. One of several procedures may be used to eliminate this difficulty.

1) In the general case two identical models, identically loaded, may be used, one for the xy-slice and one for the xz-slice.
2) In large models it may be possible to use a subslice from the main slice (shown in Fig. 2.8) for determining τ_{xz}.
3) In the particular case where a plane of stress symmetry exists, advantage can be taken of this symmetry in the slicing plan.

The xz-slice is observed in the polariscope with the light passing through the subslice in the y-direction. Isoclinic parameters and isochromatic fringe orders along lines OP,

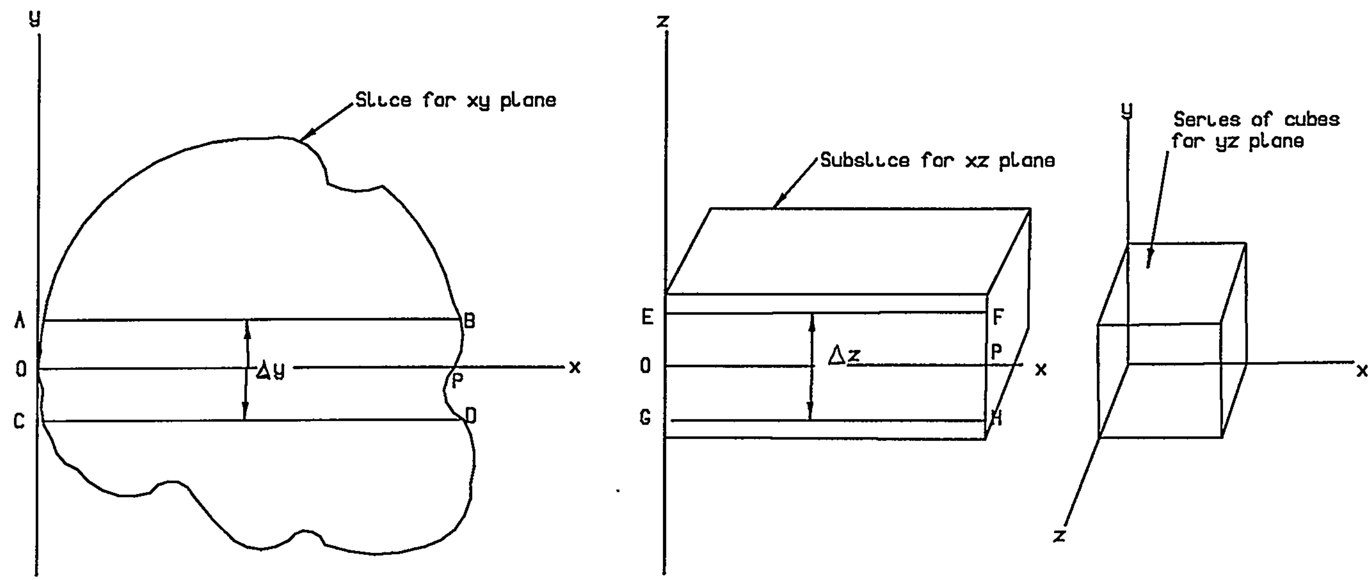

Figure 2.8: The slicing plan normally employed with the shear-difference method in three dimensions.

EF, and GH give the shear stress τ_{xz} as,

$$\tau_{xz} = \frac{1}{2}\,(\sigma_1"-\sigma_2")\,\sin 2\theta_y = \frac{1}{2}\frac{N_z\,f_\sigma}{t}\,\sin 2\theta_y \qquad (2.30)$$

where, $\sigma_1"$, $\sigma_2"$ are secondary principal stresses in xz-plane

At this stage τ_{xy} and τ_{xz} have been established along OP, and sufficient data have been obtained to employ Eqs. (2.28) to arrive at σ_{xx}. The other two normal stresses σ_{yy} and σ_{zz} can be established once σ_{xx} is known by utilizing the following equations,

$$\sigma_{yy} = \sigma_{xx} - \frac{N_z\,f_\sigma}{t}\cos 2\theta_z$$

$$\sigma_{zz} = \sigma_{xx} - \frac{N_z\,f_\sigma}{t}\cos 2\theta_z \qquad (2.31)$$

To evaluate the final cartesian component of stress τ_{yz}, the subslice may be reduced to a series of cubes each containing an evaluation point x_1, x_2, etc., as its center, as shown in Fig. 2.8. The yz-plane of these cubes is examined in the polariscope with the light passing through the cube in the x-direction. The isoclinic and isochromatic data are then employed to give τ_{yz} as shown below:

$$\tau_{yz} = \frac{N_z\,f_\sigma}{2t}\sin 2\theta_x \qquad (2.32)$$

CHAPTER THREE

LITERATURE SURVEY OF RELATED WORK

The determination of stresses and strains in three-dimensional composite bodies is a difficult problem, both theoretically and experimentally. However, such problems are of practical importance and find application in many structures such as fiber-reinforced composites, adhesion joints, rocket propellent shells, and foundation structures [7]. When a composite body made of two different materials connected along the interface is in equilibrium under mechanical or thermal loading, then the stresses and displacements in each of these bodies will depend on the elastic constants of both bodies. Use of photoelasticity for composite materials has been investigated to some degree [8-17]. Composite models using the photoelastic method have been discussed by earlier investigators [18-26].

Several investigators conducted both analytical and experimental studies in an effort to develop stress-optic relationships for the birefringent fiber-reinforced composite materials. Pih and Knight [8] pioneered work in this area and developed a stress-optic law based upon a stress-proportioning technique.

$$N = \frac{t}{f_\sigma} (C_1\sigma_1 - C_2\sigma_2) \tag{2.24}$$

where,

N = fringe order

C_1, C_2 = principal stress coefficients

σ_1, σ_2 = principal stresses

t = model thickness

f_σ = material fringe constant

Several authors [8-15] further carried on the theoretical work into the development of stress and strain-optic laws and theory of photoelasticity for fiber-reinforced composites. This work is well documented.

Stresses in the matrix are of great importance when loads act in direction normal to the fibers. In this case initial failure may be governed by stress and strain concentration in the matrix. Most of the work in this area is theoretical. Related experimental work is very limited and it has consisted mainly of two-dimensional model studies. It is indicated [18] that there are a couple of problems which are inherent in the three-dimensional photoelastic analysis of a fiber-reinforced composite, notably, i) model-material failure, and ii) loss of fringe pattern in slicing. Model-material failure arises when an insert material, such as steel or aluminum, is placed into an epoxy-matrix material. The steel or aluminum, which has a much lower coefficient of thermal expansion than the epoxy, causes the composite to fail either in bond along the insert or by cracking of the matrix material in the process of curing. Fringe pattern loss during slicing can occur during sawing of steel or aluminum inserts which raises the temperature of the epoxy matrix around the inserts sufficiently to anneal several fringes of the frozen photoelastic pattern. However, these problems are avoided by using plastic inserts in an epoxy-matrix material rather than steel or aluminum.

Chandrashekhara [19] et al. studied the application of the stress-freezing technique to birefringent models having similar ratios of elastic constants compared to the prototype. The stress distribution is not directly dependent on the value of elastic constants but on their ratios such as E_y/E_x, G_{xy}/E_y etc. Durelli, et al.[27], conducted many two and three dimensional photoelastic studies for the determination of shrinkage and mechanical loading stresses in matrices with various types of inserts. They used a low-temperature-curing epoxy cast around plexiglass or other epoxy inserts. Goree[28] investigated the case of in-plane loading of two rigid cylindrical fibers in an infinite matrix using a complex variable technique and pointed out a variation in maximum stress location with inclusion fiber spacing. For wide spacings, the maximum principal stress occurs at the interface, but for spacings less than one fiber radius, the location moves to the midpoint. he also indicated a considerable influence of Poisson's ratio of the mixture with the incompressible matrix producing the highest stress for a given spacing. For example, for a clear spacing of one-half the fiber radius, a Poisson's ratio of 0.5 produces a 40% increase in stress over that for a ratio of 0.25. In general, the influence of Poisson's ratio of the component materials has not been thoroughly investigated. Marloff and Daniel [22] carried out three-dimensional photoelastic analysis of a fiber-reinforced composite model and their results seem to indicate that the influence of Poisson's ratio may not be appreciable. Further, in their results the maximum stress occurs in the middle of the matrix section between fibers which is at variance with the theoretical prediction of maximum stress at the interface. Stress concentration factors varied from 1.80 at the interface to 2.0 at the midpoint of the matrix section between fibers.

Not only has most of the experimental work consisted of two-dimensional model studies, the limited amount of three-dimensional composite model studies have some shortcomings. In the study done by Chandrashekhara [19], fibre volume fractions used were less than 15 percent. This does not model a realistic range of composite materials as V_f usually ranges from 30% to 70%. Secondly, in some of the work done in this field, the number of inserts vary between 1 or 2, making it more susceptible to the free-edge effects. In the case of Marloff and Daniel [22], a period of one week was allowed for stabilization of the fringe pattern in the slices removed from the model. This procedure could lead to stress relaxation and consequently error. In the present study, an effort has been made to alienate most of these problems by using a better range of fiber volume fractions, and reducing the free-edge effects by utilising five rows of inserts.

CHAPTER FOUR

EXPERIMENTAL PROCEDURE

Scaled-up photoelastic composite models are used for the present study. An effort was made to model AS4/3501-6 graphite fiber composite as closely as possible. Composite models that were cast consisted of 40% fiber volume fraction, with the diameter of the reinforcing rods being 12.7 mm (1/2 in.). Governing criteria was established as the elastic modulus ratio of AS4/3501-6 graphite fiber composite; i.e. E_f/E_m of 46, at the stress freezing temperature of 116°C for the composite model.

4.1 Materials

4.1.1 Matrix

The Photoelastic PLM-4 epoxy resin system was used to model the matrix material of the composite material. The Photoelastic PLM-4 epoxy has been formulated by the manufacturer specifically for use in making thick-walled or heavy-sectioned models for three-dimensional photoelastic analysis by stress freezing. This resin system is characterised by a low exothermic reaction, making it feasible to cast large models without danger of overheating during polymerization. When properly cast and cured, this material offers excellent transparency, is relatively easy to machine, exhibits very little time-edge effect, and has high stress-optic sensitivity, with a stress-optical constant of 10.5 kPa/fringe/m at room-temperature and 0.40 kPa/fringe/m at the critical temperature of 116°C.

The PLM-4 resin system was supplied in a liquid resin and dry hardener combination, which can be mixed and cast to make any model configuration for which a mold is available. The following formula was used to mix the two components:

100 parts (by weight) of PLM-4 (liquid resin)

40 parts (by weight) of PLMH-4 (hardener)

4.1.2 Fiber

Considerable thought was made in the choice of the material for modelling the fibres. Mechanical testing was performed on Nylon 6-6, Teflon, Nylon 101, and Nylatron GS rods (see Appendix A). Governing criteria for the selection was established as: high-temperature behaviour, Young's modulus (to model the carbon fibers), and coefficient of thermal expansion (to reduce the shrinkage effects). It was found that Nylatron GS rods come the closest to satisfy the above criteria. Table 4.1 shows the properties of the matrix material and the selected rod material at room temperature and at the stress-freezing temperature. The stiffness and tensile strength properties at the stress freezing temperature were obtained experimentally where as all other data was supplied by the manufacturer. Using these materials an elastic modulus ratio, E_f/E_m of 26 at the stress freezing temperature is achieved.

Property	PLM-4 (epoxy)		Nylatron GS rods	
	R.T.	116 °C	R.T.	116 °C
Tensile MPa Strength (psi)	60 (9,000)	2.0 (290)	69 - 96 (10-14,000	12.5-14 (1.8-2,000
Elastic GPa Modulus(10^3psi)	3.1 (450)	0.017 (2.5)	3.1-4.1 (450-600)	0.442 (64)
Coeff. of Thermal Expansion 'α' in/in/°F	3.9×10^{-5}	9.0×10^{-5}	3.5×10^{-5}	---
Stress-optical Constant kPa/fringe/m (psi/fringe/in)	10.5 (60)	0.40 (2.2)	N/A	N/A
ν	0.36	0.50	---	---

Table 4.1: Material properties.

Another problem that had to be given consideration was the choice of a right mold release agent. After various tests it was observed that the best results are obtained by using Dow Corning 20[1] release coating. It provides a silicone parting film which effectively releases plastics and other elastomeric products. Since wetting was a problem for aluminum molds, Dow Corning 20 release coating was diluted by blending 10 parts (by weight) of Dow Corning 20 release compound with 80 parts Isopropanol (99%) and 10 parts Toluene.

4.2 Design of Models

Photoelastic composite models were designed to represent unidirectional single layer fiber-reinforced composites. Photoelastic PLM-4 epoxy was used for matrix material and 12.7 mm (1/2 in.) Nylatron GS rods were used to model the fibers. The elastic moduli of the matrix and fiber material were such that a modulus ratio (E_f/E_m) of 26 was achieved at the critical temperature. Five rows of rods were used to get away from the edge effects. The rods were aligned symmetrically, therefore, resulting in a square cross-section. The composite model with 40% fiber volume fraction had a final size of 69x69x300mm (2.75"x2.75"x12").

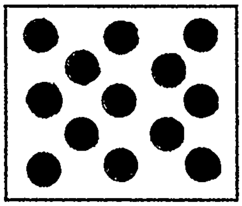

End View

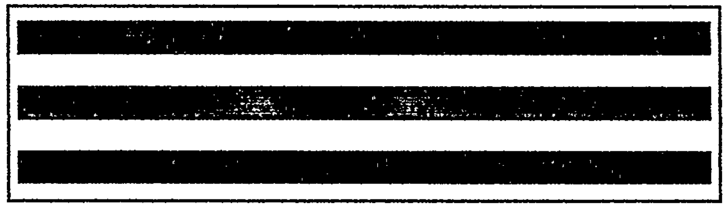

Section of Side View

Figure 4.1: Composite model with unidirectional reinforcement.

4.3 Design of Molds

The molds to cast the photoelastic models were made out of aluminum. Two identical molds were made for each fibre volume fraction studied. In addition, a calibration specimen for each batch was made at the same time. The molds were designed in such a way that leakage of resin material would not occur and the rods were easily positioned. The mold frame consists of four rectangular plates and two end plates. Mold assembly is shown in figure 4.2. Positioning of the rods was accomplished through the use of end plates. The rods were placed in the recesses in the bottom end plate and aligned at the top through the holes in the top plate. After casting the bottom plate comes off easily whereas the resin and rods at the top plate must be sawed off. Provision was made in the top plate to pour the resin material, and, to let out entrapped air. The mold was held together by a set of screws and the end plates were kept in place by using a clamp, thus, making it easier to take the mold apart to remove the casting.

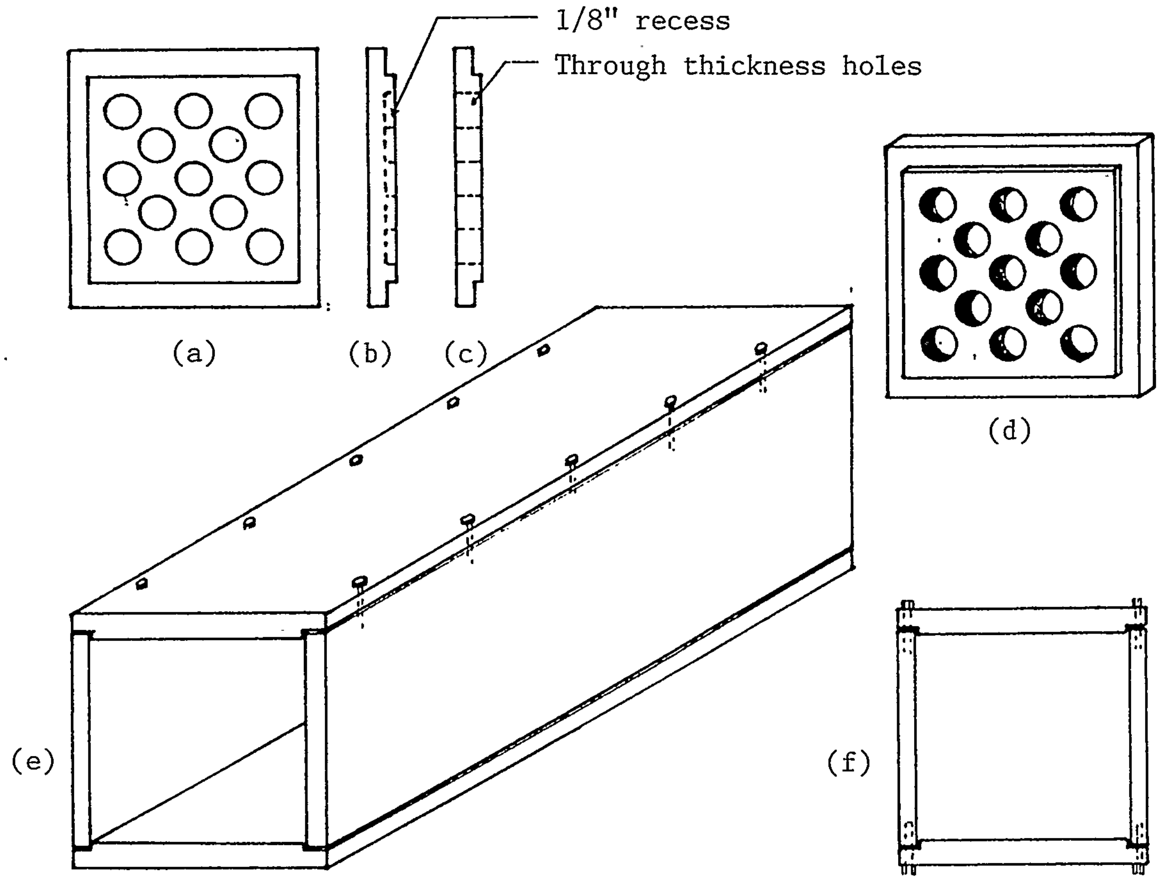

Figure 4.2: Composite model mold assembly; (a) & (d) End plates for the mold, (b) & (c) Bottom and Top End plates, respectively; (e) & (f) Main rectangular frame of the mold with square inside cross-section.

4.4 Model Preparation

4.4.1 Mold Preparation

First, the surface of the mold was cleaned with acetone. Once this was accomplished, the casting surface was completely coated with a smooth layer of Dow Corning 20 release coating. When the surfaces were dry (usually 15-20 minutes) the molds were assembled and ready for positioning of the plastic rods. The Nylaytron GS rods were cut to the desired length and the surfaces were wiped with acetone for clean surface bonding with the matrix material. The rods were held in position in the model by placing them through holes in the end plates at both ends of the mold. The mold was then clamped, as shown in figure 4.3, and placed in the oven and raised to a temperature of 105°C (220°F).

4.4.2 Resin and Hardener Preparation

Total amount of resin and hardener mixture required for the molds was calculated. PLM-4 liquid was weighed out in a container large enough to hold the total amount of mixture required. In a separate container, the desired amount of PLMH-4 hardener was weighed out. Both containers were placed in an oven at 105°C (220°F), and left overnight (12-14 hrs).

Figure 4.3: Assembled mold in the clamp with plastic rods in place.

The soaking time was used to dry out any moisture trapped in the two compounds.

4.4.3 Mixing and Pouring

1. After the 12 hour drying period, the hardener was slowly added to the resin while maintaining the temperature at 105°C.
2. The two were mixed thoroughly with a mechanical stirrer so as to dissolve the hardener and thus produce a homogeneous mixture. Stirring was done in the furnace using a flexible drive shaft with an electric motor mounted outside, see figure 4.4. Stirring was kept slow to keep generation of air bubbles to a minimum. Stirring was continued for approximately six hours. During the mixing cycle, the temperature was maintained at 105°C.
3. When thoroughly mixed, the resin was poured into the hot mold (both resin and mold were at the same temperature of 105°C). The resin was poured slowly as another precaution against the introduction of air bubbles.
4. Once poured, the temperature of the cast liquid resin was held constant at 82°C for 44-48 hours until gelation occurred.
5. After gelation has occurred, the temperature of the oven was slowly raised to 127°C at a rate of 2-3°C per hour.

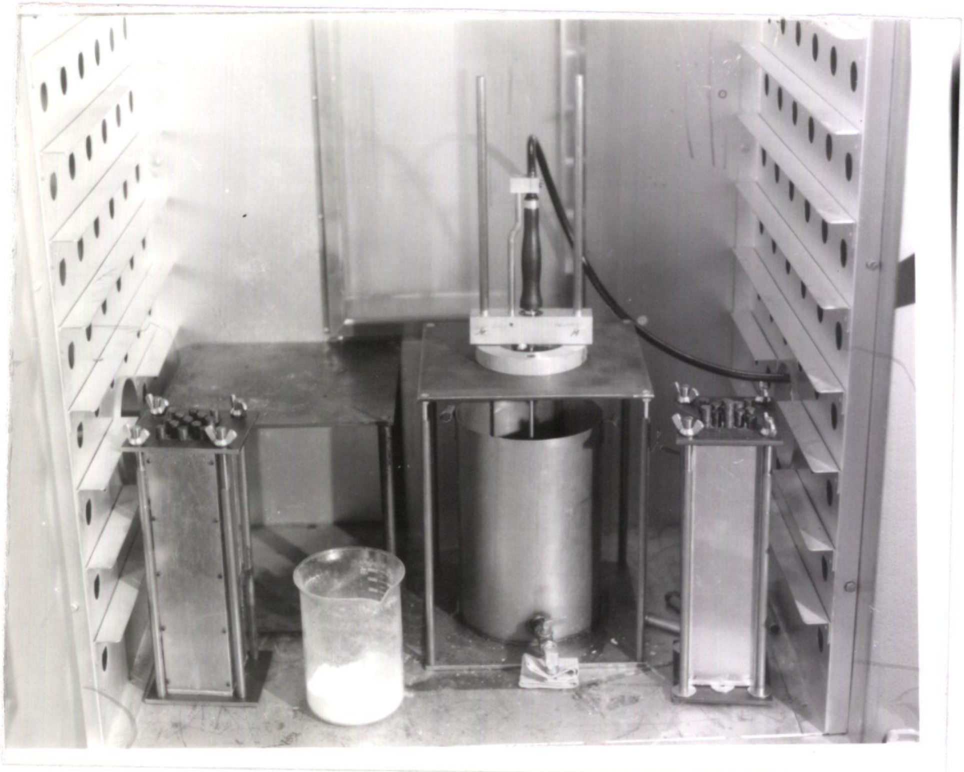

Figure 4.4: Stirring equipment to mix PLM-4 liquid resin and PLMH-4 hardener in the oven at 105°C.

6. The temperature of the oven was maintained at 127°C for approximately 12 hours; the mold was removed from the oven and the cast resin is removed. At this point, the cast resin was in a hard, rubbery state and unmolding was relatively easy. Unmolding was done as rapidly as possible so that the casting does not cool appreciably.
7. The complete procedure described above takes about five days and the temperature cycle in the oven was controlled by a <u>cam</u>. The cam motor is such that one rotation is achieved in 14 days. The cam/follower set up is shown in figure 4.5.

4.4.4 Postcuring

1. After the casting had been removed from the mold, it was placed on a smooth, flat plate of glass that had been dusted with talcum powder (figure 4.6). The powder acts as a mold release to allow the casting to contract or expand during postcuring.
2. The casting was placed back in the oven, with the temperature raised from 127°C to 138°C at a rate of 2°C per hour. When the 138°C temperature has been reached, it was held constant for at least 48 hours. The casting (photoelastic model) is now fully cured.
3. The casting was slowly cooled back down to room temperature. The rate of cooling is very critical, and

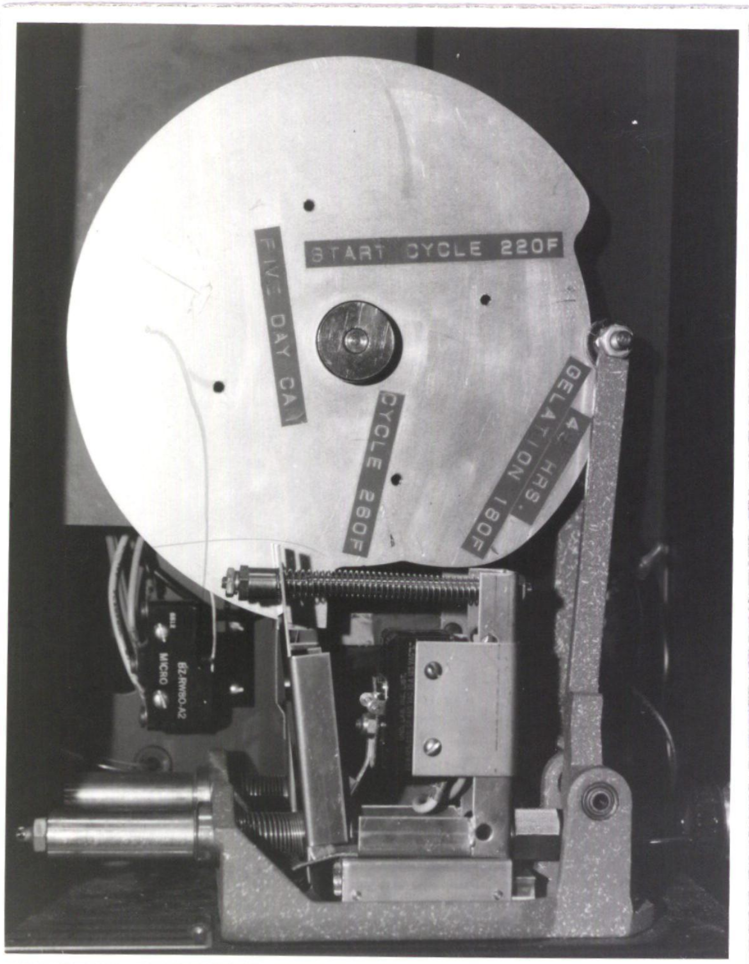

Figure 4.5: Cam/follower set up to control the thermal (temperature) cycles of the oven.

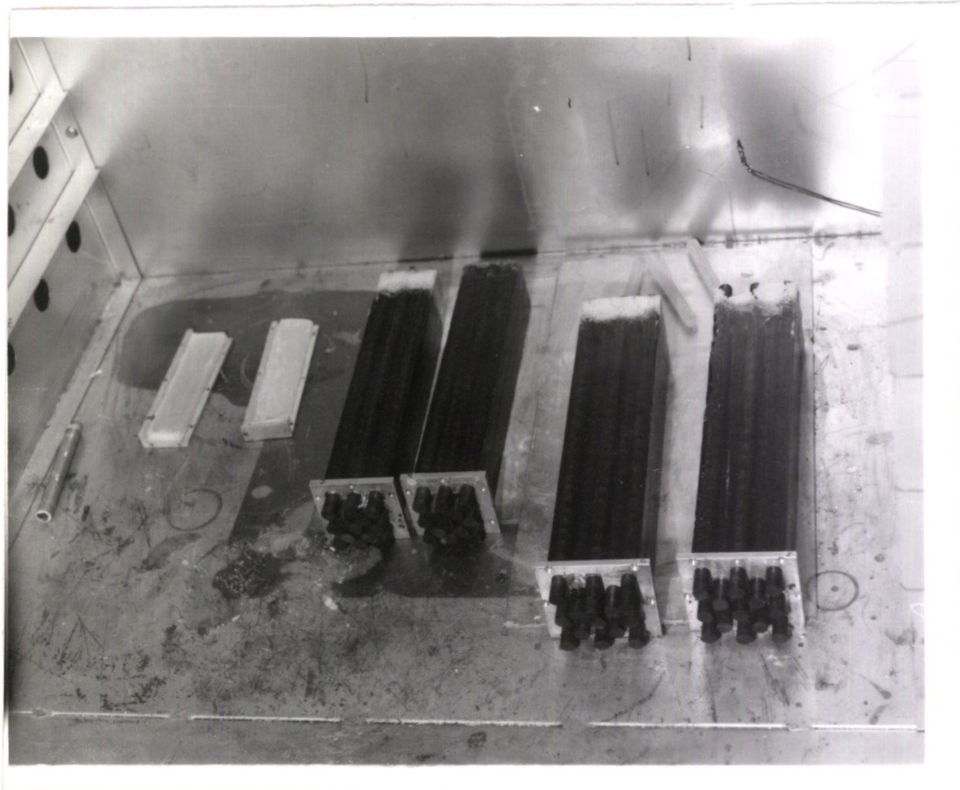

Figure 4.6: Photoelastic composite model castings, during the curing cycle in the oven.

must be done properly in order to avoid any thermal stresses that may develop during cooling. Therefore, the following schedule was maintained:

Temperature decrease	Cooling rate
138 to 93°C (280 to 200°F)	0.3°C per hour (0.5°F per hour)
93 to 60°C (200 to 140°F)	0.4°C per hour (0.75°F per hour)
60 to 38°C (140 to 100°F)	0.75°C per hour (1.5°F per hour)
38°C to Room Temperature (100°F to R.T.)	Turn oven off and allow the casting to cool to room temp.

The temperature cycles through the postcuring process were maintained through 13.5 day cam, which makes it one continuous procedure/cycle. The casting (photoelastic model) was then ready for final machining and preparation prior to loading and stress freezing.

4.5 Loading and Stress Freezing

The composite model casting was prepared for loading and stress freezing by sawing off the end plates and removing portions of the ends if they contained any defects.

4.5.1 Loading

The type of loading arrangement for the composite model was four-point bending. The bending moment/stress was held constant over a length of 63.5 mm or 2 1/2 in. (i.e. between the inner two loading points). The desired amount of load was calculated to induce the necessary number of fringes in the model, and at the same time keeping the maximum stress level well below the yield stress in order to stay in the elastic region. The amount of load varied for composite models with different fibre volume fractions. The micro-mechanical prediction method and the transformed section theory were used for this determination. 12.7 mm (1/2 in.) steel rods are used as load distributors and support points to get concentrated load effects without inducing excessively high stress concentrations. The loading arrangement is shown in figure 4.7. A load cell was used to monitor the desired amount of load on the model in the oven during the stress freezing cycle. In the event of the model deflecting considerably, load springs are used to maintain

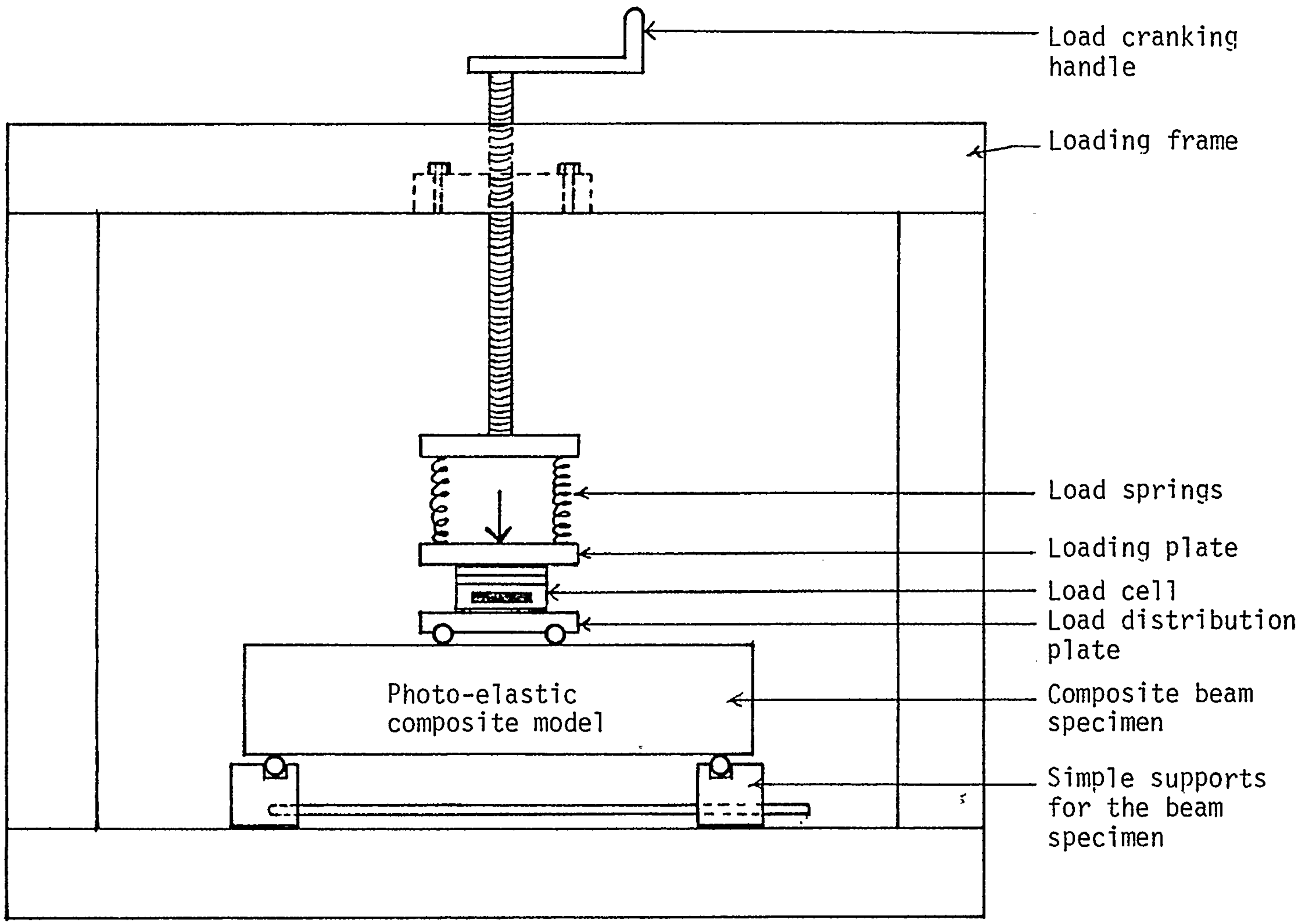

Figure 4.7: Loading arrangement for the photoelastic composite model.

the load on the specimen. Springs act to keep the loading plate in contact, and the spring constant is such as to keep the load change to a minimum. Furthermore, during the whole cycle, the load cell output is monitored and any changes were compensated to maintain a constant load level.

Calibration beam specimen (37.5 x 135 x 7.5 mm) made out of PLM-4 epoxy was also loaded in four-point bending and went through the same curing and loading cycle. A calibration specimen was used to establish the fringe factor constant for each batch of models cast.

4.5.2 Stress Freezing

Stress freezing operation consists of the following:

- Heating the model above the softening point of the resin.
- Loading the model at this elevated temperature.
- Cooling the model slowly to room temperature while retaining the load.

The stress freezing temperature for PLM-4 is approximately 113°C (235°F). The model is heated to a temperature 5°C (10°F) higher than the above, heating rate approaching this temperature being slow ≃ 2 to 3°C (5°F) per hour and maintained at 118°C (245°F) for about an hour so that a uniform temperature is achieved. After loading the model at this stress-freezing temperature, the cooling rate described previously for postcuring the casting is maintained. Again, a cam is used to control the temperature for the whole process, taking about 10 days. Now, the model is ready to be sliced and analysed in the polariser.

It should be noted here that the total time involved in preparing the composite models and stress freezing them (excluding slicing and polishing) is close to 31 days. And, this procedure is repeated for different fibre volume fraction composite models.

4.6 Slicing and Polishing

Photoelastic composite models with frozen stresses were cut into 6-7 mm (1/4") thick slices and then polished. The slices were cut in a predetermined set pattern. These slices were analysed in the polariser. Required isochromatic fringe patterns and isoclinics were recorded on photographs. The slicing pattern is shown in figures 4.8 and 4.9. The slices were removed from the area between the inner two loading points on the model. This is the region of interest because the bending moment is constant in this area.

Slicing pattern shown in figure 4.9 was based on the convenience of analysis. The main thrust was to obtain as much information as possible. Slices were removed in the xy-plane and yz-plane. Slices in the xy- and yz-plane contain information about σ_{xx}, σ_{yy}, σ_{zz}, τ_{xy} and τ_{yz}. Slices in xz-plane were not removed for two reasons:

i) it was almost impossible to slice due to the curvature of deflection, and

ii) these slices were not necessary for the analysis since no additional information was forthcoming.

A lot of problems were encountered and overcome in the cutting of the photoelastic composite model. Major problems were associated with brittleness of the matrix, delamination along fiber-matrix interface and sensitivity to heat buildup during cutting. Initially, the slices were cut on the milling machine using slitting saws. But due to the binding pressure exerted along the surface of saw, the material either shattered or delaminated during the cut. After trying a few test cuts, it was decided to slice the model using a thin

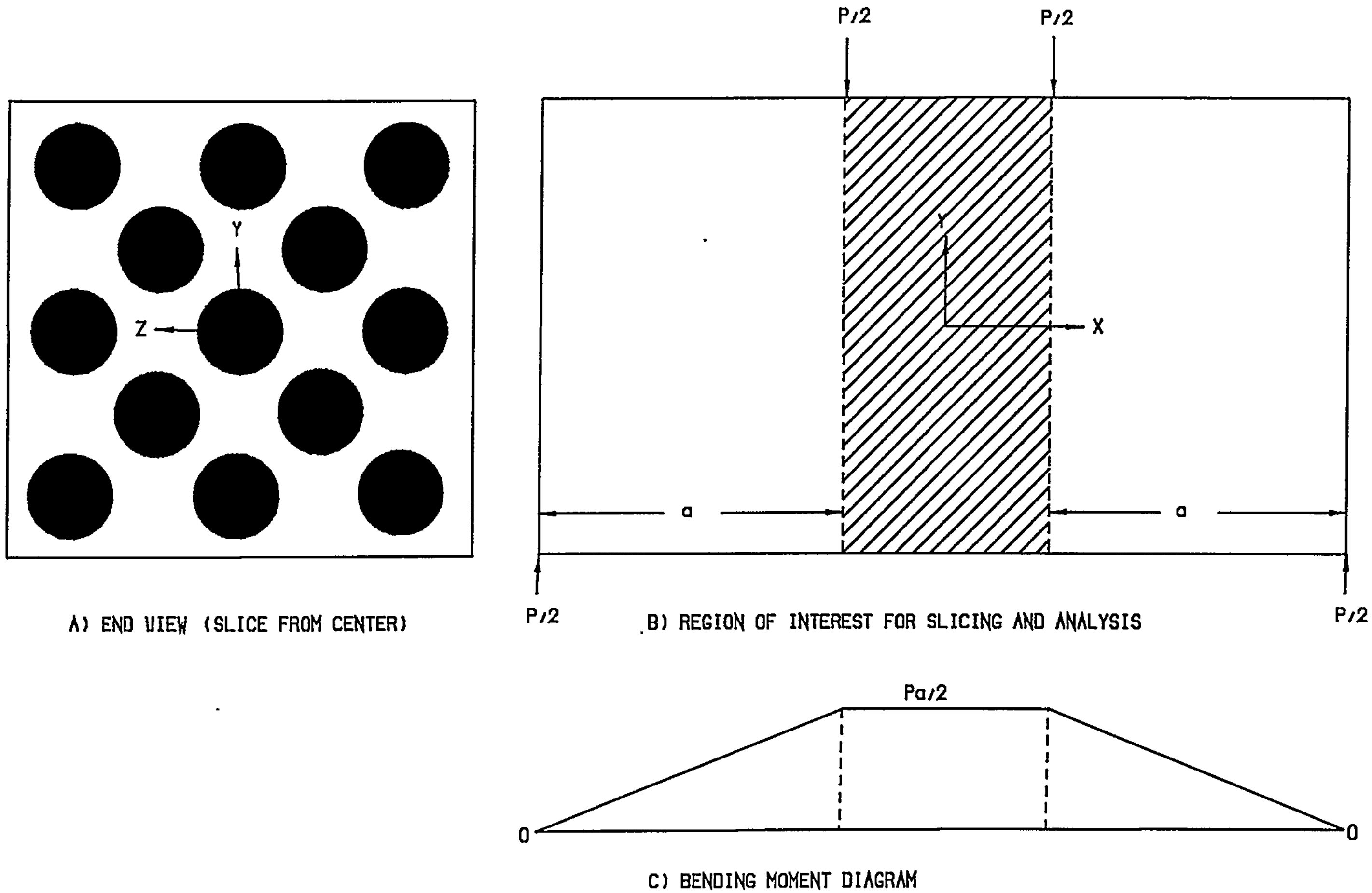

Figure 4.8: Composite model for analysis.

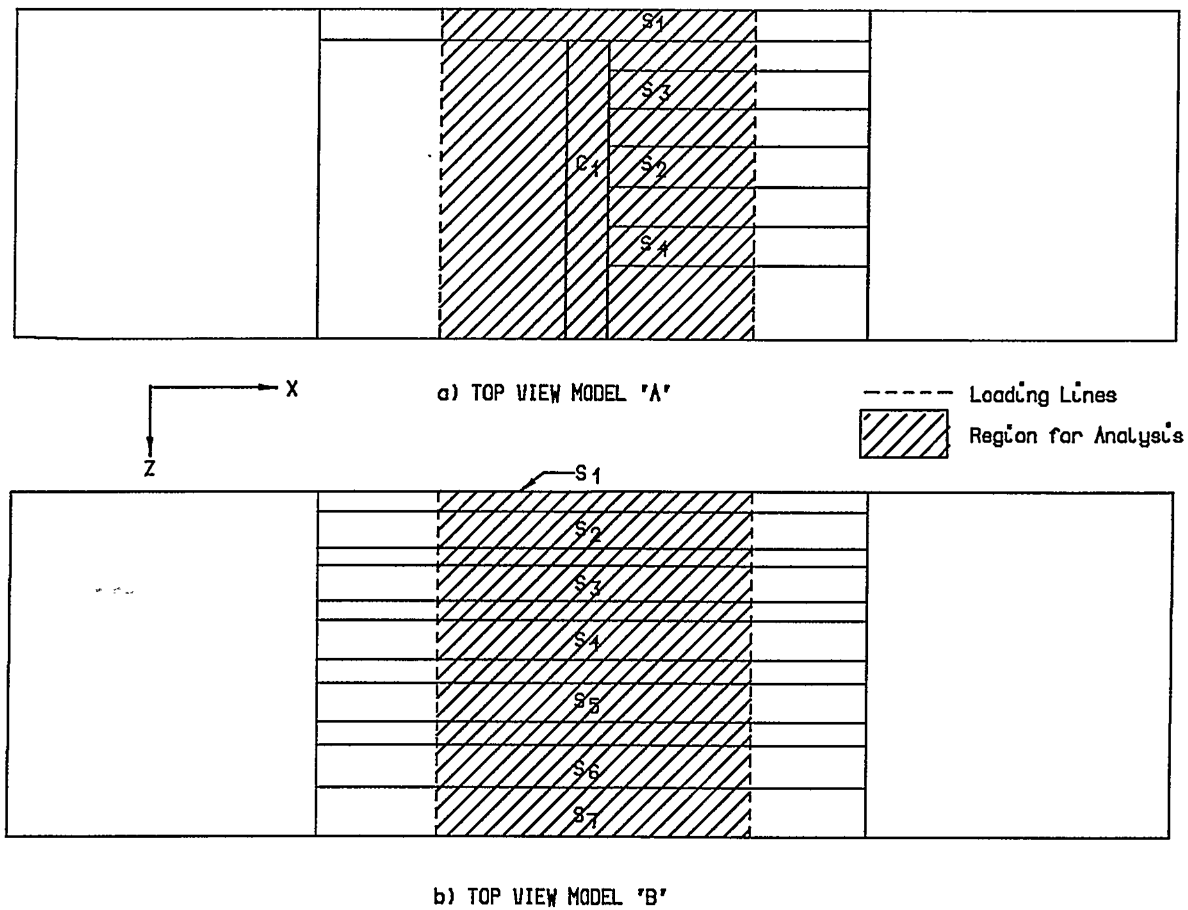

Figure 4.9: Slicing pattern for models A and B.

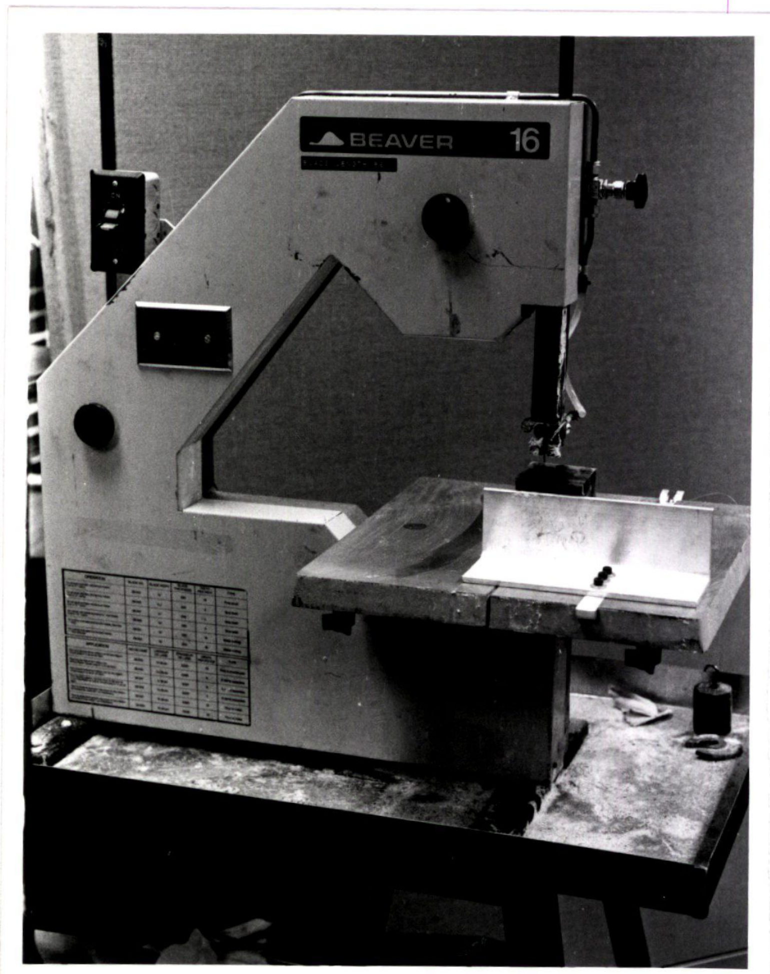

Figure 4.10: Band-saw unit for cutting slices from the composite model.

band saw. Since this produced an uneven finish, the slices were now required to be polished. A band saw unit was modified with a cooling and lubricating system as shown in figure 4.10. It was set up for cutting the photoelastic composite material.

Slices were cut according to the slicing pattern discussed earlier. Most of the slices cut were 6-7mm thick. Exceptions were slices S_1 and S_7 along the sides of the model. Due to the nature of these slices required, thickness dropped as low as 2-3 mm. The material being very sensitive, prescribed cutting techniques were followed. Cutting speeds were high and the feed rate kept low. For the slices in the longitudinal direction, feed rate was about 3-5 mm/min. On average each slice took about 2 hrs. of cutting time with ample cooling lubrication.

Once the slices were cut, they were hand polished to obtain a smooth finish. Slices were polished from 150 grit down to 1000 grit. A distinctively smooth finish was obtained. This made the fringe patterns in the polarizer more resolvable.

Though the fringe patterns were clear, use of oil with a matching refractive index on the surface of the slices showed a marked improvement. It especially helped for the slices which had fringe orders greater than 10-15.

CHAPTER FIVE

RESULTS AND ANALYSIS

Slices removed from the models were analysed in the polariscope. Both Isochromatic and Isoclinic fringe patterns were observed. In order to perform analysis on the slices, first the fringe constant value has to be determined from the calibration specimen. Isochromatic fringe pattern and 0° isoclinics for the calibration specimen are shown in figure 5.1 and figure 5.2.

5.1 Calibration Specimen

The Isochromatic fringe pattern shown in figure 5.1 was used to calibrate the value of the stress-optical constant, f_σ, for the photoelastic matrix material. Being a simple beam specimen loaded in four-point bending, theoretical stress distribution was known. As can be observed in figure 5.2, the area of interest is enclosed by 0° isoclinics. Therefore, the specimen can be considered as a principal plane, and, σ_x and σ_y as principal stresses. Away from the stress concentration points, the fringe pattern and fringe orders are clearly visible. Stress-optical constant, f_σ, was

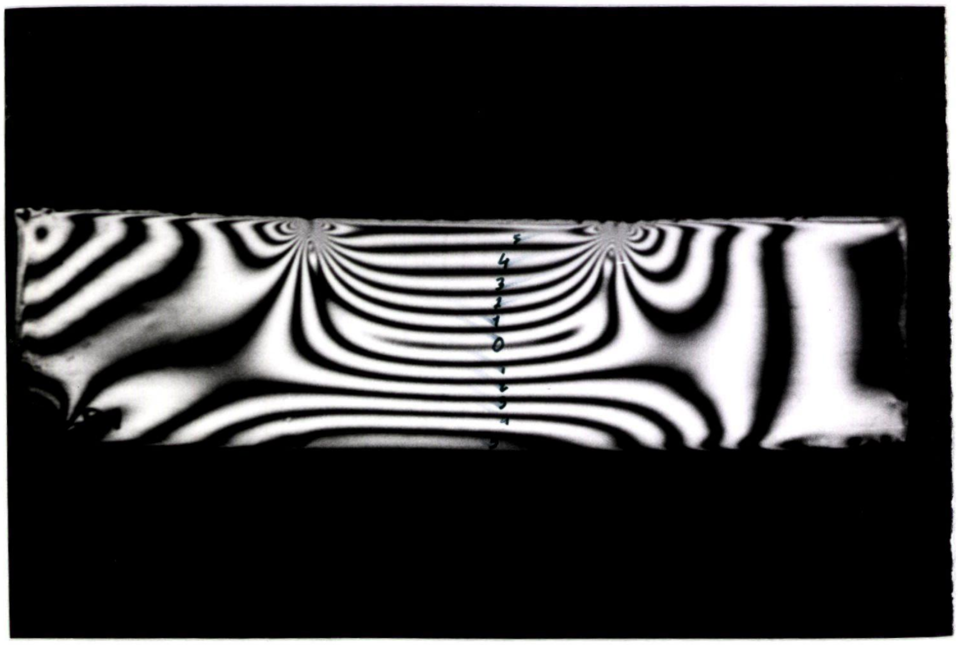

Figure 5.1: Isochromatic fringe pattern for Calibration Specimen.

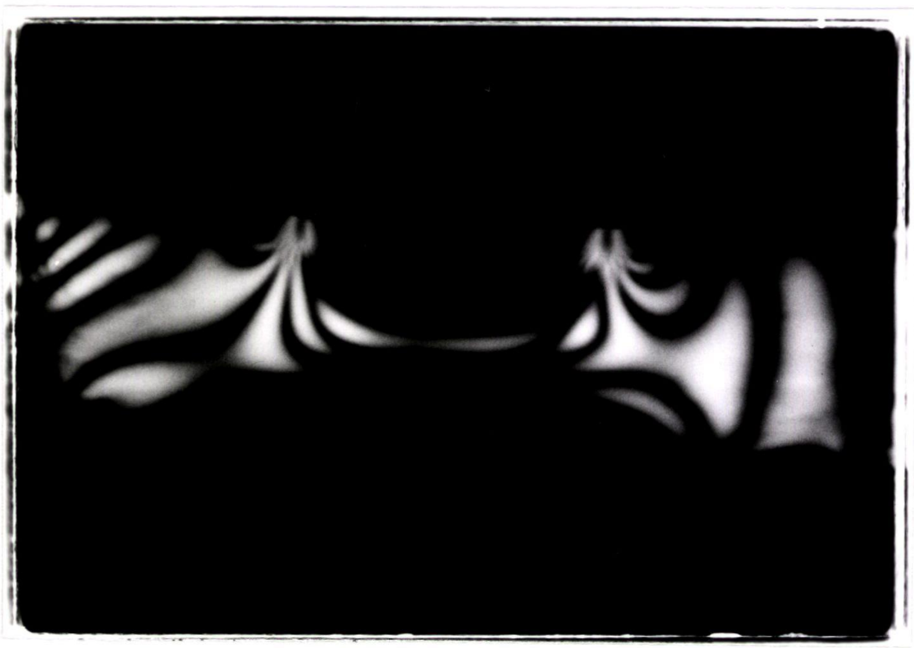

Figure 5.2: 0° Isoclinics for Calibration Specimen.

calculated by substituting the known values of σ_x and N into equation 2.23,

$$\sigma_x - \sigma_y = N\ f_\sigma/t$$

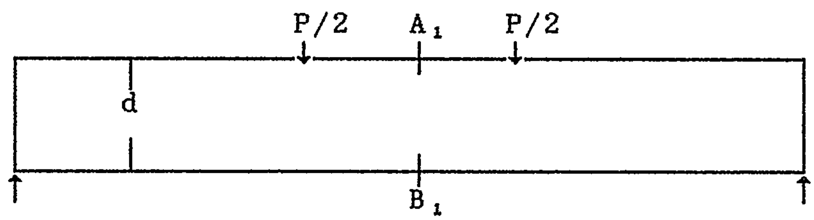

Figure 5.3: Loaded calibration specimen with analysis points A_1 and B_1.

$\sigma_y = 0$ at $y = \pm\ d/2$ where, d = depth of beam specimen

Therefore,

$$\sigma_x = N\ f_\sigma/t$$

For the beam specimen shown in figure 5.3, fringe constant values were averaged for points B_1 and A_1 in tension and compression. For the first batch of composite models cast, fringe constant value was calibrated as 0.44 kPa/fringe/m or 2.43 psi/fringe/in.

5.2 Analysis of Slices

The composite models tested were of a fiber volume fraction equal to 40 percent. Two identical models (model A

& model B) were loaded to 2160 $\pm$ 44 N (485 $\pm$ 10 lb) while stress freezing took place. During slicing of model 'A', slices S_2 and S_4 were lost in cutting. These either broke or delaminated while slicing. However, the second model 'B' was salvaged completely. Combined with available information from model 'A', a total of 10 slices were analysed. Isochromatic fringe patterns and 0° Isoclinics for these slices were photographed. 0° Isoclinics appear as dark portions/bands superimposed on the isochromatic fringe patterns. These fringe patterns are shown in figure 5.5 to 5.23.

Figure 5.4 shows the lines along which photoelastic analysis was conducted. In this study these lines are referred to as analysis lines. Analysis lines AA', CC' and EE' give stress distribution in the three fiber plane where as analysis lines BB' and DD' show stress distribution in the two fiber plane.

The fringe patterns shown in figures 5.5 to 5.23 contain stresses induced by external loading only. An unloaded slice that went through the same stress freezing thermal cycle was checked for thermal stresses. This slice when analysed in the polariscope was devoid of any fringes. Therefore, it can be concluded that the thermal stresses introduced during the

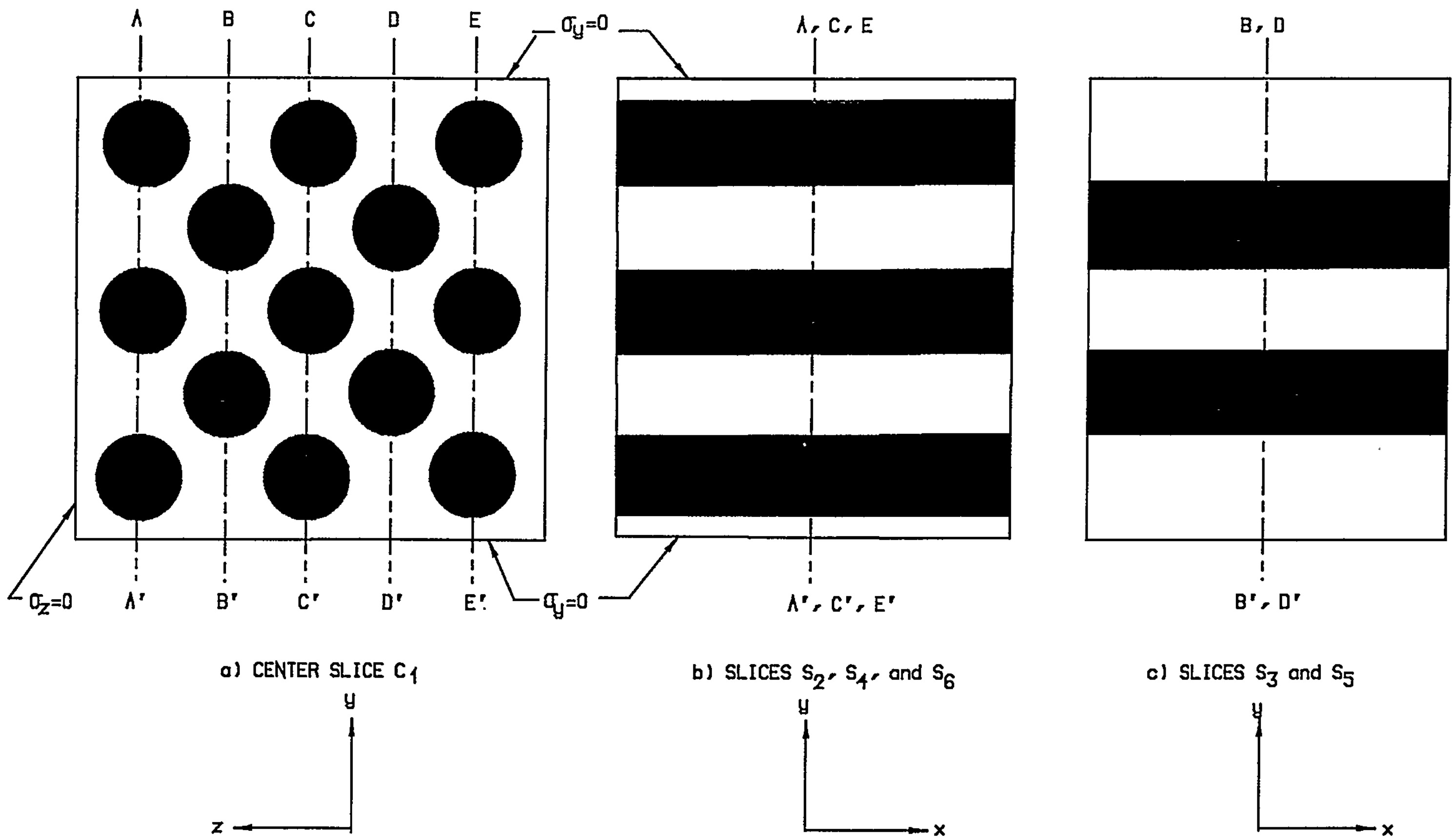

Figure 5.4: Lines along which stress analysis is possible in the composite model.

stress freezing cycle were negligible.

Slice C_1

Figures 5.5 and 5.6 show the isochromatic fringes and 0° isoclinics for the slice normal to the fiber direction. Fringe pattern in this slice contains information about σ_y, σ_z and τ_{yz}. Combined with slices in the xy-plane these stresses can be separated. Though it would be highly desirable to have the stress distribution known in the whole of the slice. However, physical limitations restrict the analysis along lines AA', BB', CC', DD' and EE'. These analysis lines are shown in figure 5.4. Observing figure 5.6, it is obvious that these analysis lines fall in 0° isoclinics. Therefore, slice C_1 is a principal slice/plane, and, σ_y and σ_z are principal stresses.

Starting from the top edge $\sigma_y=0$, σ_y can be determined by employing the method described in section 2.4. Difficulty arises as soon as the first fiber is encountered along any of the analysis lines. Because of these discontinuities encountered, fringe order between the fibers cannot be established with certainty. Therefore, to separate σ_y and σ_z in this slice, one of the following is needed:

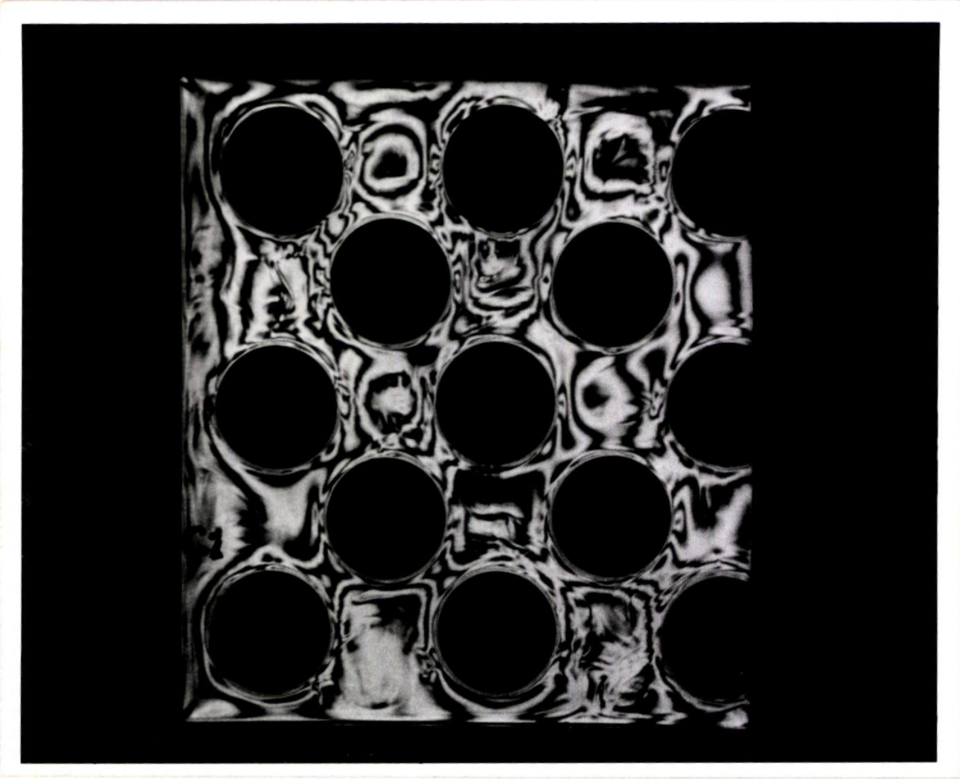

Figure 5.5: Isochromatic fringe pattern for slice C_{1A}.

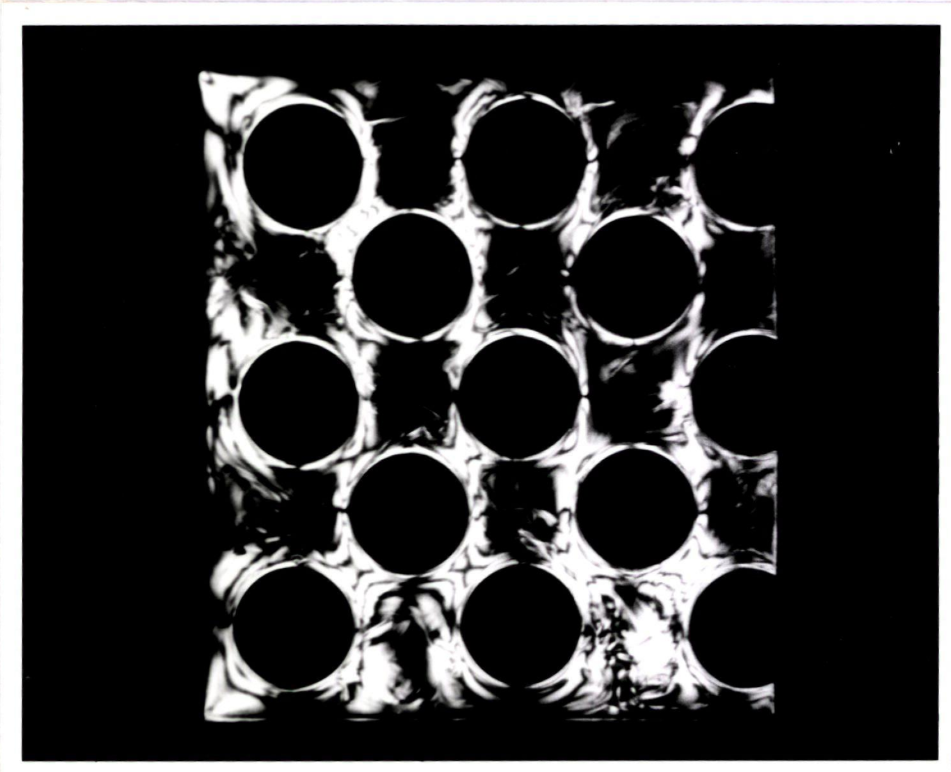

Figure 5.6: 0° Isoclinics for slice C_{1A} (model A).

- evaluate stress σ_y from the slices in xy-plane. Based on some logical assumptions assign fringe order to fringes in slice C_1. These assumptions can be based on a complimentary method of analysis such as finite-elements. Thus, knowing σ_y and fringe order N along analysis lines, σ_z can be evaluated from slice C_1.

- use a different material with relevant optical properties for reinforcing fibers. This will help in establishing a continuity of fringe pattern and fringe order. Thus making it possible to separate the stresses.

It will be seen later that the information from the xy-plane was not forthcoming. Therefore, the separation of stress σ_y and σ_z in the slice C_1 could not be carried out. Hence it can be concluded that reinforcing fibers with optical properties need to be used for a complete stress distribution analysis.

Slices S_{1A}, S_{1B} and S_{7B}

Isochromatic fringe patterns and 0° isoclinics for slices S_{1A}, S_{1B} and S_{7B} are shown in figure 5.7, figures 5.8 & 5.9, and, figures 5.10 & 5.11, respectively. Subscripts A

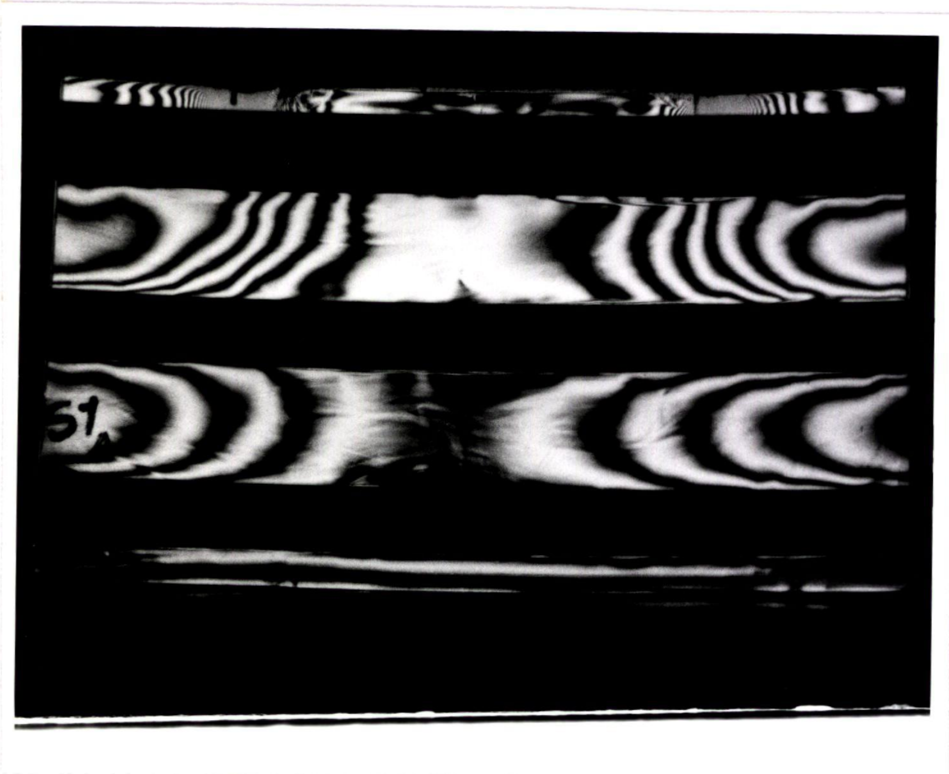

Figure 5.7: Isochromatic fringe pattern for slice S_{1A}.

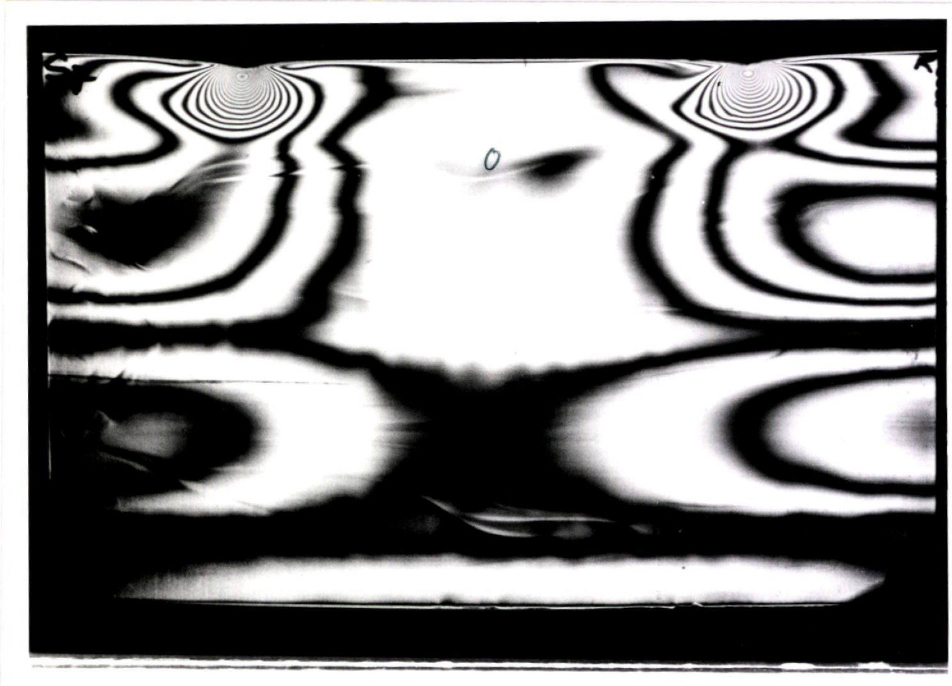

Figure 5.8: Isochromatic fringe pattern for slice S_{1B}.

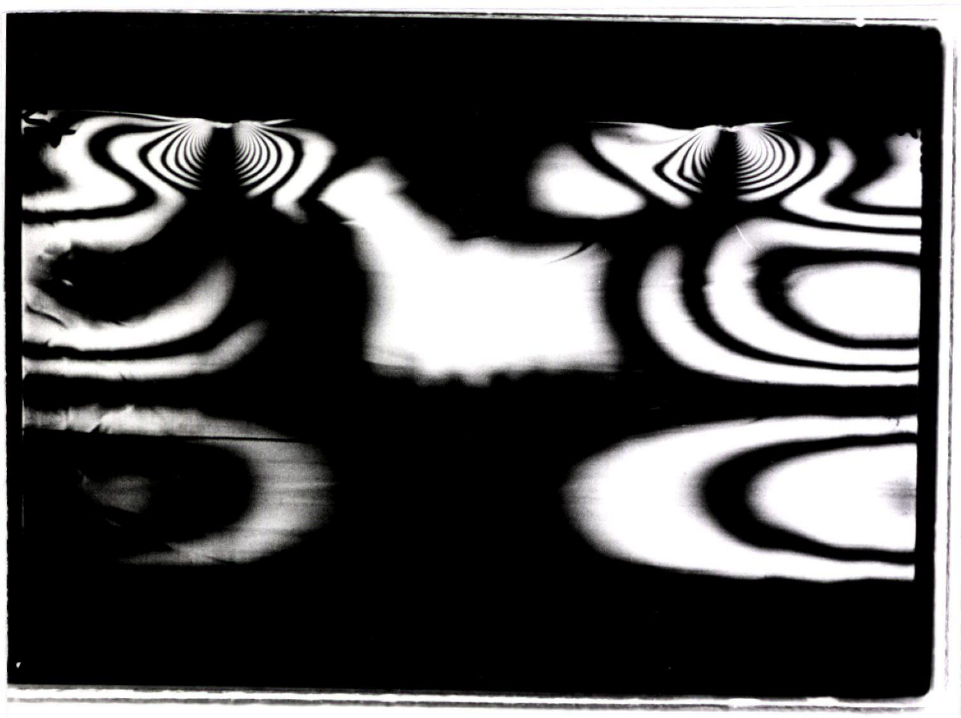

Figure 5.9: 0° Isoclinics for slice S_{1B} (model B).

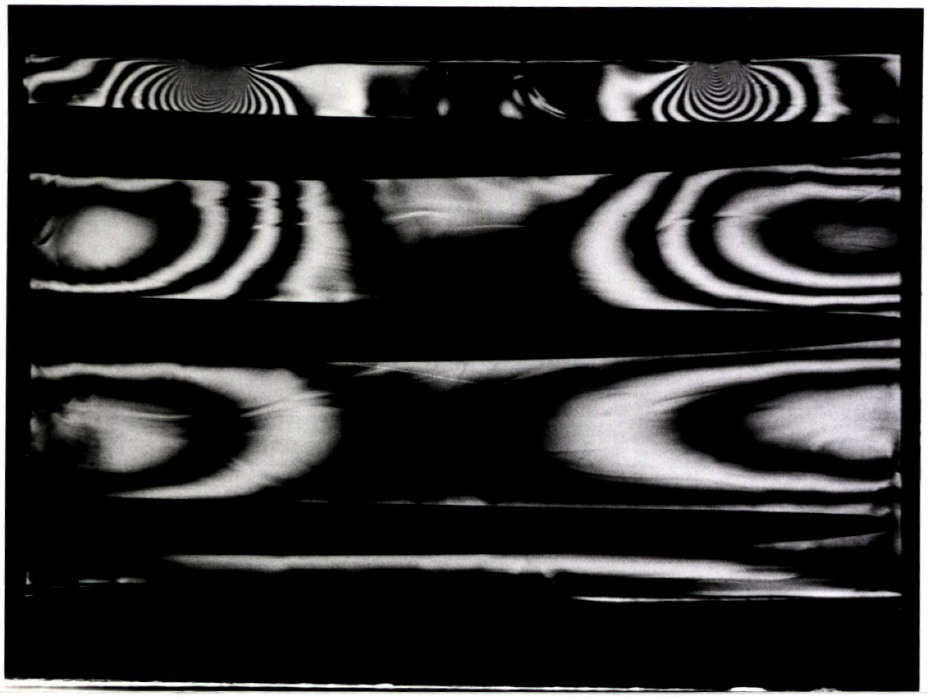

Figure 5.10: Isochromatic fringe pattern for slice S_{7B}.

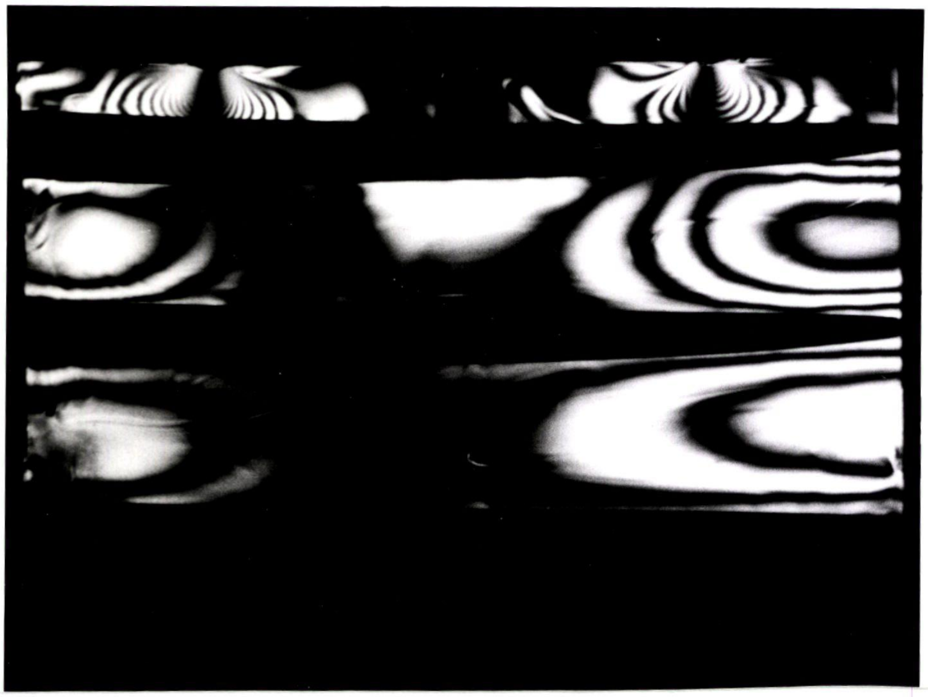

Figure 5.11: 0° Isoclinics for slice S_{7B} (model B).

and B refer to model A and model B. Slices S_{1A} and S_{1B} are from one side of the model and slice S_{7B} from the opposite side. They are comparable because of symmetrical loading and the geometrical symmetry of the cross-section. Slices S_{1A} and S_{7B} contain three fibers and are identical except for the thickness of the slice. Slice S_{1B} is just the matrix part removed from the edge of the model. All of these slices have one surface as the free edge of the model where $\sigma_z=0$. Also, because of varying position through thickness, the fringe patterns observed are at different points in the model. Therefore, slice S_{7B} should represent a fringe pattern that is compatible of one between slices S_{1B} and S_{1A}. Analysing the fringe pattern in figure 5.10 and comparing to those in figures 5.8 and 5.7, similarities are quite obvious. This helps substantiate the theory that slices removed from two identical models can be combined for analysis. These slices show that the fringe patterns change in a progressive manner. Photoelastic data obtained from these slices is tabulated in Table 5.1.

<u>Slices S_{2B}, S_{4B} and S_{6B}</u>

Isochromatic fringe pattern and 0° isoclinics for slices S_{2B}, S_{4B} and S_{6B} are shown in figures 5.12 & 5.13, figures 5.14 & 5.15, and figures 5.16 & 5.17, respectively. All these slices have three fibers passing through them.

Theoretically, fringe patterns in these slices should be identical. Especially in slices S_2 and S_6. But looking at figure 5.12, 5.14 and 5.16, this is not the case. Fringe patterns do have similarities but the number of fringes visible and the fringe orders are different. Slices S_{2B} and S_{6B} differ in their fringe patterns because the location of the slice varies. Both have the same thickness and are removed from adjacent positions along which slices S_{1B} and S_{7B} have been cut. Therefore, the analysis lines for slices S_{2B} and S_{6B} are not identically symmetrical. In other words, 6-8 mm thick slices cut are not exactly in the center of 12.7 mm thick fibers. Since three-fiber reinforcement dominates over that of a section with two-fibers, fringe pattern is sensitive to slight changes in position of slices. This means that extreme care must be taken in selecting the position of the slice to be cut. Unless the analysis dictates otherwise, the slice should always be removed from the center of the fiber thickness.

Assuming that slice S_4 is perfectly cut, it can be considered as a typical representation of the fringe pattern in a slice containing three fibers, since it is far removed from the free-edge effects. For stress analysis along lines AA', CC' and EE', stresses σ_x and σ_y have to be separated out. The region of most interest is the area between the

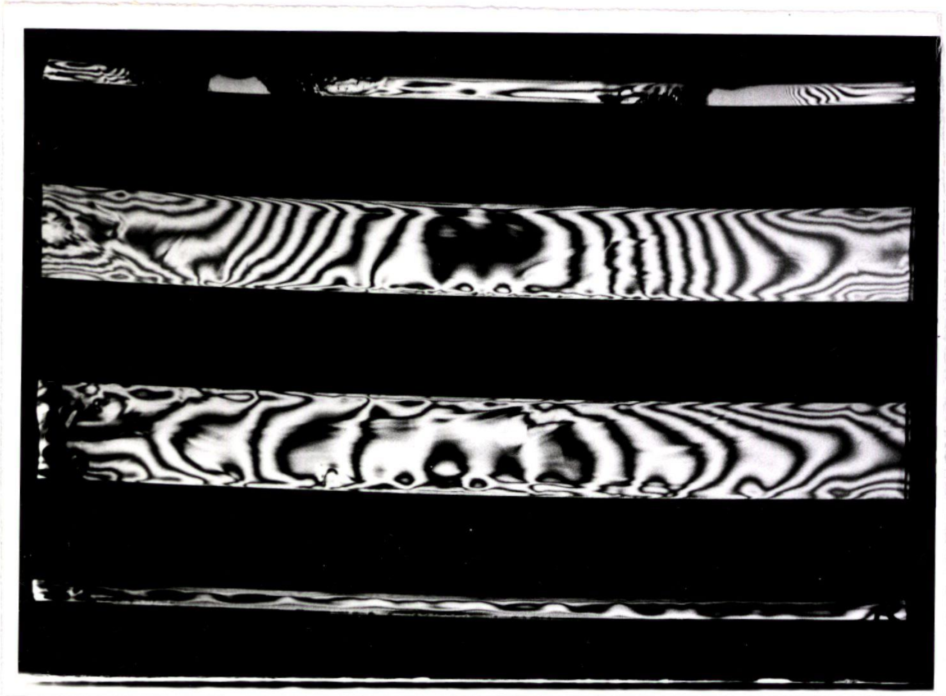

Figure 5.12: Isochromatic fringe pattern for slice S_{2B}.

Figure 5.13: 0° Isoclinics for slice S_{2B} (model B).

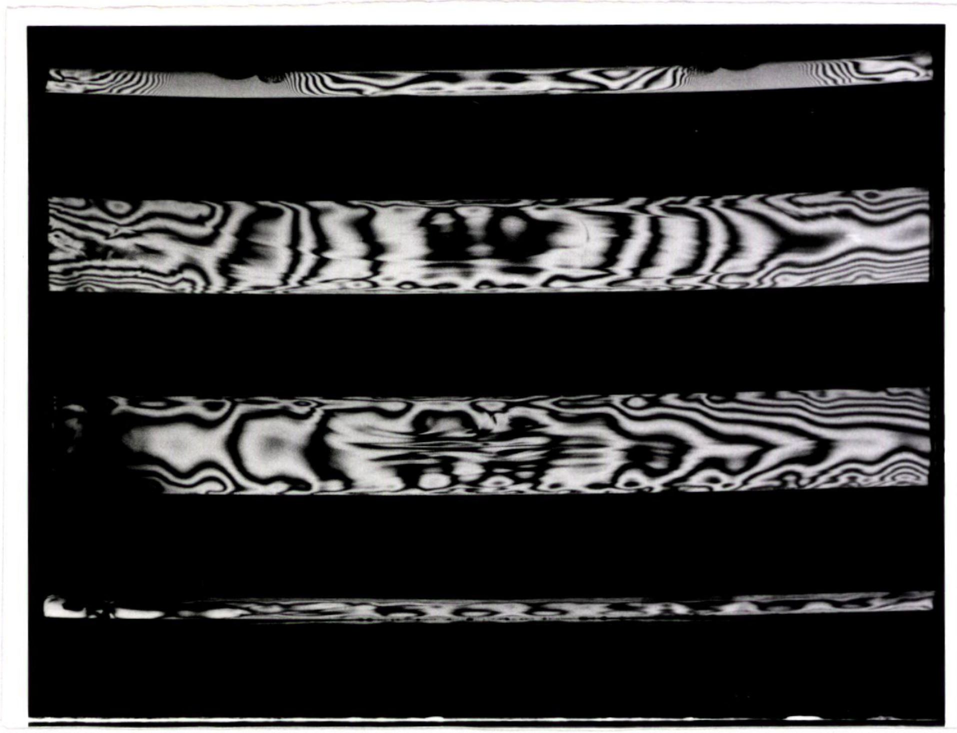

Figure 5.14: Isochromatic fringe pattern for slice S_{4B}.

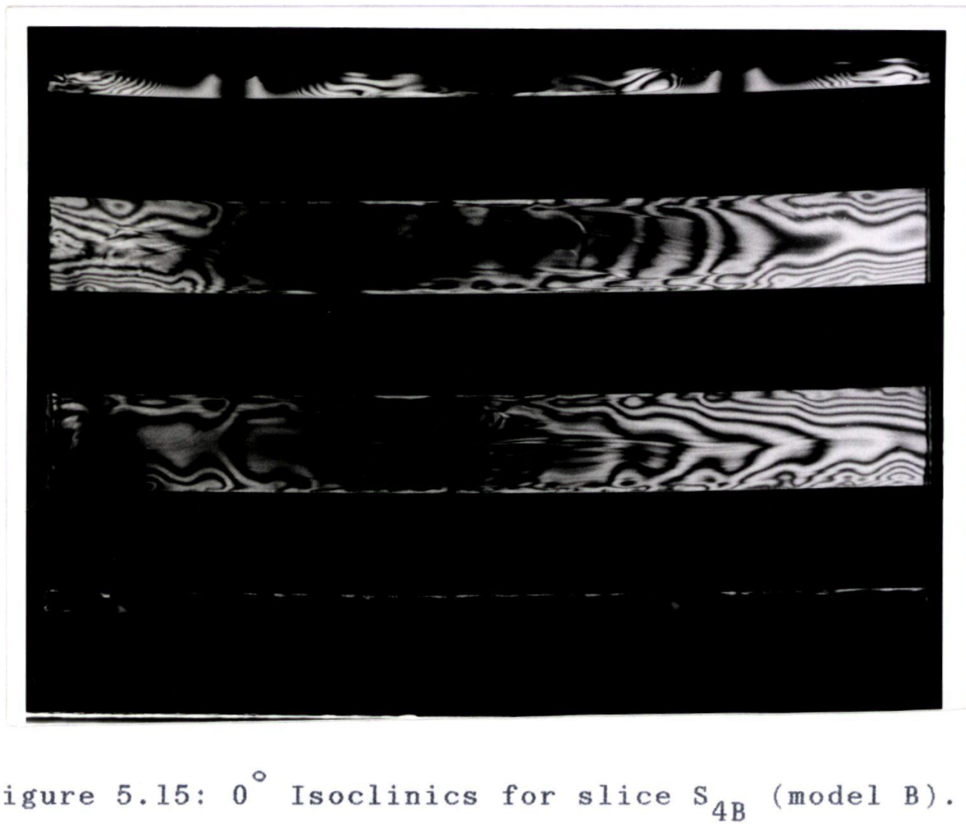

Figure 5.15: 0° Isoclinics for slice S_{4B} (model B).

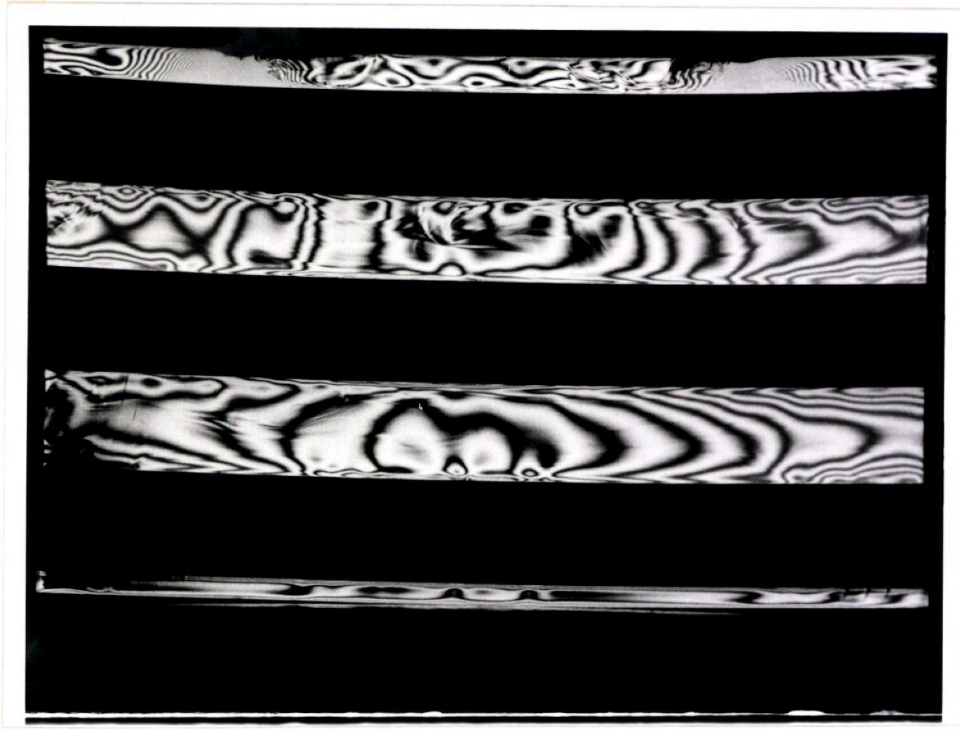

Figure 5.16: Isochromatic fringe pattern for slice S_{6B}.

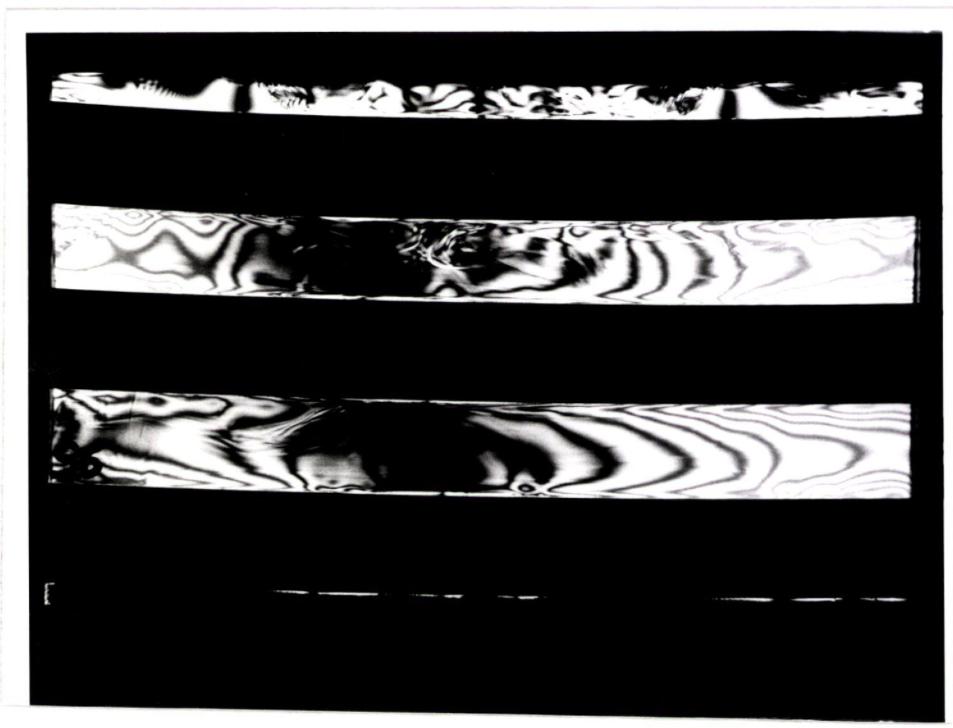

Figure 5.17: 0° Isoclinics for slice S_{6B} (model B).

fibers. The problem encountered here is again that of discontinuity of fringes. Also, because a zero-order black fringe was not observed, an assumption has to be made for a given fringe order. It can be assumed that the fringe in the center has a zero order. It is based on two reasons:

i) theoretically, due to the pure bending effect throughout the middle section, the shear stress should be zero. This is further confirmed by 2-D finite-element analysis for three-fiber slice in section 5.3.

ii) the fringe pattern in the x-direction on either side of the analysis line is totally symmetrical. Since the fringe order has to be continuous in both directions ($\pm x$), therefore, the fringe in the center has a common value for the fringe order.

Again further analysis is not possible due the discontinuities encountered in the fringe pattern.

Slices S_{3A}, S_{3B} and S_{5B}

These slices contain two reinforcing rods. Isochromatic fringe pattern and 0° isoclinics for slices S_{3A}, S_{3B} and S_{5B} are shown in figures 5.18 & 5.19, figures 5.20 & 5.21, and figures 5.22 & 5.23, respectively. Slice S_{3A} removed from model A represents half the fringe pattern of slices S_{3B} and S_{5B}. The fringe patterns are symmetrical about the middle i.e. analysis lines BB' and DD'. Fringe pattern in slice S_{3A} is compatible with that of slices S_{3B} and S_{5B}. Observing the fringe patterns in figures 5.18, 5.20 and 5.22, it confirms the earlier theory that slices from two identical models can be combined for analysis.

Comparing the fringe pattern in figures 5.20 and 5.22 it is clear that they are almost identical. This is to be expected as the slices are symmetrical about the center of the composite model. This also shows that the fringe pattern in slices with two fibers is less sensitive to the location of cut as compared to the one in slices with three fibers.

Slices S_{3B} and S_{5B} were the only ones in which a zero-order black fringe was visible. It was expected that this fringe would be located between the fibers since it would then be near the neutral axis due to geometrical symmetry. This would make it easier to interpret the exact location of neutral axis for the composite model. The FEM results confirmed this expectation.

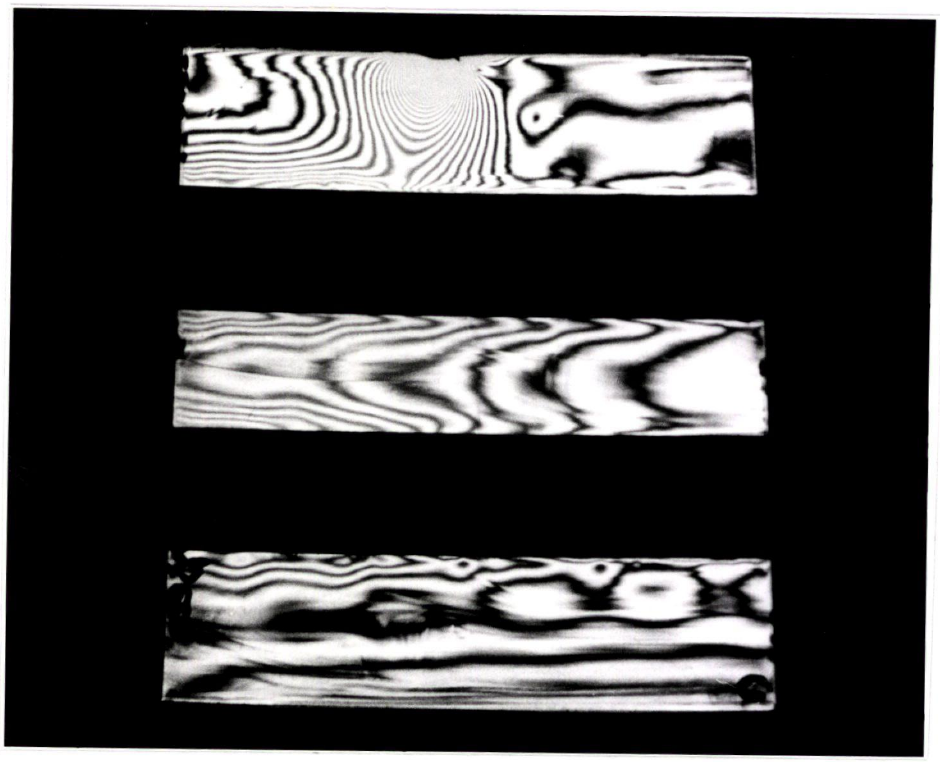

Figure 5.18: Isochromatic fringe pattern for slice S_{3A}.

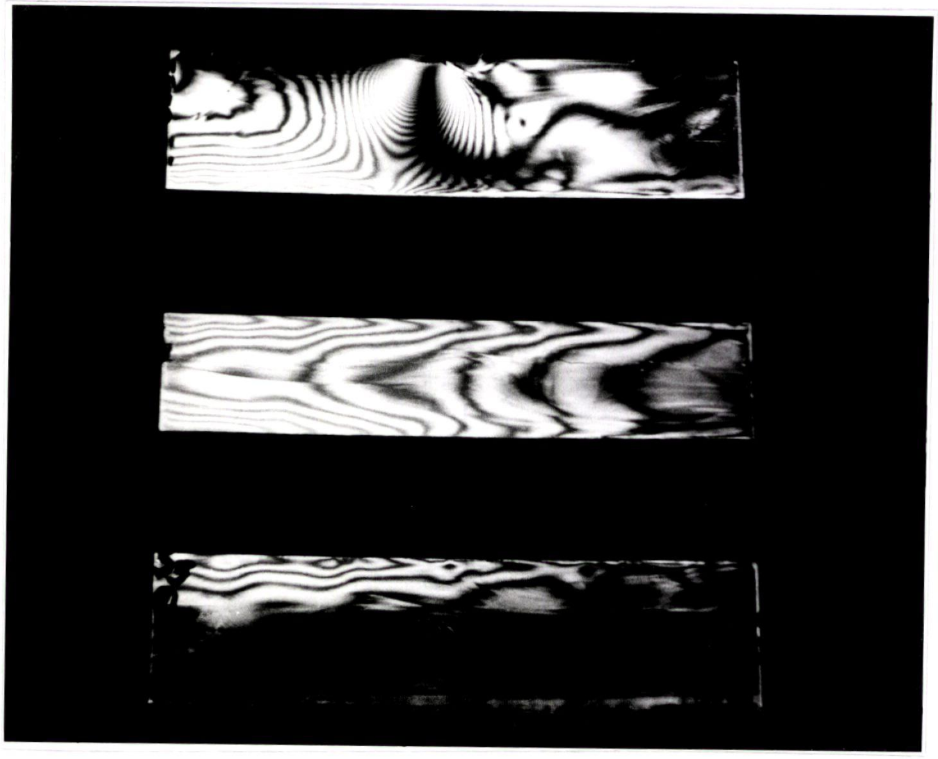

Figure 5.19: 0° Isoclinics for slice S_{3A} (model A).

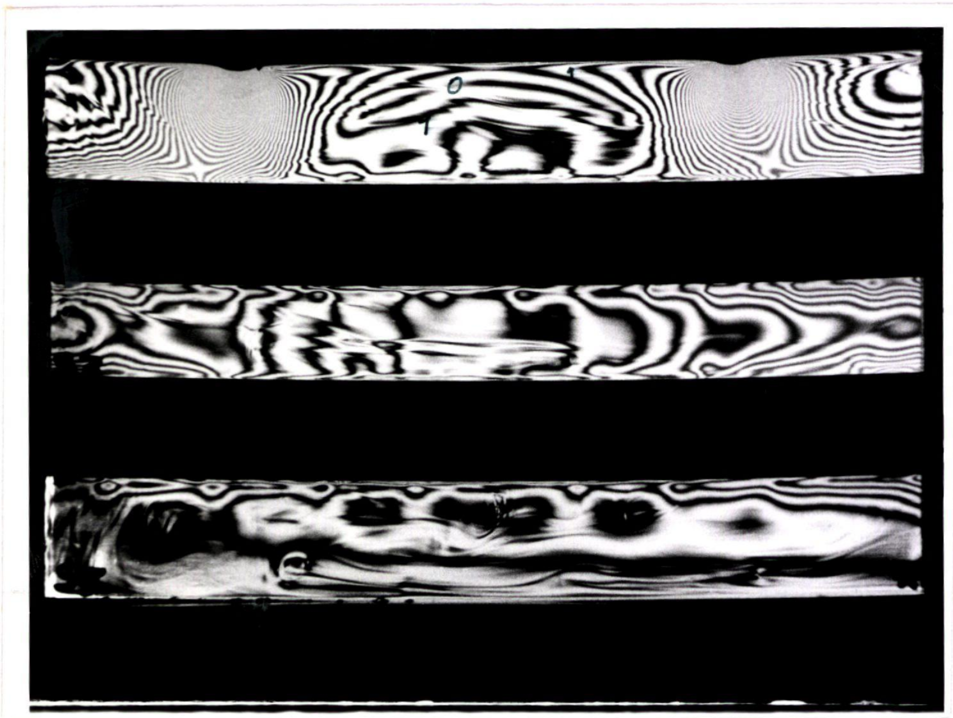

Figure 5.20: Isochromatic fringe pattern for slice S_{3B}.

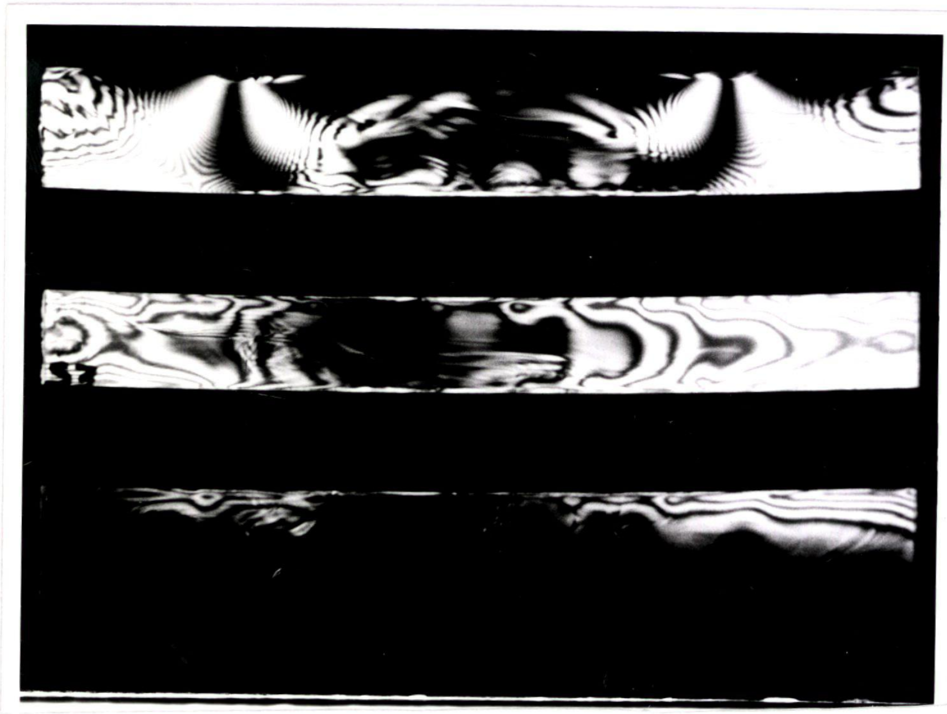

Figure 5.21: 0° Isoclinics for slice S_{3B} (model B).

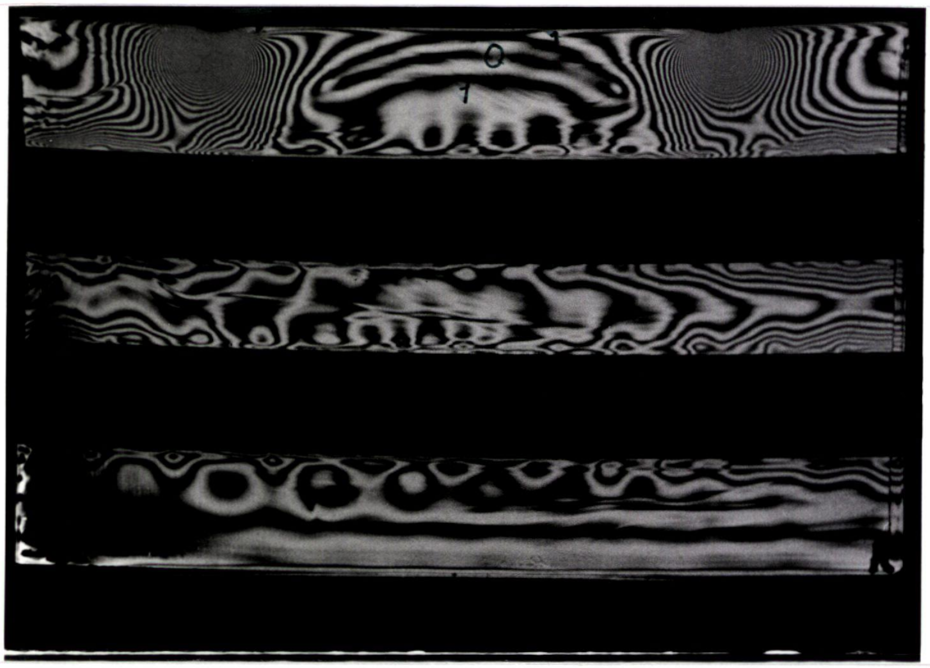

Figure 5.22: Isochromatic fringe pattern for slice S_{5B}.

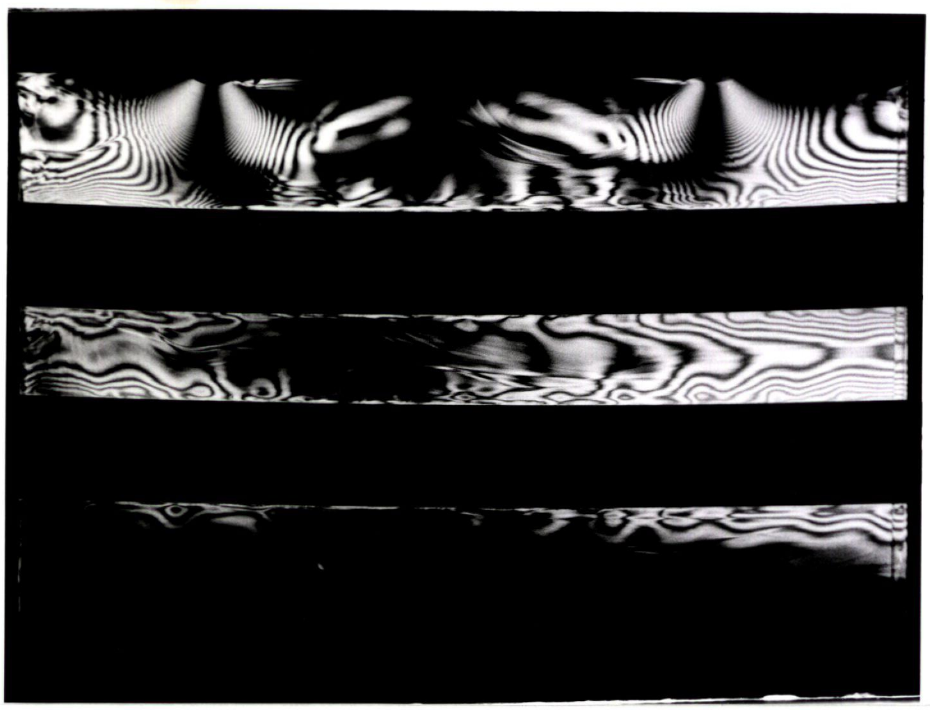

Figure 5.23: 0° Isoclinics for slice S_{5B} (model B).

The fringe pattern in the top portion of slices S_3 and S_5 can be analysed in two ways. Theoretically, the portion of matrix material bounded by the fiber and the two loading points should end up in compression. Observing the fringe pattern in the top portion of slices S_3 and S_5 in Figures 5.20 and 5.22. $\sigma_y=0$ at the top free-edge and the fringe pattern along the analysis line has 0° isoclinics. Therefore, the equation for σ_x at any point becomes:

$$\sigma_{xx}|_{x_1} = \sigma_{xx}|_{x_o} - \Delta\tau_{xz}|_{x_o+x_1/2}$$

Since there are no slices in the xz-plane, therefore, $\Delta\tau_{xz}$ values cannot be determined. It is also obvious that τ_{xz} cannot be zero, otherwise, it would indicate that σ_x can be determined from the fringe pattern in the top portion of slices S_3 and S_5. It would be theoretically impossible because the stresses associated with this particular fringe pattern change signs about the zero order fringe. Therefore, if the fringe pattern corresponded only to σ_x, it would result in the matrix in the top portion being in compression and tension. Since the above is theoretically impossible, it can be inferred that τ_{xz} cannot be zero and σ_y has to be known before the σ_x distribution can be evaluated.

The fringe pattern in the top portion of slices S_3 and S_5

has been rationalised above using theoretical methods. However, it has to be acknowledged that this is based on simple beam theory for a homogeneous material. Therefore, a distinct possibility exists that the fringe pattern and the stress reversal is real. This might be due to the strong influence of the surrounding three fiber planes on the two fiber distribution. But to confirm or prove any of the above interpretations more experimentation without discontinuities is needed for this particular behaviour to be studied.

Separation of Stresses for Slices in XY-Plane

To separate the stress σ_x and σ_y, one of the stress components has to be known at a point. It is known that $\sigma_y=0$ at the free edge. But the analysis cannot proceed much further because of the discontinuity encountered in the form of reinforcing rods. Observing the 0° isoclinics for these slices it is seen that the analysis lines fall under these dark bands. Therefore, these slices are principal planes and σ_x and σ_y principal stresses. With the fringe orders established, $\sigma_x - \sigma_y$ is given by equation 2.23.

Combined with slice C_1, results in

$$\sigma_x - \sigma_y = N_z f_\sigma / t$$

and,

$$\sigma_y - \sigma_z = N_x f_\sigma / t$$

It is obvious that more information is needed to solve for σ_x, σ_y and σ_z. Another equation is required to solve for the three unknowns. Therefore, to complete the analysis either one of the stress components has to be found by another complimentary method, or, the reinforcing rods should be changed for ones with optical properties.

The only point where stress σ_x can be evaluated is at the top free edge in slice S_{3B} and S_{5B}. Observing figures 5.20 and 5.22, $N \simeq 1$. Since $\sigma_y = 0$ at the free edge, substituting in equation:

$$\sigma_x - \sigma_y = N\ f_\sigma / t$$

σ_x can be evaluated. Thickness 't' for slices S_{3B} and S_{5B} is 7.35 mm and 7.65 mm respectively. Therefore, the average stress at the top edge is 59 kPa. While calculating the load desired for stress freezing, the stress at the top edge was calculated as 360 kPa for the two fiber plane and 103 kPa for the three fiber plane. As it can be seen a value of 360 kPa is not comparable to 59 kPa. One of the reasons for this descrepancy is the fact that simple transformed section theory was applied for the load calculation. Basically this calculation was performed only to approximate a load to stay in the elastic range. A better comparative study is carried out by using the results from the FEM analysis and the experimental photoelastic analysis.

Table 5.1 shows the photoelastic data from the composite model slices. Thickness of individual slices shown is after polishing. Most of the slices were about 7.3 to 7.8mm thick.

Table 5.1: Photoelastic data from composite model slices.

Slice	Thickness t, mm	Fringe Order N, at loading points Left	Right	Range of Fringe Order along Analysis Lines
Calib.1	7.75	> 8	> 8	0 - 6.2
C_1	5.15	N/A	N/A	0 - 3
S_{1A}	4.8-5.3	> 12	> 12	0 - 1
S_{3A}	6.40	N/A	> 22	0 - 2
S_{1B}	2.45	16	15	0 - 1
S_{2B}	7.80	*	*	0 - 2
S_{3B}	7.35	> 28	> 24	0 - 2
S_{4B}	7.35	*	*	0 - 2
S_{5B}	7.65	> 24	> 24	0 - 2
S_{6B}	7.80	*	*	0 - 2
S_{7B}	4.45	> 14	14	0 - 1

* - Not Resolvable.

Main exceptions being slices S_{1A}, S_{1B} and S_{7B}. This is because these slices were cut from the edge of the model. Maximum thickness that could have been achieved for slice S_{1B} was 3 mm, since it contains only the matrix part at the edge of the composite model. Fringe order N, at the left and right loading points is high because of stress concentrations at that point. Values shown are of maximum resolved fringe order. In most cases the actual fringe order was higher than what could be resolved. Along analysis lines in the slices in the xy-plane (slices S_i), fringe order varied from 0-2. The reason being that most of the loading is taken by the reinforcing rods. Therefore, the fringe order is low because stresses in the matrix are small as compared to the fibers.

In retrospect, even though the modelling based on stiffness ratio was satisfied, discontinuities in the stress field cannot be tolerated if a full field stress analysis is to be determined. Initially this problem was not fully appreciated since the interest was in the stress distribution in the matrix. Therefore, to perform a complete three dimensional stress analysis using photoelastic techniques, reinforcing fibers with photoelastic behaviour must be used.

5.3 FINITE ELEMENT ANALYSIS

Finite element analysis for the photoelastic composite model was undertaken for two reasons:

i) to be used as a complimentary method for photoelastic analysis. Primarily to get some starting points to help establish fringe orders in photoelastic fringe patterns.

ii) to study the applicability of finite element results in the overall analysis.

The finite element study for the composite model was done by using the finite element package ANSYS. Finite element analysis simulated the actual loading conditions of the composite model. Two-dimensional analysis simulated individual slices cut, whereas, three-dimensional analysis gave a rough approximation of the overall behaviour. For two dimensional analysis 2-D Isoparametric Solid elements were used. Each element was defined by four nodes and each node had two degrees of freedom. For three dimensional analysis 3-D Isoparametric Solid elements were used. Each node was defined by eight nodes and each node had three degrees of freedom. The degrees of freedom allowed were translation in x-, y- and/or z-direction. Fiber and matrix behaviour was simulated by assigning different stiffness values to the corresponding elements. The stiffness values assigned were the measured values of Young's modulus of the fiber and matrix material at the stress freezing temperature.

Two dimensional finite element analysis was carried out for both two fiber and three fiber slices. Two fiber analysis simulated the behaviour of slices S_3 and S_5 as shown in figure 5.24. Three fiber analysis simulated the behaviour of slices S_2, S_4 and S_6 as shown in figure 5.25. The analysis was done as a thin beam loaded in four-point bending with the thickness being 6.4 mm (1/4"). Loads were calculated by dividing the total uniformly distributed load into individual slices. Results and stresses shown are for the region along the analysis lines described earlier.

5.3.1 Two-Dimensional Analysis

Three Fiber Analysis

Finite element analysis for the three fiber plane simulated the behaviour of slices S_2, S_4 and S_6. Finite element mesh used to model the slices is shown in figure 5.26. This mesh consisted of 378 nodes and 338 elements.

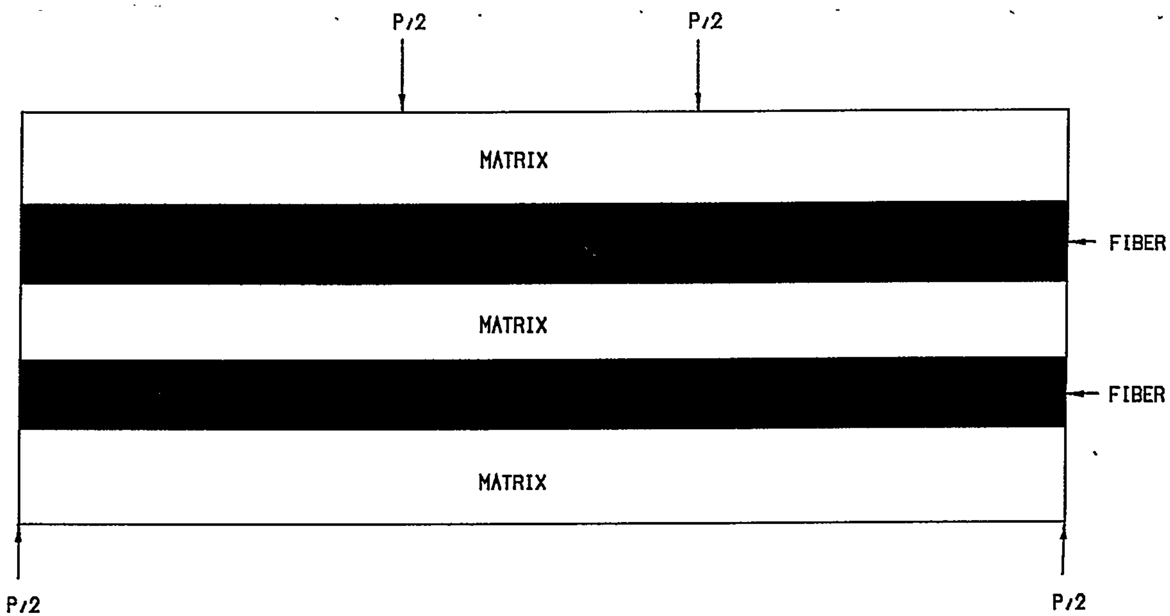

Figure 5.24: Two-dimensional section of configuration used for finite element model of slices S_3 and S_5.

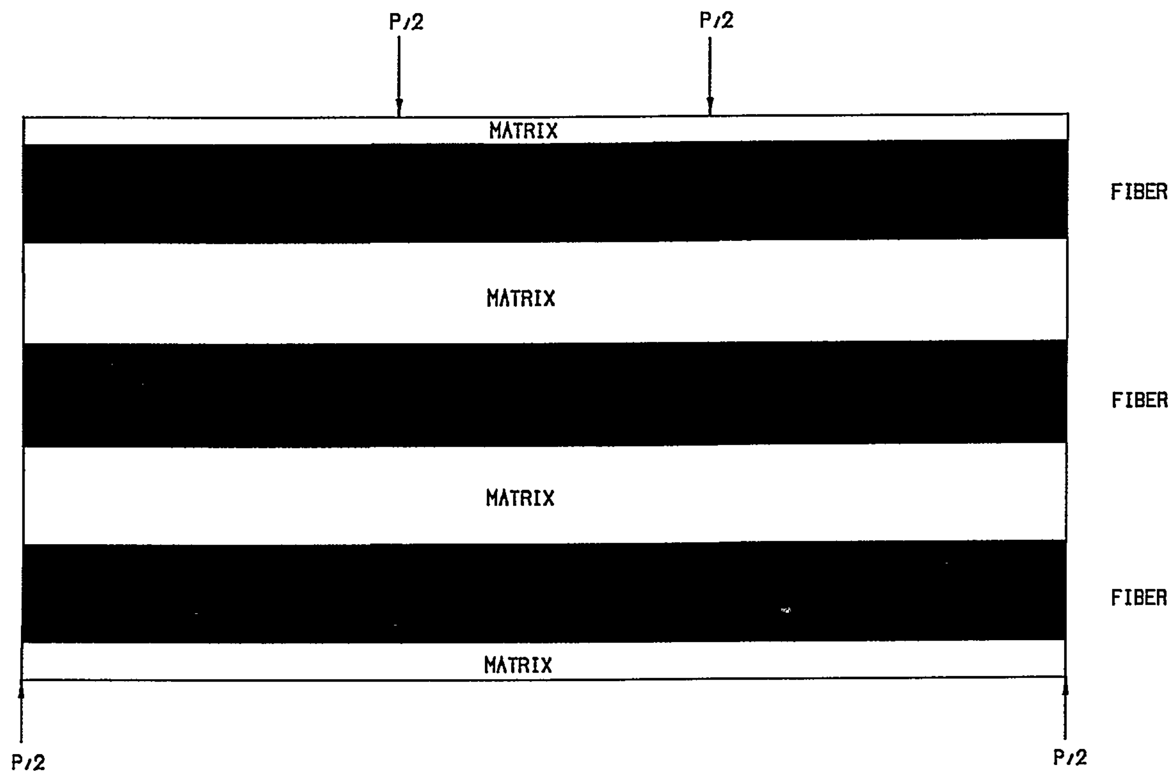

Figure 5.25: Two-dimensional section of configuration used for finite element model of slices S_2, S_4 and S_6.

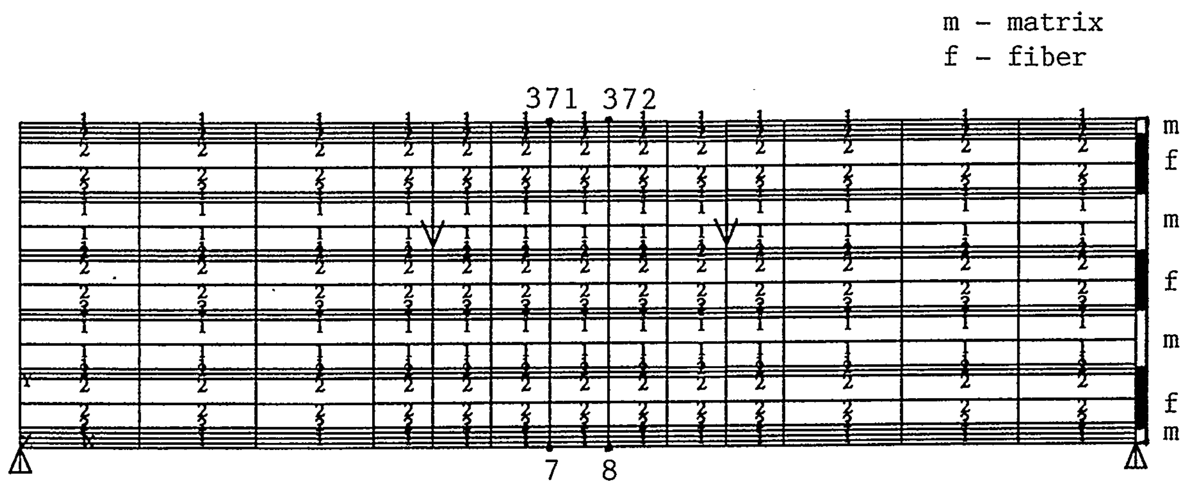

Figure 5.26: Finite element mesh for composite model slice with three fibers.

Elements marked 1 and 2 indicate the matrix and fiber sections. Arrows indicate the concentrated load of 89 N applied on nodes 369 and 374 at the top edge of the model. Lines connecting node 7 to node 371 and node 8 to node 372 simulate the analysis lines AA', CC' and EE' shown in figure 5.4. The stress distributions S_x, S_y and S_{xy} are plotted for these node numbers. Also, S_x and S_{xy} contour maps are plotted for comparison with the fringe pattern in the corresponding photoelastic slice. The stress distributions and contour maps are shown in figures 5.27 to 5.32. The distance marked on the x-axis is the distance along the analysis line measured from the bottom of the cross-section to the top. Therefore, as a beam, the stresses are plotted from the tensile to the compressive region.

Figures 5.27 and 5.28 show the S_x stress distribution in the complete section and along the analysis line AA'/CC'/EE', respectively. Observing figure 5.27 it is clear that the stresses are concentrated in the fibers. Figure 5.28 shows S_x to be maximum in the fibers. Stresses in the middle fiber are low because of the proximity to the neutral axis. Maximum stress in the fibers is $\simeq$ 700 kPa where as, maximum stress in the matrix is $\simeq$ 30 kPa. The Neutral axis as indicated by the zero stress level coincides with the centroid.

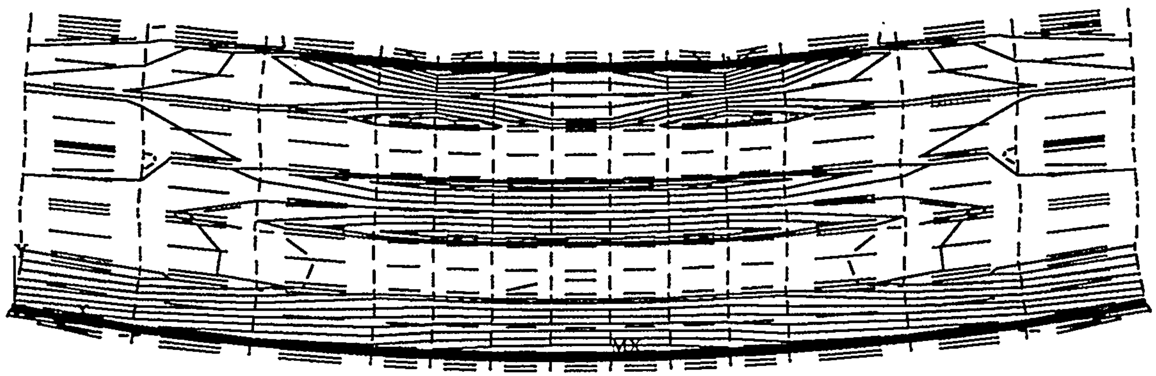

Figure 5.27: Average Sx distribution in composite model slice with three fibers (Sx stress contours).

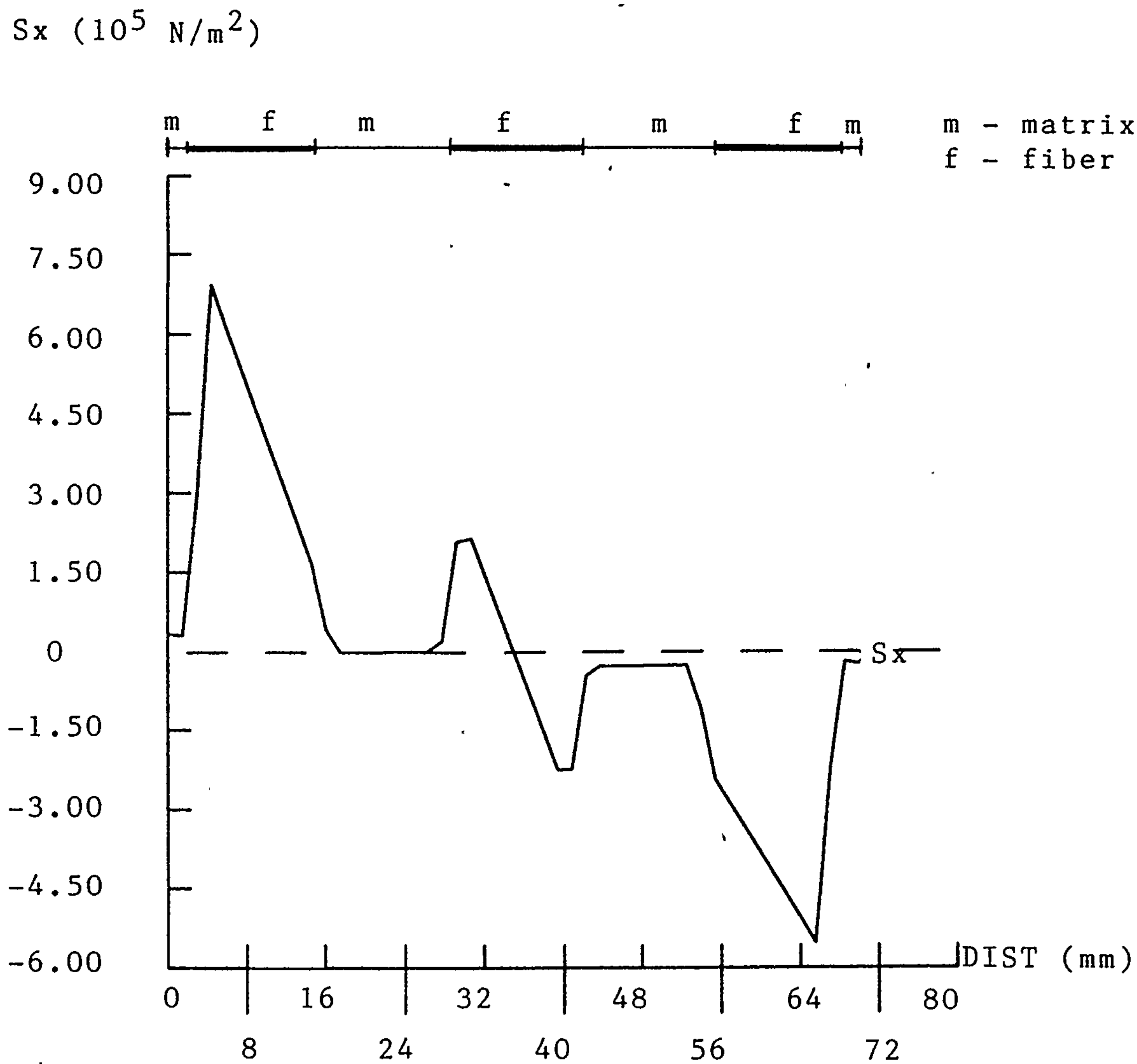

Figure 5.28: Sx distribution along the simulated analysis line in the three fiber slice.

Stresses in the matrix follow a linear distribution through the neutral axis. Stresses in the matrix are almost negligible in comparison to stresses in the fibers. This is especially true of the regions between fibers where the stresses are almost zero. The maximum σ_f/σ_m ratio is $\simeq$ 24 which is close to E_f/E_m = 26. This behaviour is as expected because of the strain compatibility between the two components.

The S_y stress along the analysis line is plotted in figure 5.29. The stress is zero at the bottom and maximum at the top. Theoretically, S_y should be also be zero at the top free edge. The reasons for such deviation are not apparent. In, general, the stress values are low and S_{ymax} is less than 3% of S_{xmax}.

The Sxy stress contours and stress distributions along the node numbers indicated are plotted in figures 5.30 to 5.32. Observing S_{xy} plots the values are almost negligible as compared to stresses in the x-direction. From figure 5.30 S_{xy} is zero in the middle (corrresponds to analysis line), and in general low in the pure bending region. Also, observing figures 5.31 and 5.32, S_{xy} values are equal in magnitude and opposite in direction on either side of the analysis line. This behaviour is expected and is in

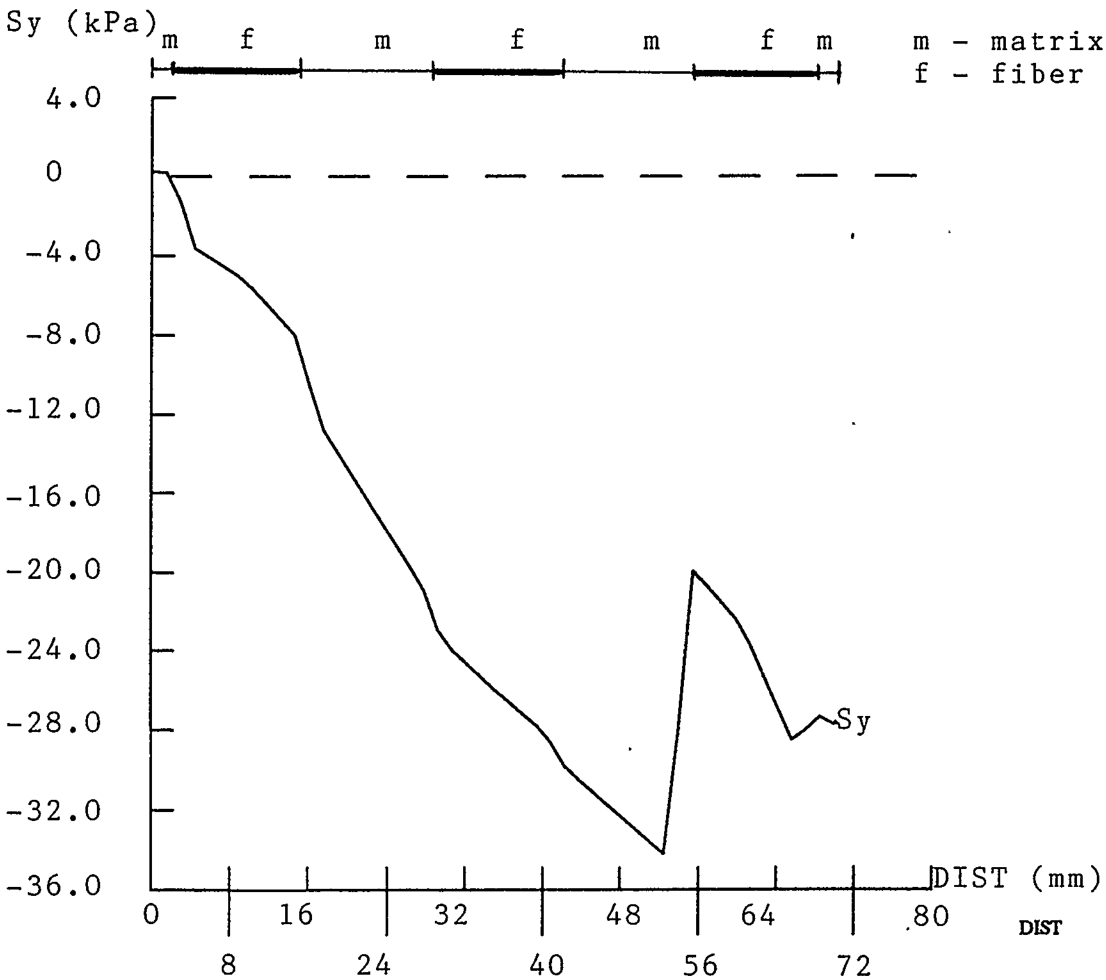

Figure 5.29: Sy distribution along the simulated analysis line in the three fiber slice.

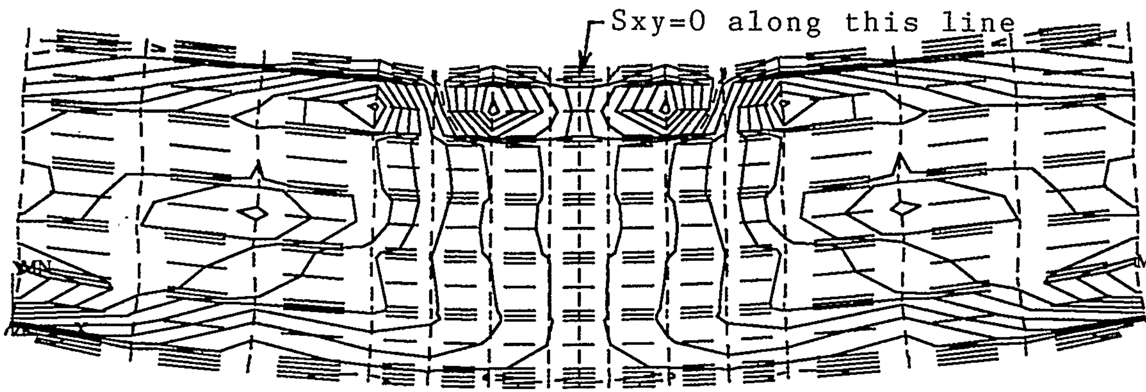

Figure 5.30: Average Sxy distribution in composite model slice with three fibers (Sxy stress contours).

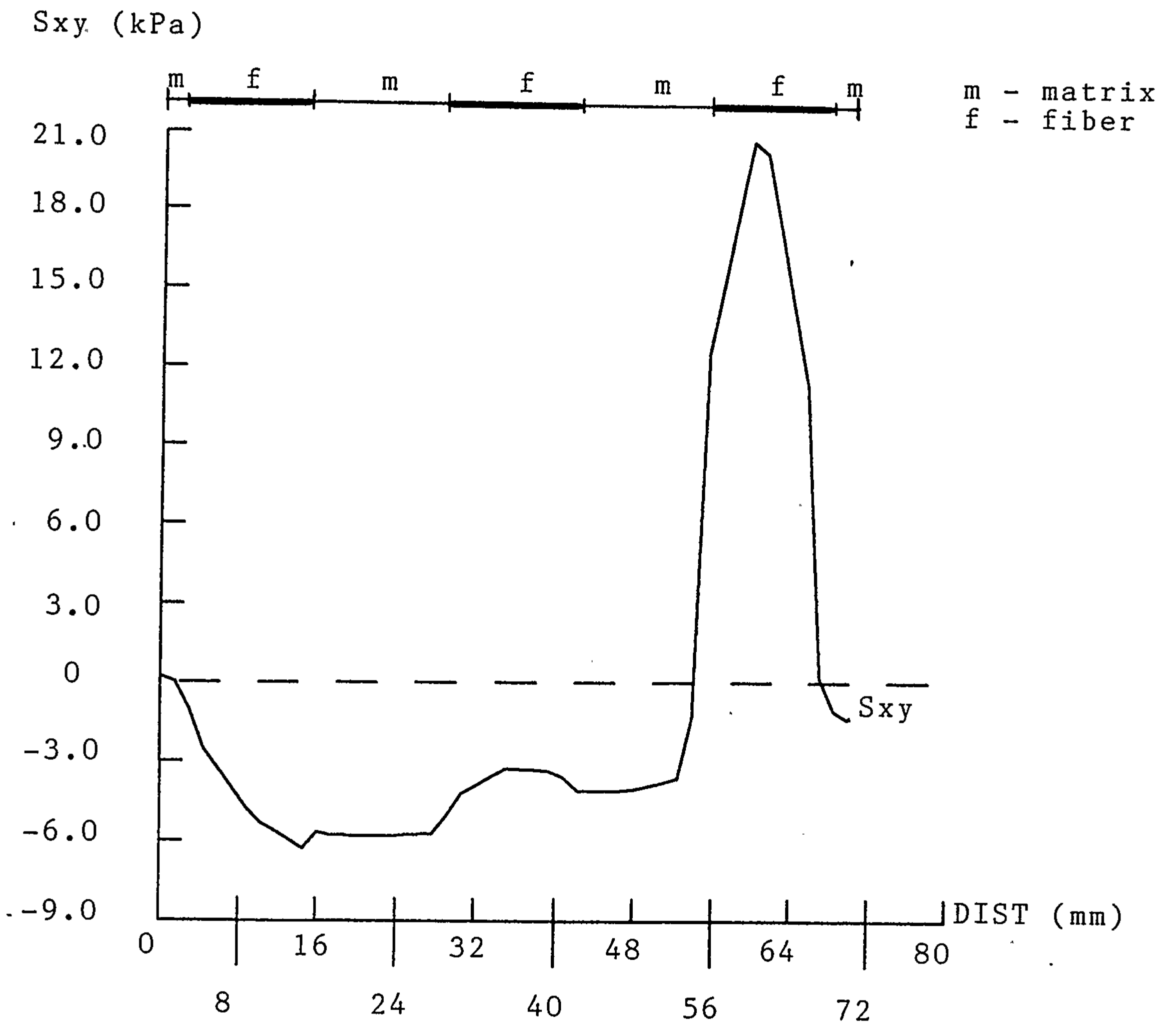

Figure 5.31: Sxy stress distribution along node 7 to node 371 to simulate the analysis line in the three fiber slice.

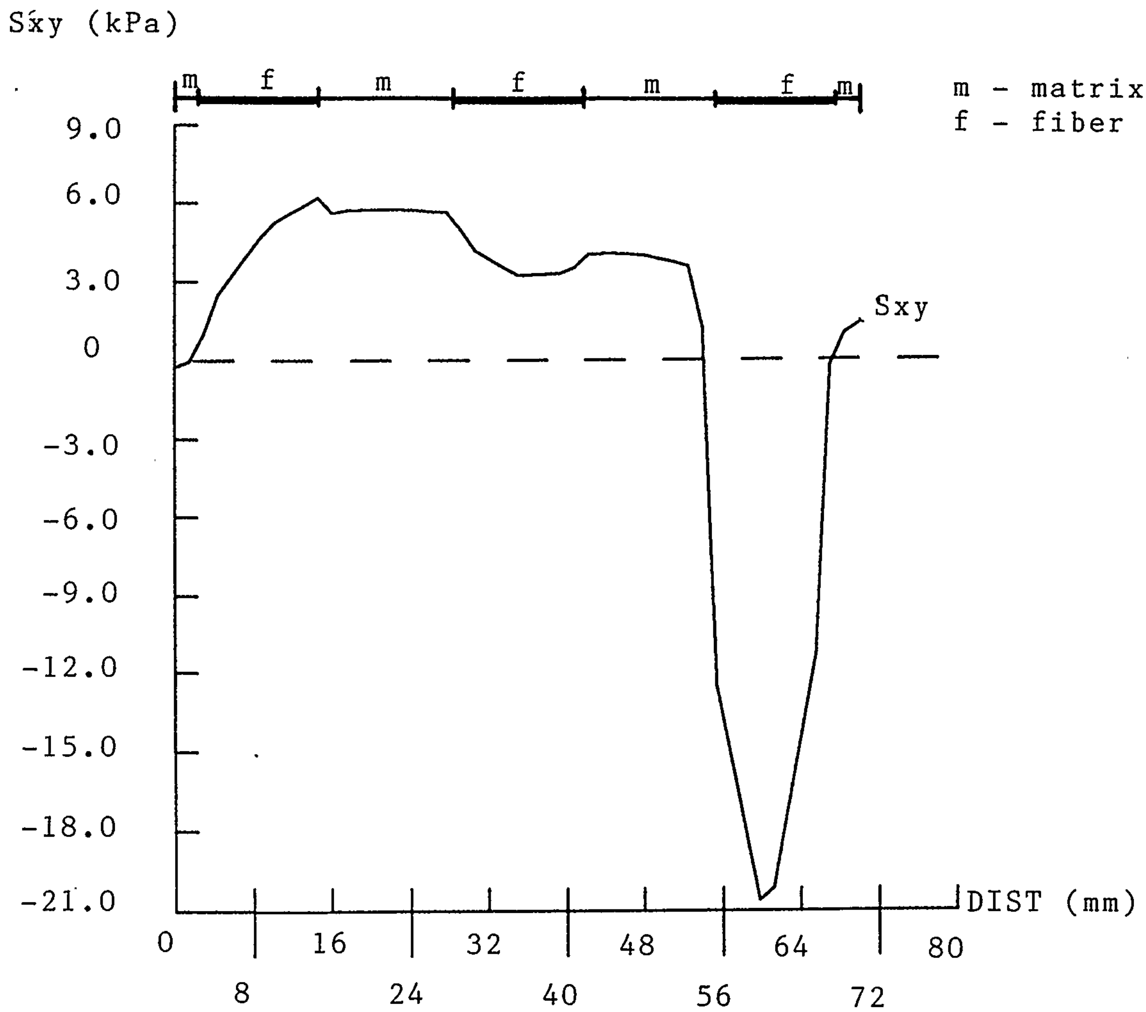

Figure 5.32: Sxy distribution along node 8 to node 372 to simulate the analysis line in three fiber slice.

agreement with the fringe pattern for slices S_2, S_4 and S_6. Since S_{xy} is zero in the center along the analysis line it can be concluded that away from the stress concentrations the shear stress is zero under pure bending.

Two Fiber Analysis

Finite element analysis for the two fiber plane simulated the behaviour of slices S_3 and S_5. Finite element mesh used to model the slices is shown in figure 5.33. This mesh consisted of 350 nodes and 312 elements. Elements marked 1 and 2 indicate the matrix and fiber sections. Arrows indicate the concentrated load of 89 N applied on nodes 341 and 346 at the top edge of the model. Lines connecting node 7 to node 343 and node 8 to node 344 simulate the analysis lines BB' and DD'. Stress distributions Sx, Sy and Sxy are plotted for these node numbers. Also, σ_x and τ_{xy} contour maps are plotted for comparison with the fringe pattern in the corresponding slices. The stress distributions and contour maps are shown in figures 5.34 to 5.39.

Figure 5.34 shows the S_x stress contours for the complete slice where as figure 5.35 shows the S_x stress distribution along analysis lines BB' and DD'. Again, observing figure

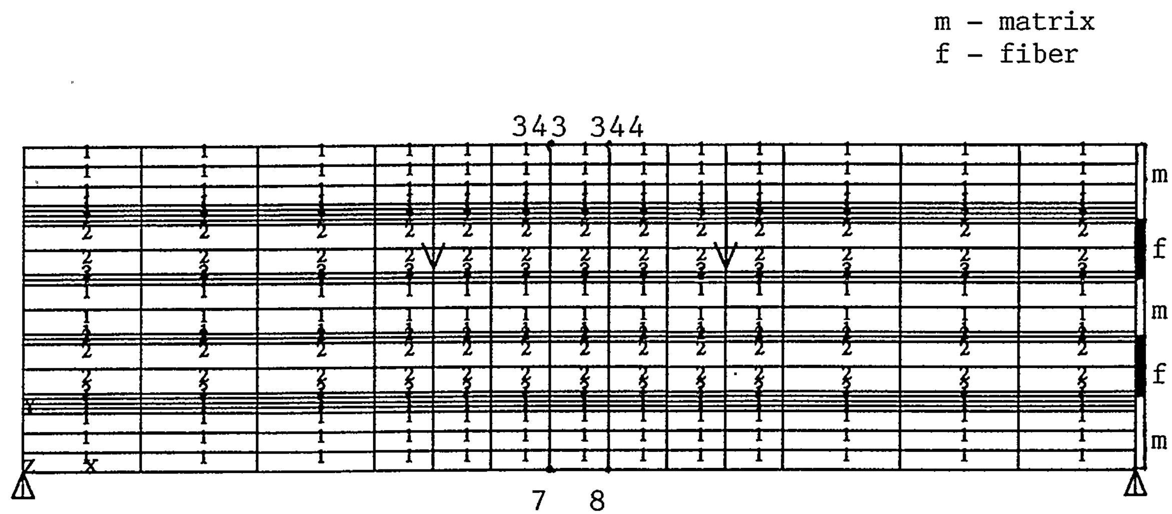

Figure 5.33: Finite element mesh for the composite model slice with two fibers.

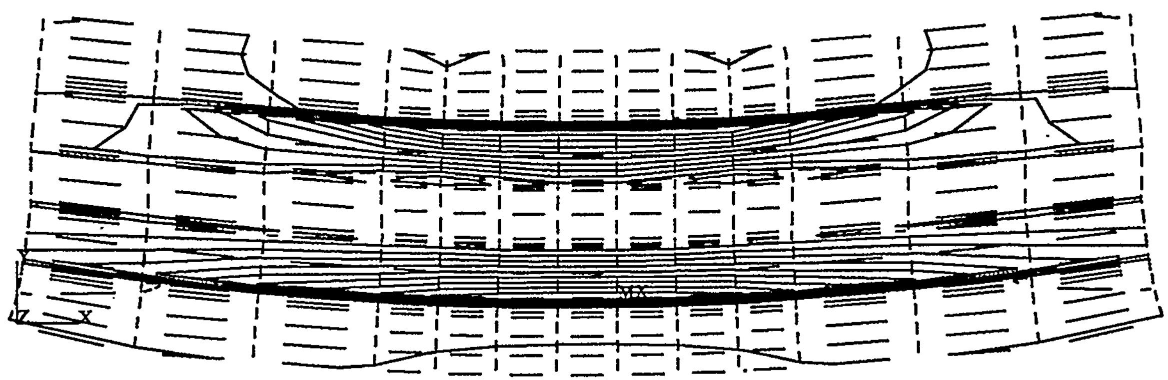

Figure 5.34: Sx_{avg} distribution in the simulated two fiber slice.

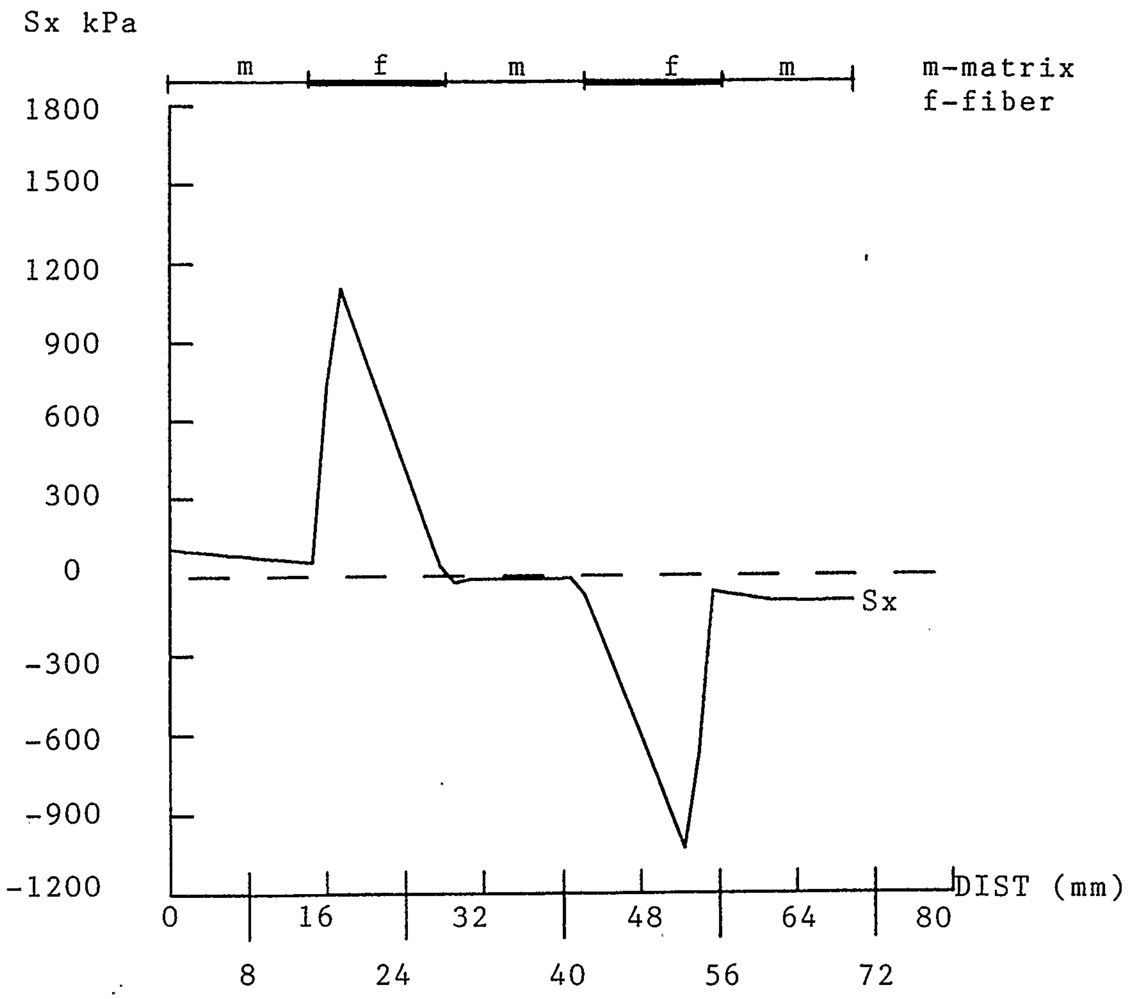

Figure 5.35: Sx distribution along the simulated analysis line in the two fiber slice.

5.34 it is obvious that stresses are concentrated in the fibers. Overall behaviour of two fiber slice is similar to that of three fiber slice. In figure 5.35 the maximum stress S_x in the fiber is $\simeq$ 1125 kPa which occurs in the top and the bottom fibers. In comparison, maximum stress in the matrix is $\simeq$ 100 kPa which occurs at the top and bottom end i.e. node 343&344 and node 7&8 respectively. This is to be expected as these two points are the farthest away from the neutral axis. Stresses in the matrix are linear and symmetrical about the neutral axis which coincides with the centroid. The S_x stress values are higher in the reinforcing fibers in the two fiber slice than in the three fiber slice. Since the majority of the loading is taken up by the fibers, the distribution of stresses in the two fibers is higher than in the three fibers for the loading condition used here.

The S_y stress distribution along analysis lines BB' and DD' is plotted in figure 5.36. Majority of the S_y stress values are less than one percent of S_{xmax} with S_{ymax} being approximately two percent. The change in S_y from compression to tension and back in compression has no theoretical explanation. Theoretically, the final S_y value should be zero at the free edge. Though it is not the case, stress is low enough to be assumed as such.

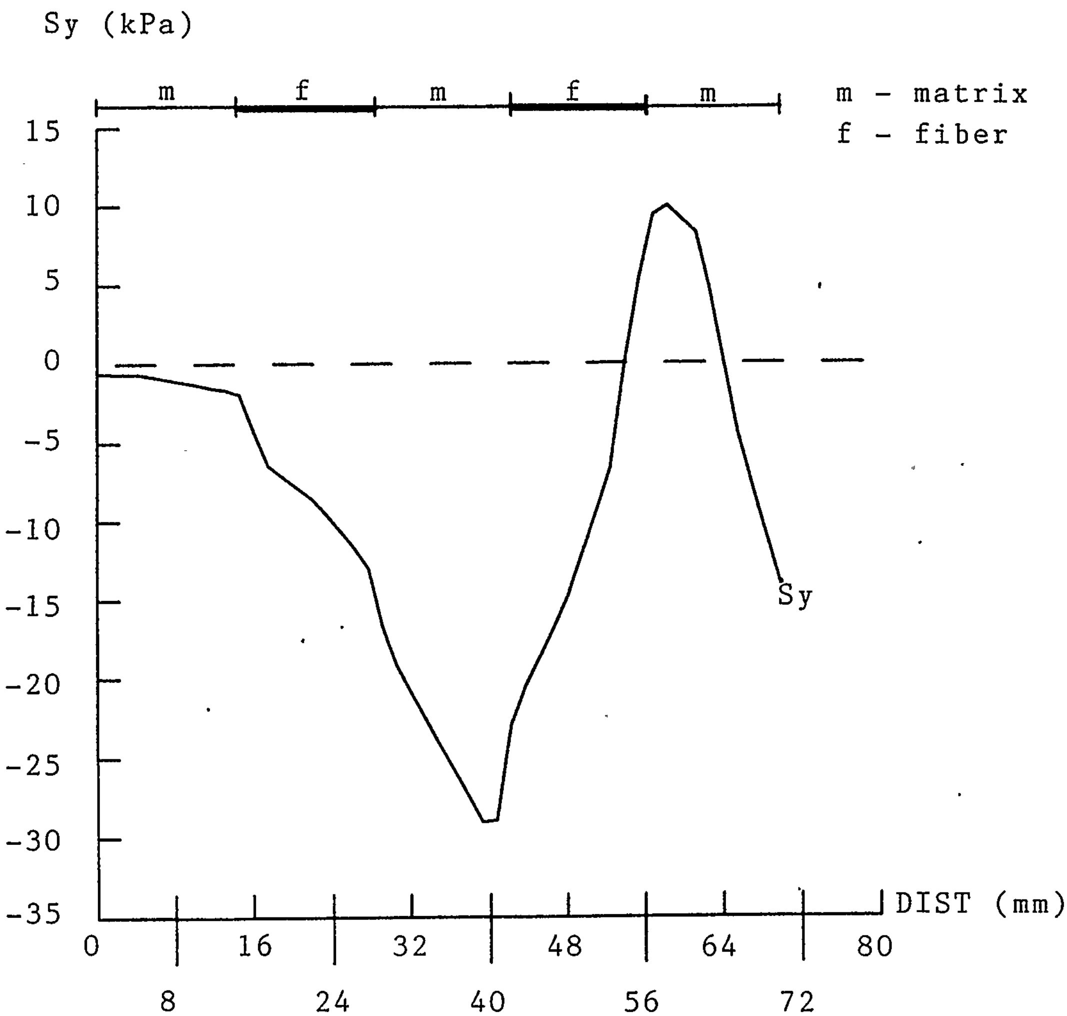

Figure 5.36: Sy distribution along the simulated analysis line in the two fiber slice.

The Sxy stress contours and stress distributions along the node numbers indicated are plotted in figures 5.37 to 5.39. Shear stress distribution in the two fiber slice is similar to that in three fiber slice. The shear stress S_{xy} is zero in the middle, and in general, low in the pure bending region. The S_{xy} values in figure 5.38 and 5.39 are within 0.5-1.8 percent of S_{xmax}. Again, observing figures 5.38 and 5.39, shear stress values are equal in magnitude and opposite in direction on either side of the analysis line. This behaviour is in agreement with the fringe pattern for slices S_3 and S_5.

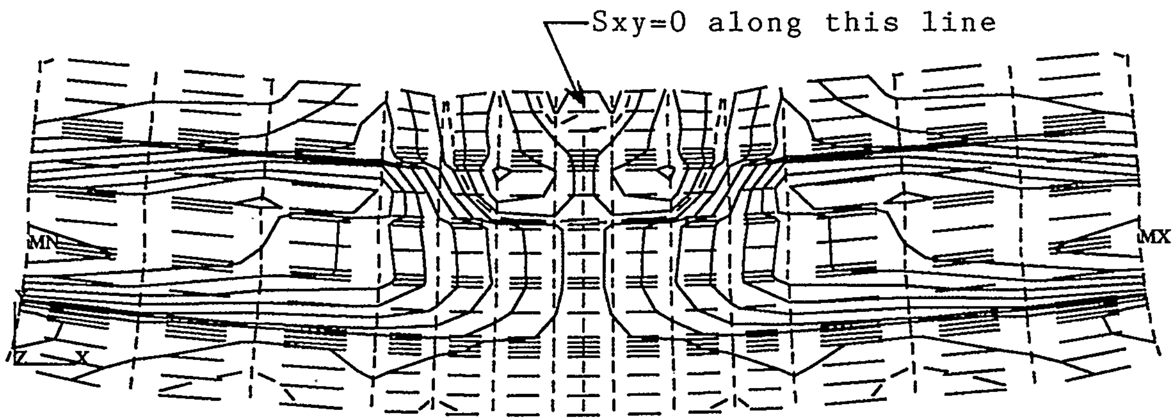

Figure 5.37: Average Sxy distribution in the composite model slice with two fibers (Sxy stress contours).

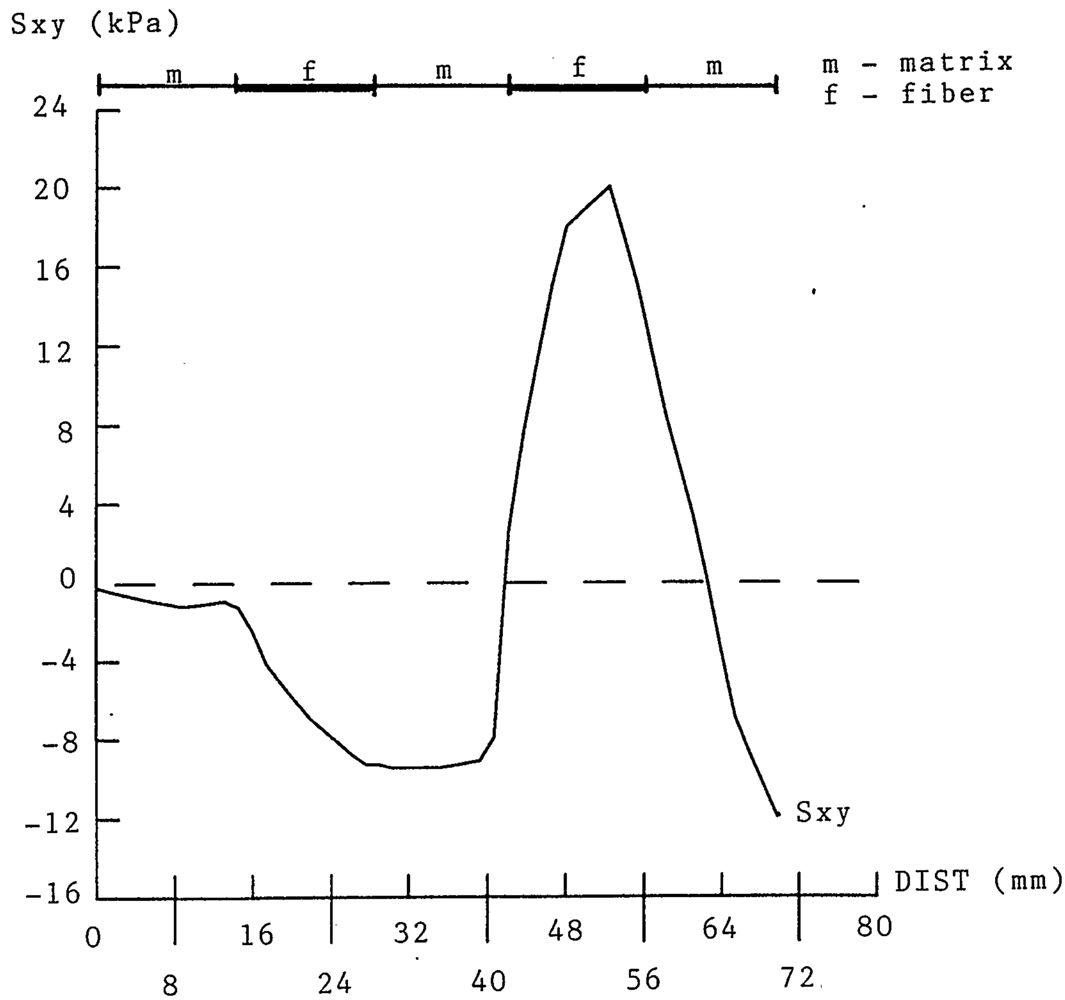

Figure 5.38: Sxy distribution along node 7 to node 343 to simulate the analysis line in the two fiber slice.

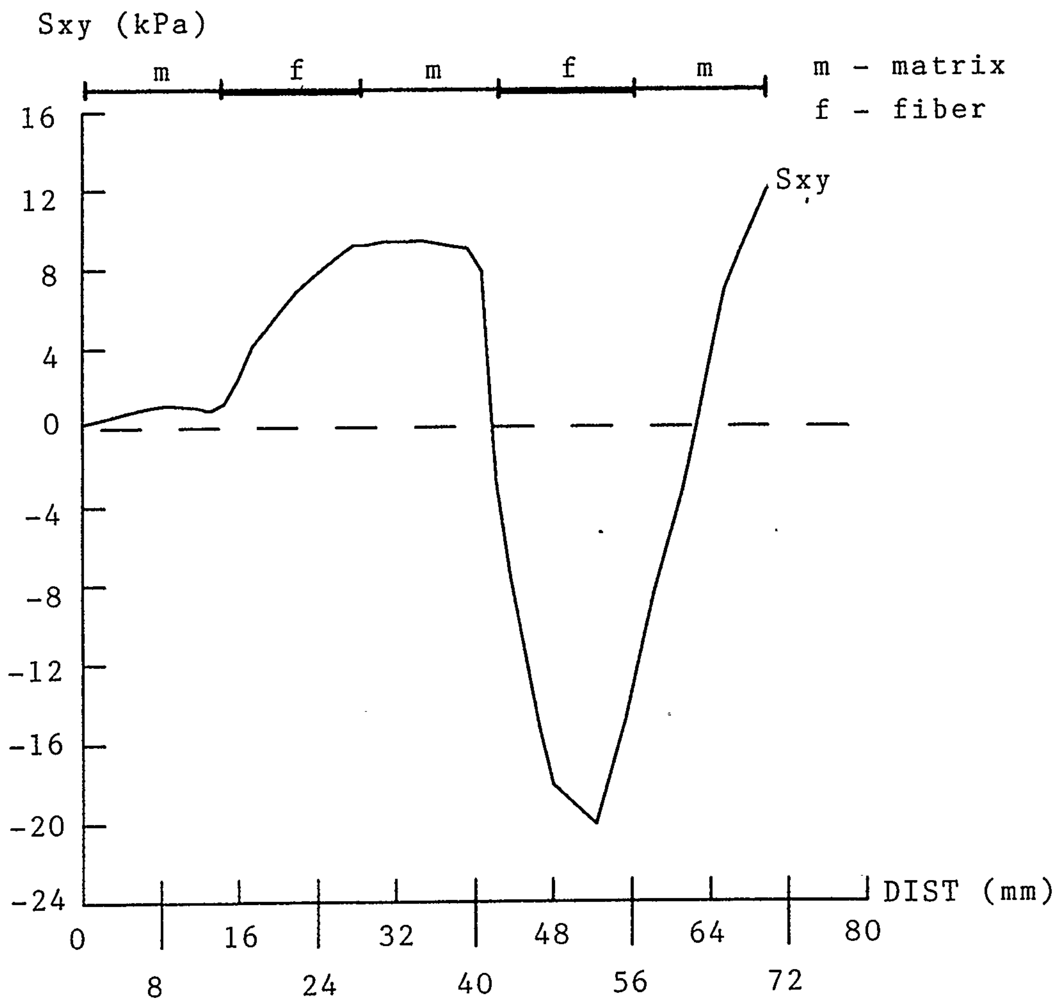

Figure 5.39: Sxy distribution along node 8 to node 344 to simulate the analysis line in the two fiber slice.

5.3.2 Three-Dimensional Analysis

Three-dimensional analysis was undertaken to acquire a whole field effect. Based on symmetry only a quarter of the composite beam was analysed. Also, due to computing power limitations the fibers were modelled as square fibers. The fiber volume fraction was kept constant at 40% by matching the cross-sectional area of the square fiber with the actual circular one. Spacing between the fibers was maintained at 12.7mm (1/2").

The finite element mesh used to model three-dimensional behaviour is shown in figure 5.40. This mesh consisted of 980 nodes and 702 elements. Elements marked 1 and 2 indicate the matrix and fiber sections. Line connecting node 869 to node 882 simulates the analysis line AA', node 911 to node 924 similates BB' and node 967 to node 980 simulates the analysis line CC'. Stresses S_x, S_y, S_z and S_{xy} plotted along lines AA', BB' and CC' are shown in figures 5.41 to 5.52. The distance marked on the x-axis is the distance along the analysis line measured from the bottom of the cross-section to the top.

In the finite element analysis major emphasis is on stresses in the x-direction. Due to the nature of loading applied in

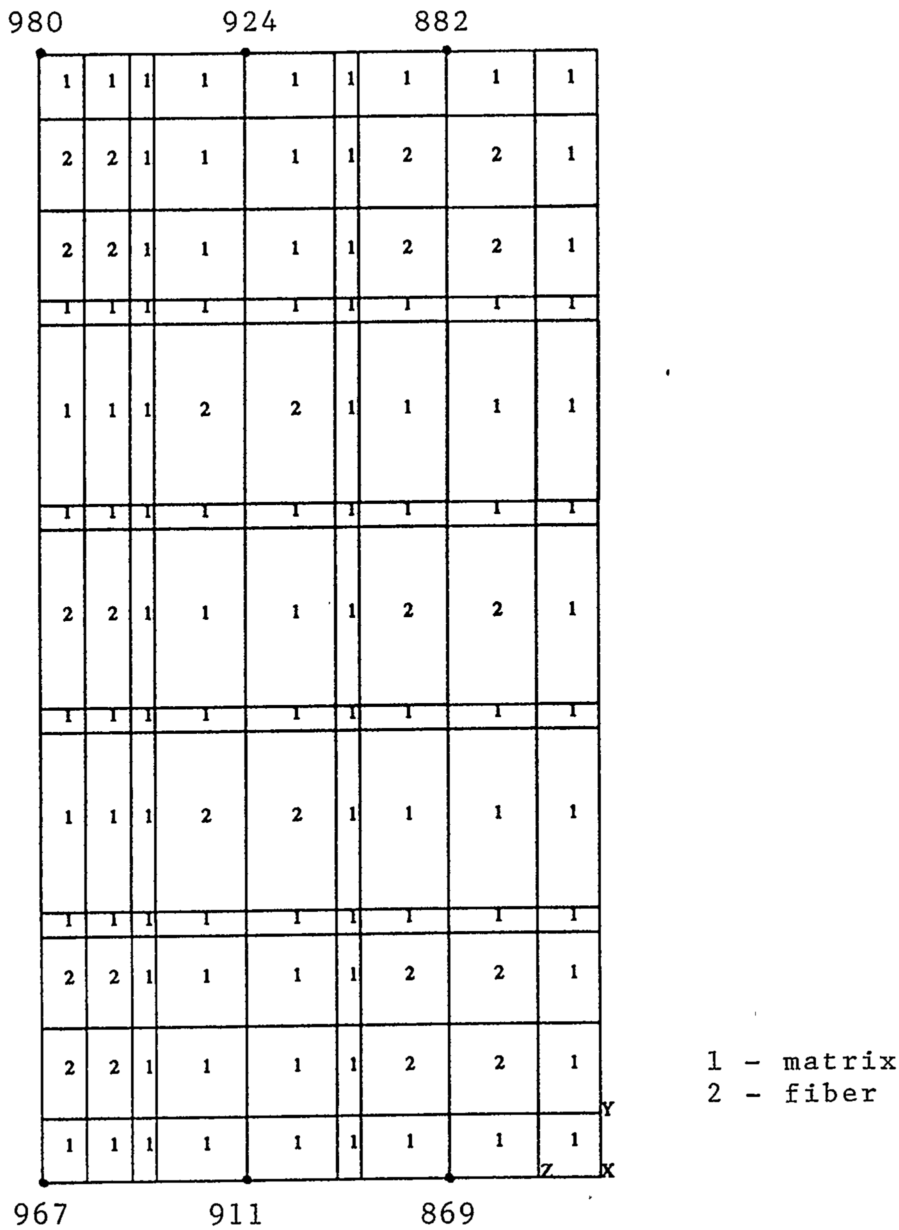

Figure 5.40: Finite element mesh for three-dimensional composite model (cross-sectional view).

the xy-plane, the loading stresses induced are in the x-direction. Stresses in y- and z-direction are Poisson stresses.

Stress S_x is plotted for both three-fiber and two-fiber sections in figures 5.41 to 5.43. Figures 5.41 and 5.43 simulate the stress distribution along the analysis lines AA'/EE' and CC' in the three fiber sections. Figure 5.42 simulates the Sx stress distribution along the analysis line BB'/DD' in the two fiber section. Stress distribution in the fibers in the three-fiber section is similar but higher than in the two-fiber section. It is opposite to that of 2-D analysis where maximum stress values in individual fibers occurred in two-fiber slices. This can be explained because the two-dimensional analysis is not representative since it does not take into account the effect of surrounding three fiber distribution. For example, a two-fiber slice analysis in figure 5.35 would not show the influence of three-fiber distribution surrounding it as in the real situation. As expected, for both two fiber and three fiber sections stresses in the matrix are low. Similar to two dimensional behaviour these stresses are linear and symmetrical about the neutral axis. Again the neutral axis coincides with the centroid. Overall, stresses in the matrix from three dimensional analysis are comparable to those from two dimensional analysis. For example, in figure 5.35 in the two

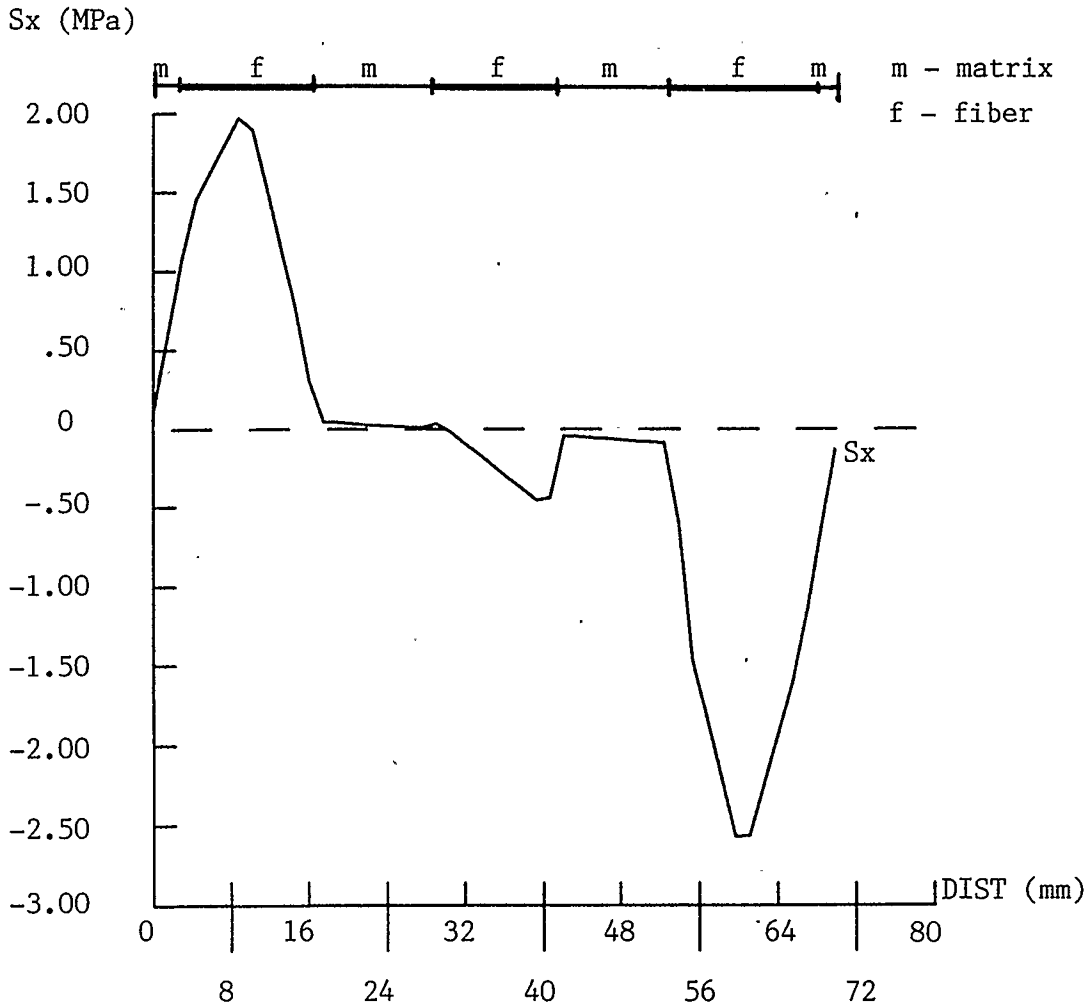

Figure 5.41: Sx along nodes 869 to 882 simulating analysis lines AA' and EE'.

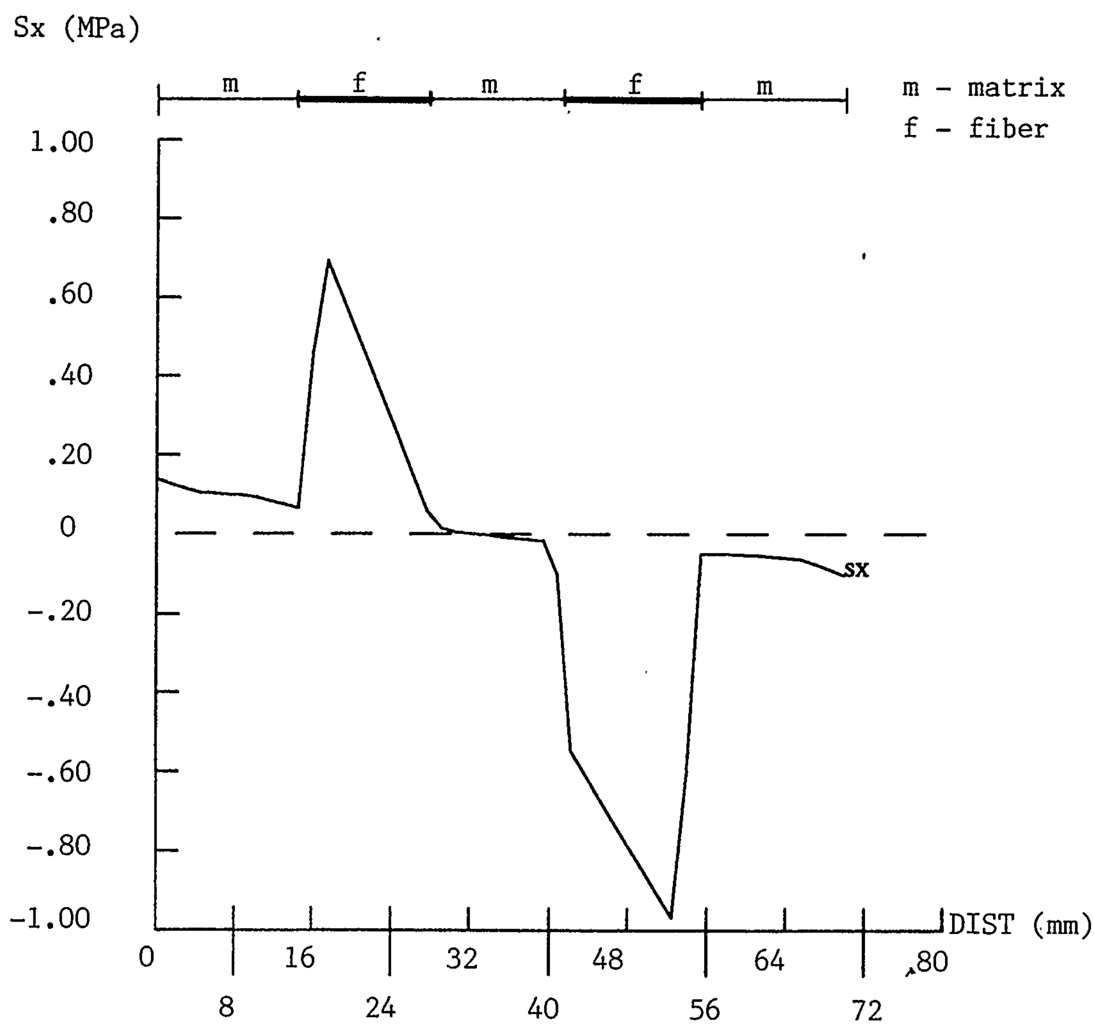

Figure 5.42: Sx along nodes 911 to 924 simulating analysis lines BB' and DD'.

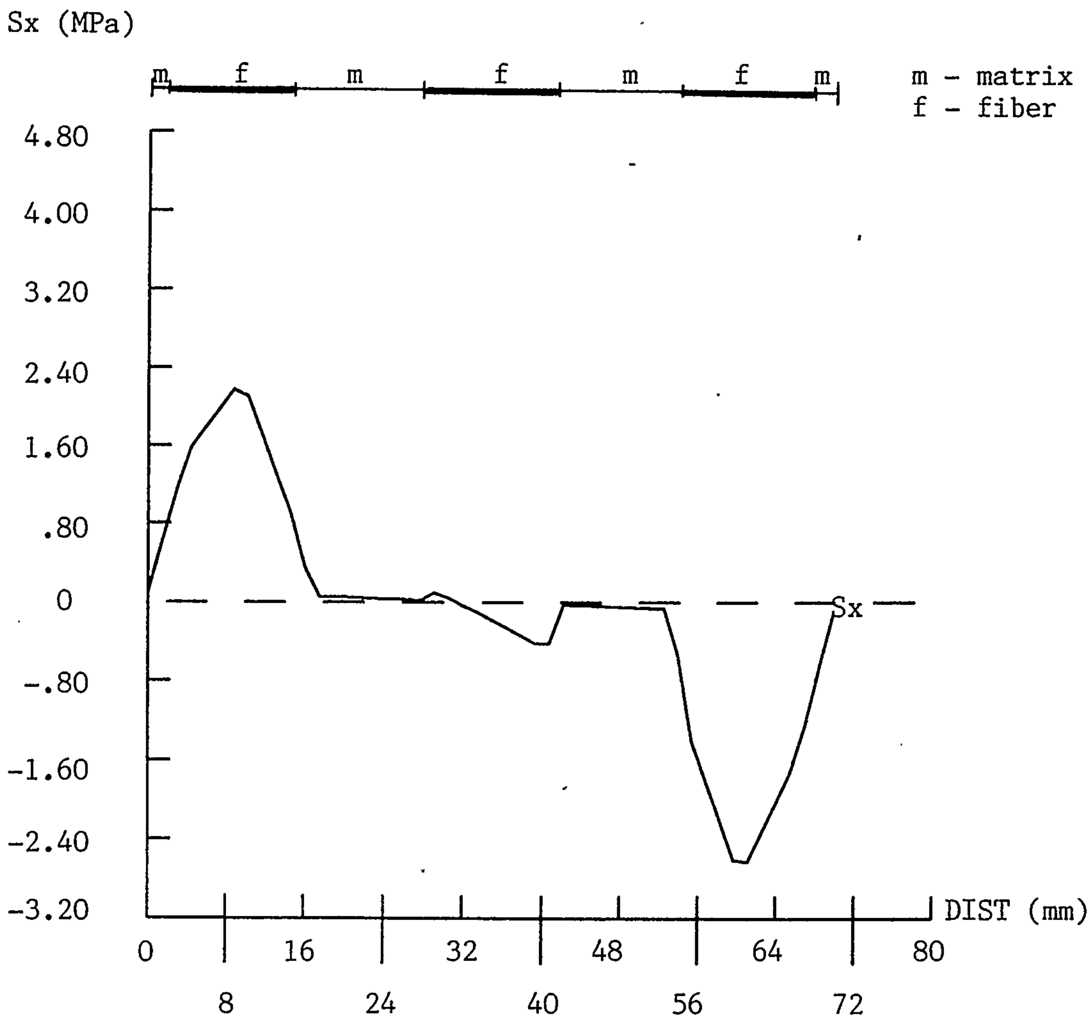

Figure 5.43: Sx along nodes 967 to 980 simulating the analysis line CC'.

fiber slice at the bottom free edge (node 7 or 8) S_x=100 kPa, where as in figure 5.42 in the two fiber section at node 967 $S_x \approx 115$ kPa. This indicates that stresses in the matrix for 2-D and 3-D analysis are comparable. Something that is clear from three-dimensional analysis is that three-fiber distribution does dominate the overall behaviour in the composite model.

Stresses S_{xy} are plotted in figures 5.44 to 5.46. Figures 5.44 and 5.46 show the stress distribution along the analysis lines AA'/EE' and CC' in the three fiber sections. Figure 5.45 shows the stress distribution along the analysis line BB'/DD' in the two fiber section. In both two fiber and three fiber sections the shear stress values are low in the matrix but much higher in the fibers. Also, as seen in figures 5.44 to 5.46, Sxy stress values are minimum in the center which is the neutral axis. This behaviour is opposite to that of homogeneous materials where the maximum shear stress occurs at the neutral axis. For the two fiber section in figure 5.45 shear stress distribution within the fibers is completely linear. These stress values are lower in the two fiber section as compared to the three fiber sections in figures 5.44 and 5.46.

Values for S_{xy} are low as compared to S_x. Observing figures

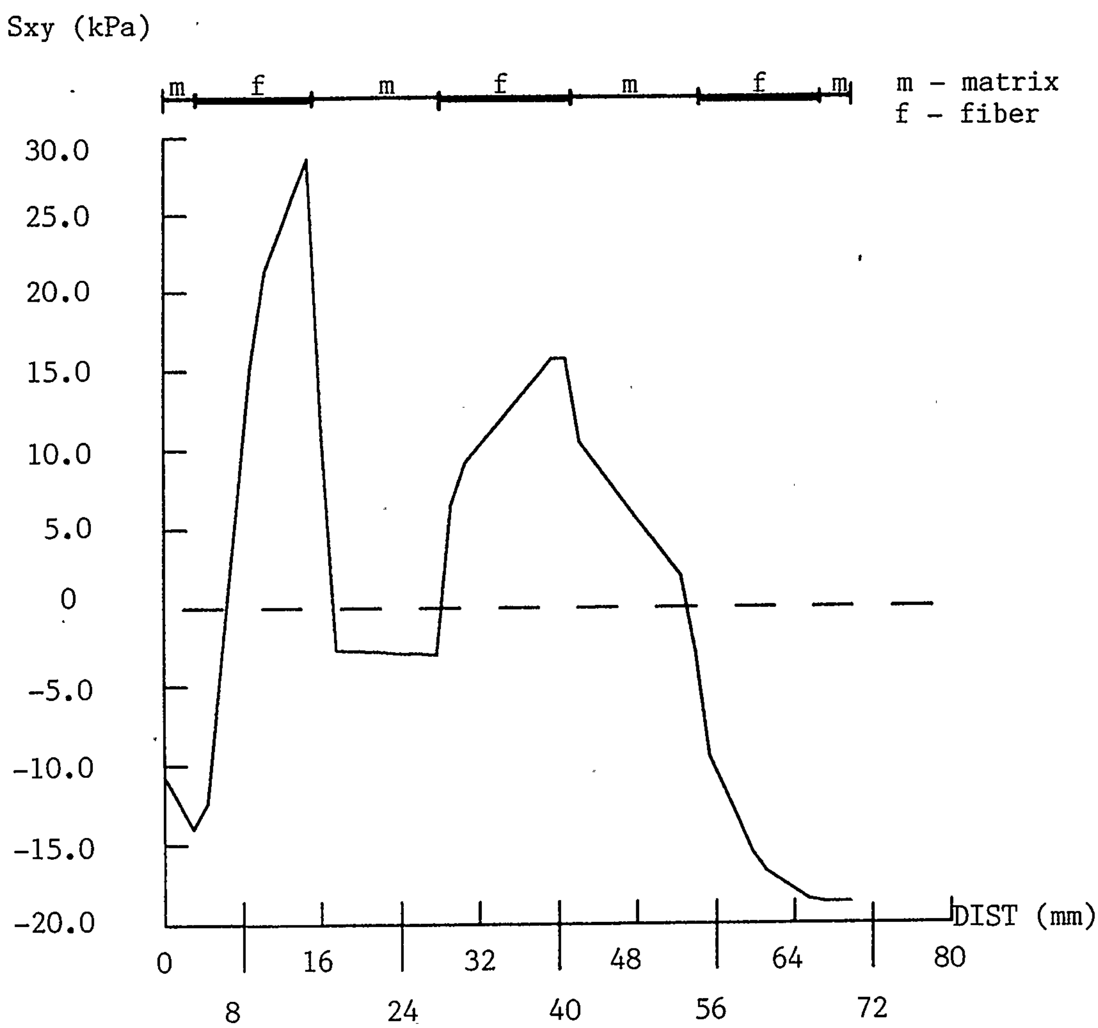

Figure 5.44: Sxy along nodes 869 to 882 simulating analysis lines AA' and EE'.

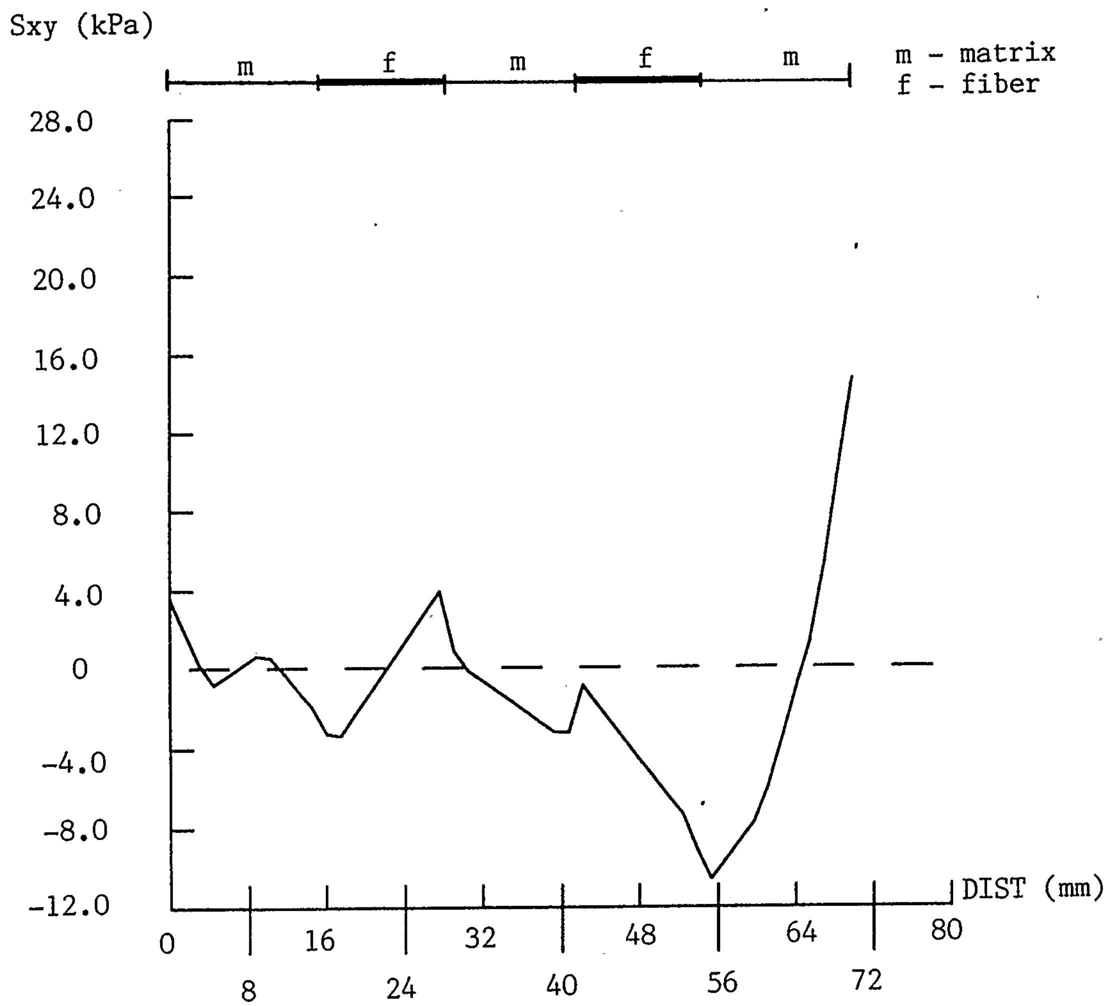

Figure 5.45: Sxy distribution along nodes 911 to 924 simulating the analysis lines BB' and DD'.

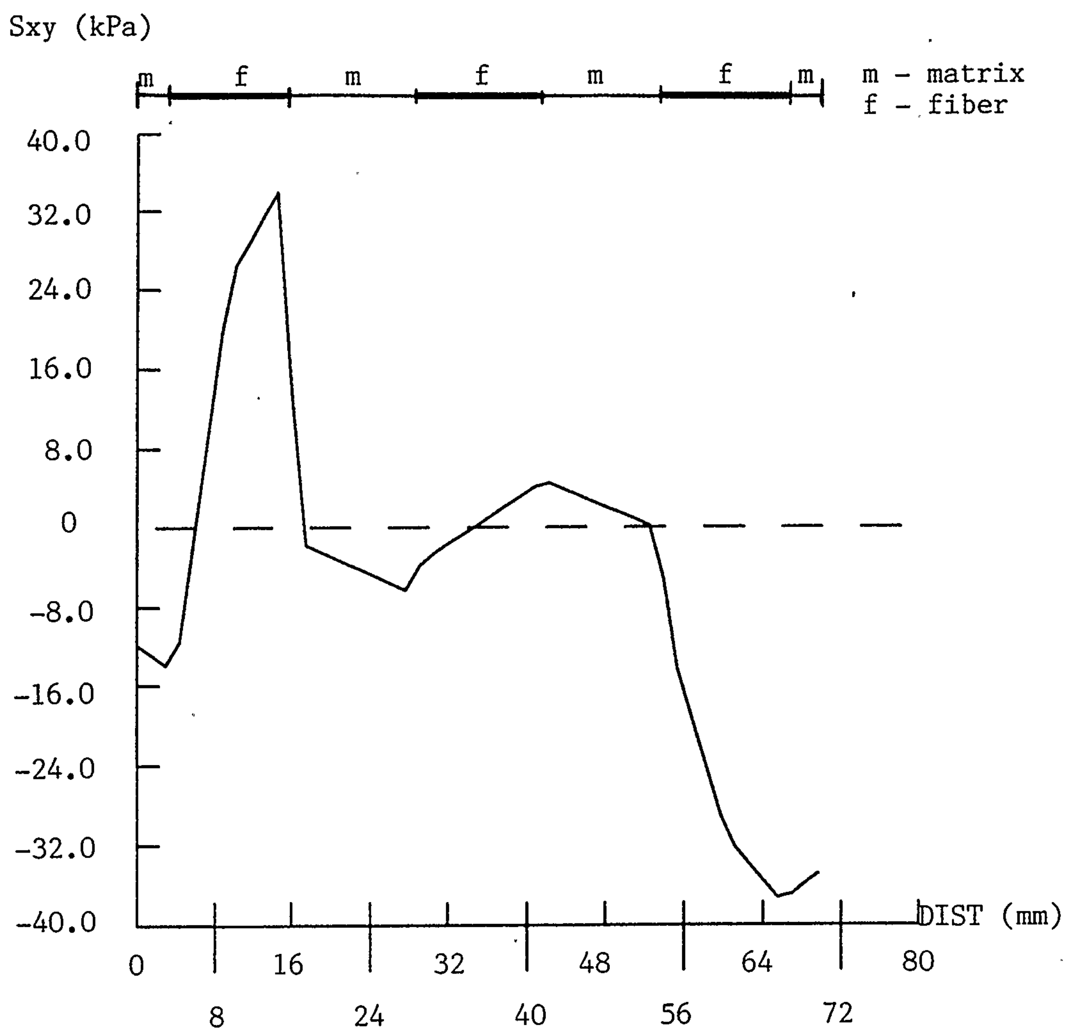

Figure 5.46: Sxy distribution along nodes 967 to 980 simulating the analysis line CC'.

5.44 to 5.46 it is clear that away from the top free edge S_{xy} is close to zero. This is consistent with the results obtained from the two-dimensional analysis. Most of the S_{xy} stress values are within one percent of the S_{xmax}. Stresses at the top edge may have been influenced by the stress concentrations in the loading plane.

Stress S_y is plotted in figures 5.47 to 5.49. Figures 5.47 and 5.49 show Sy stress distribution along the analysis lines AA'/EE' and CC' in the three fiber planes. Figure 5.48 shows the Sy stress distribution along the analysis line BB'/DD' in the two fiber plane. The Sy stress distribution is similar for both the two fiber and the three fiber sections. This stress is low along lines AA' and BB' but a little higher along line CC'. These stress values are minimum at the bottom free edge but increase steadily to the top free edge. The stress S_y is maximum at the top edge where theoretically it should be zero. It is in total deviation from results in the two-dimensional analysis. The reason for such an error is that the finite element mesh is not fine enough. For example, in figure 5.40 along nodes 911 to 924, at the top and bottom free edge in the finite element mesh only one element bridges the gap between the free edge and the fiber. Due to computation limitations finite element mesh cannot be further refined. Therefore,

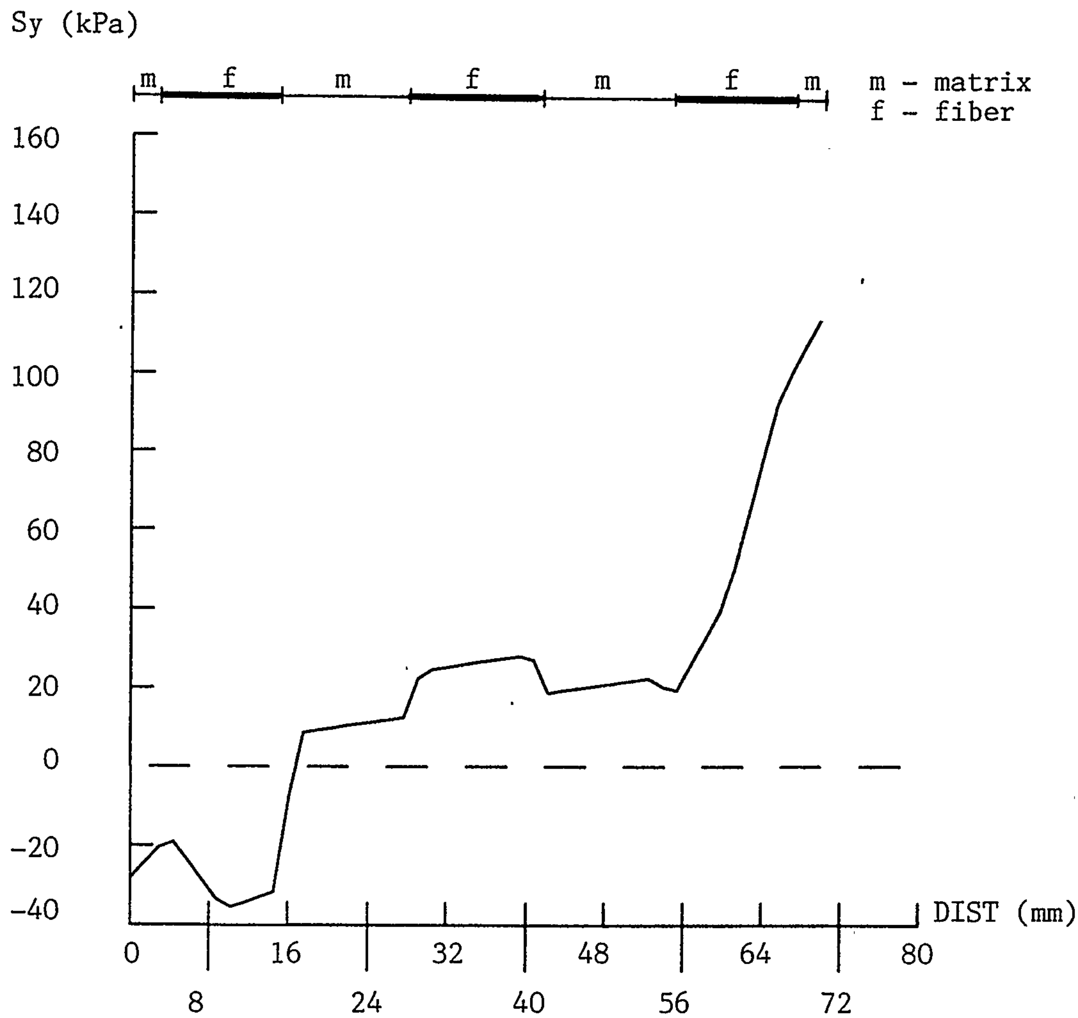

Figure 5.47: Sy distribution along nodes 869 to 882 simulating the analysis lines AA' and EE'.

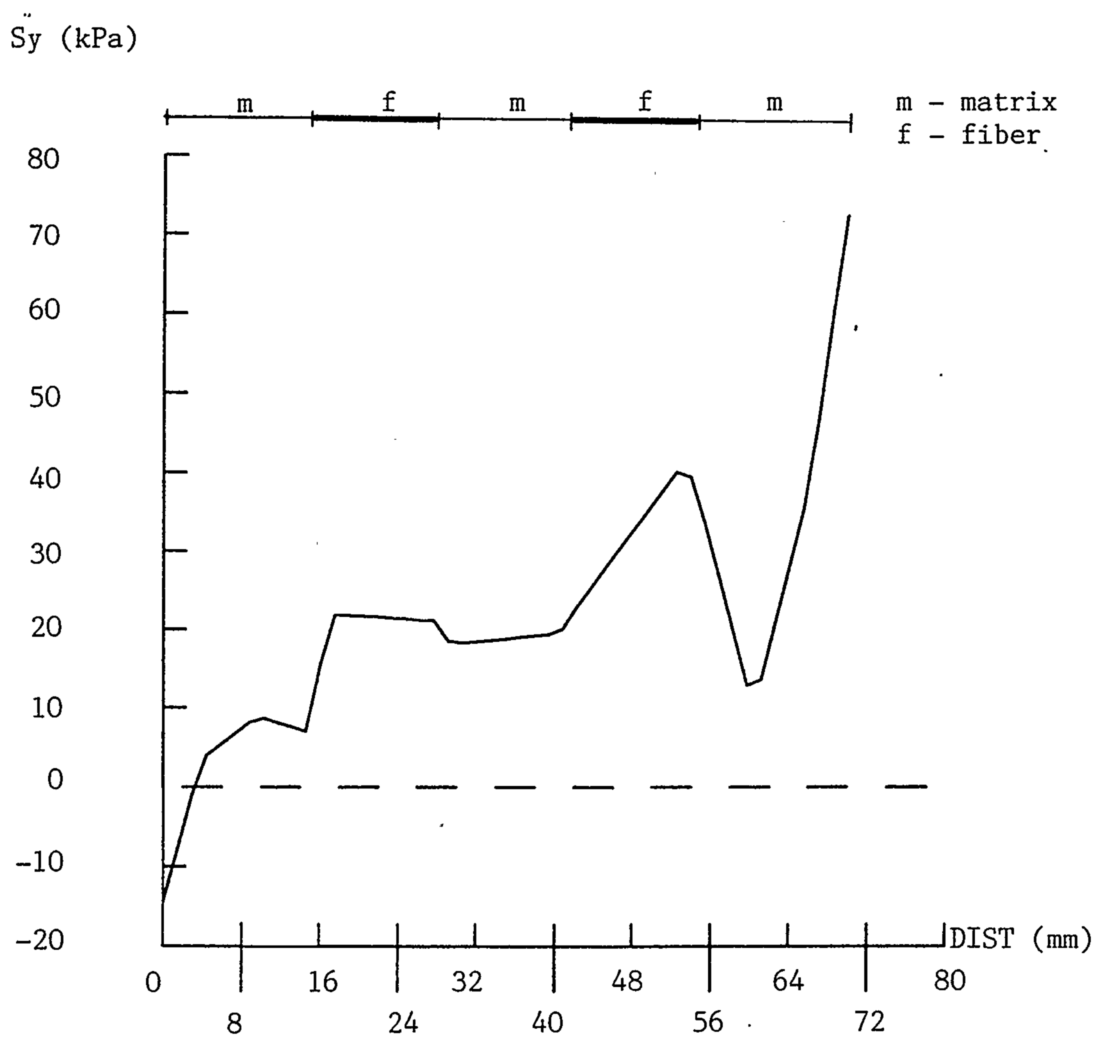

Figure 5.48: Sy distribution along nodes 911 to 924 simulating the analysis lines BB' and DD'.

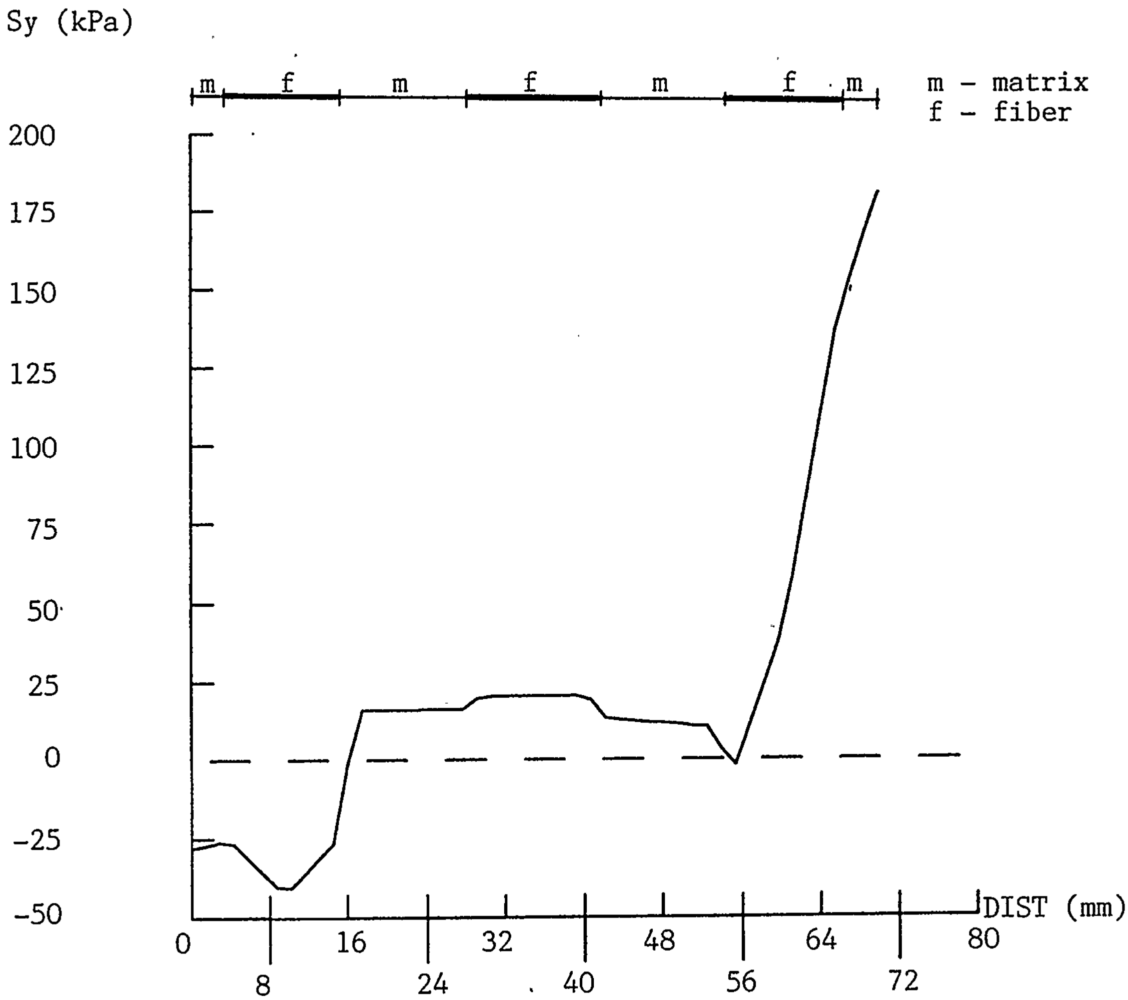

Figure 5.49: Sy distribution along nodes 967 to 980 simulating the analysis line CC'.

because of the averaging effect within an element the stress value appears higher than it actually should be.

The S_z stress distribution is plotted in figures 5.50 to 5.52. Figures 5.50 and 5.52 show the stress distribution along the analysis lines AA'/EE' and CC' in the three fiber sections. Figure 5.51 shows the stress distribution along the analysis line BB'/DD' in the two fiber section. This stress distribution is completely different for the two fiber and the three fiber sections. In the two fiber section the stress Sz is zero at the top free edge where as in the three fiber section it is maximum at that point. Observing figure 5.51, S_z stress values are less than one percent of S_{xmax}. Also, the stress distribution is linear in the bottom fiber but almost constant in the top fiber. In the three fiber sections the Sz stress distribution is linear in the top and the middle fiber. In figures 5.50 and 5.52 S_z values along analysis lines AA' and CC' oscillate about zero stress value. These oscillations diverge to a maximum stress value at the top free edge. The reason for the stresses appearing to be high along the top free edge could be the effect of loading points in that plane. In general, S_z stress distribution is negligible as compared to stress S_x.

The analysis carried out in sections 5.3.1 and 5.3.2 gives

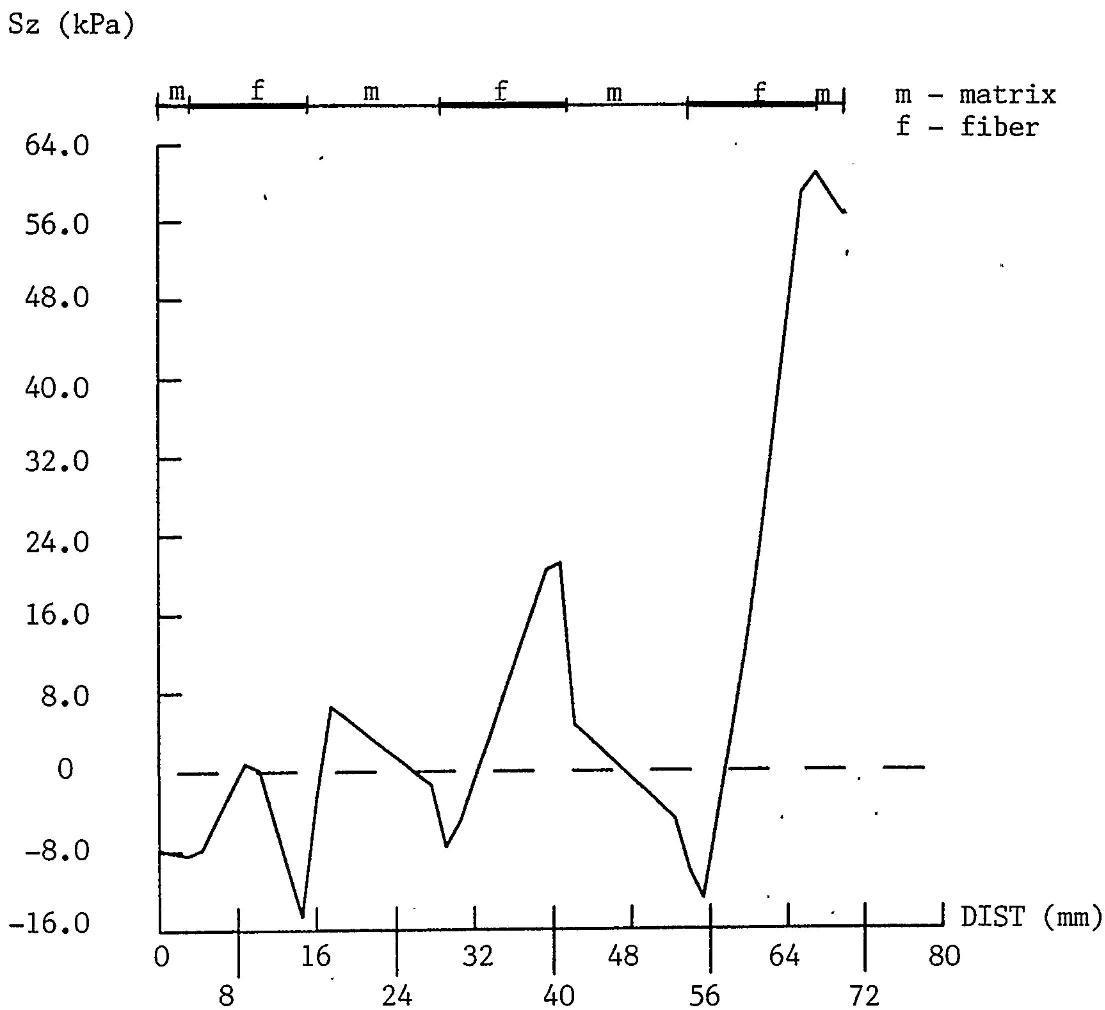

Figure 5.50: Sz distribution along nodes 869 to 882 simulating the analysis lines AA' and EE'.

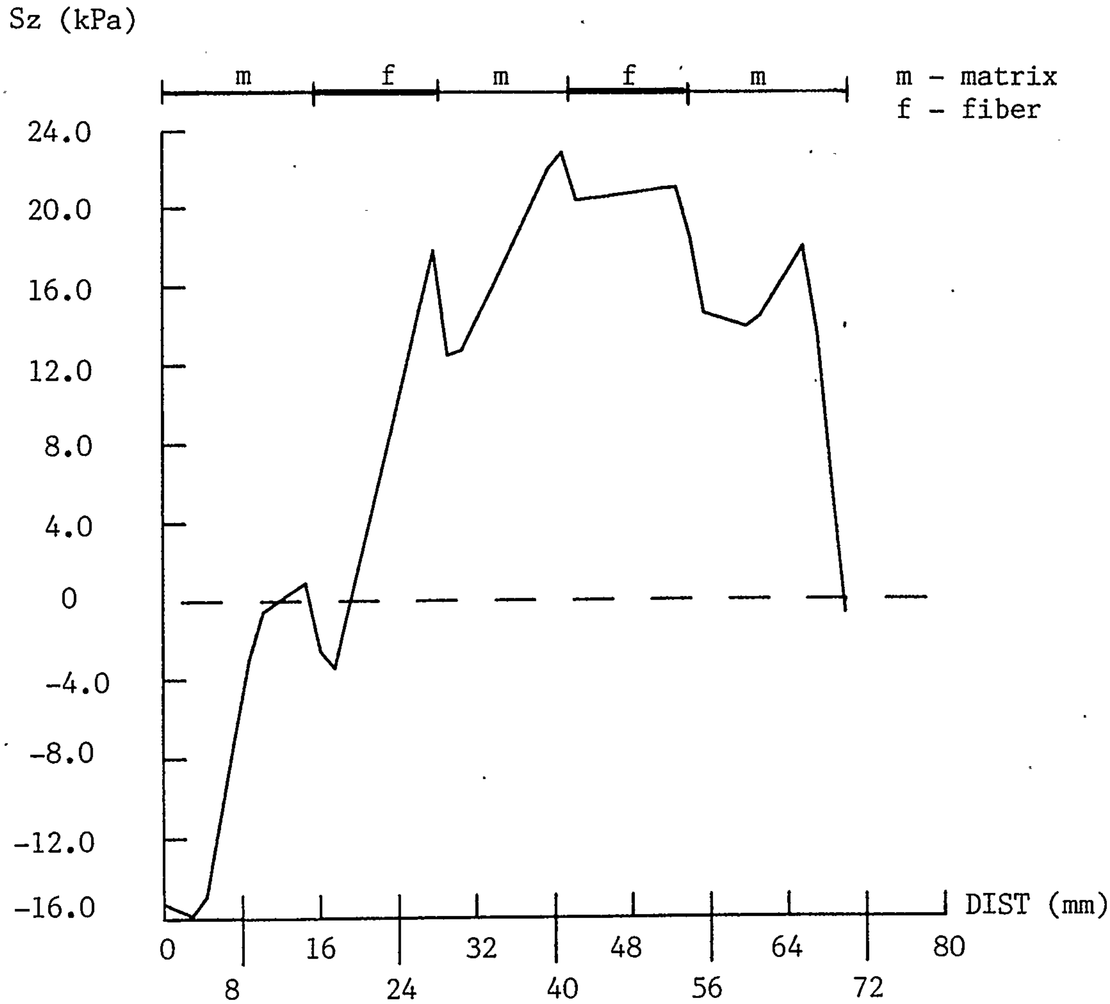

Figure 5.51: Sz distribution along nodes 911 to 924 simulating the analysis lines BB' and DD'.

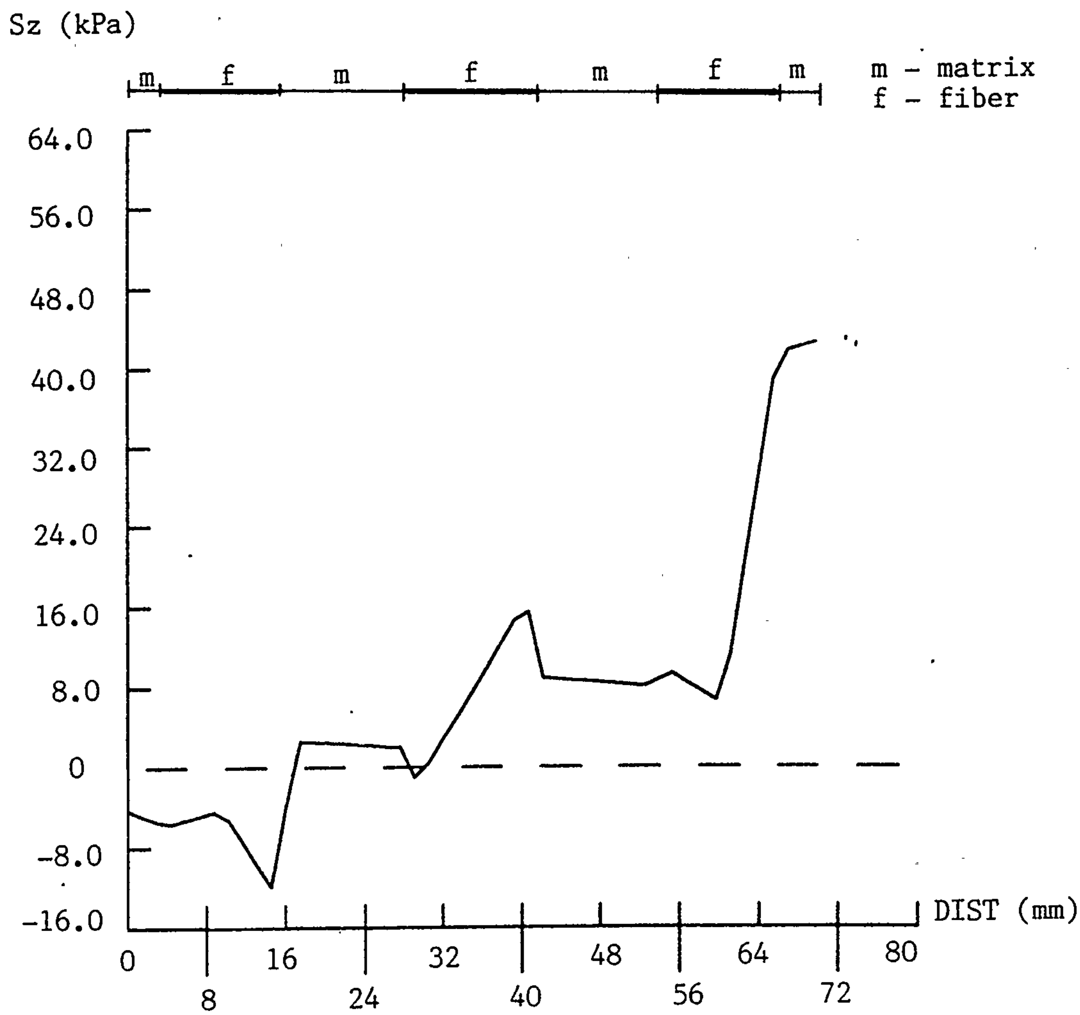

Figure 5.52: Sz distribution along nodes 967 to 980 simulating the analysis line CC'.

some indication of the overall behaviour of the fiber composite model. Three-dimensional finite element analysis indicates that the three fiber plane dominates the overall behaviour of the composite model. Stresses in the matrix are linear and symmetrical about the neutral axis. The neutral axis is found to coincide with the centroid for both two- and three-dimensional analysis. Under pure bending the shear stress is zero away from the stress concentration or loading points.

CHAPTER SIX

DISCUSSION

In the previous chapter results from photoelastic and finite element analysis were conducted separately. Quantitative results from finite element analysis are not directly applicable because of the approximations and simplifications made. However, qualitatively these results do offer some insight into the overall behaviour of the composite model under four-point bending. From the finite element results it can be inferred that:

i) majority of the load is taken up by the reinforcing fibers and the maximum stress occurs in the middle of the fibers.

ii) three-dimensional and two-dimensional results indicate that the neutral axis for the composite beam coincides with the neutral axis due to geometrical symmetry.

iii) the three fiber plane dominates the overall behaviour of the composite model, with nominal contribution resulting from the two fiber plane.

Similarities in the FEM results and photoelastic fringe pattern are easy to observe. Shear stress is zero along the analysis line for both methods. Secondly, in the two-dimensional study $\tau_{xy}(S_{xy})$ results are symmetrical about the analysis line and have opposite signs. This is in agreement with photoelastic results where the symmetrical fringe pattern about the analysis line has opposite signs for the shear stress. Before proceeding further, one point needs to be made clear, the FEM stress plots are for each individual stress component. Photoelastic fringe pattern contains a combination of σ_x, σ_y and τ_{xy} stress components. Therefore, when comparing the two results the above has to be kept in mind.

Since the photoelastic analysis does not show the stress distribution in the fibers the comparison is carried out for stresses in the matrix part. Comparing the maximum and minimum stress values it is observed that the low values occur in the matrix material. It is true for photoelastic analysis as well since the fringe order along the analysis line in the matrix is quite low. In the two fiber slice the stress σ_x can be evaluated at the free edge in the top matrix part through photoelastic analysis. Observing figure 5.17, $\sigma_y = 0$ at the top edge and the fringe order $N \simeq 1$.

This gives $\sigma_x \simeq 70$ kPa. Comparing the values for σ_x at the top edge for the two fiber slice:

Photoelastic analysis	$\simeq$ 59 kPa ($\simeq$9 psi)
3-D and 2-D two fiber plane	100-112 kPa
finite element analysis	(14.5-16.2 psi)
(fig. 5.42 and 5.36 respectively)	

To calculate the amount of load desired to stay in the elastic region, simple transformed section theory was applied. Using this theory the stresses were predicted for the same load. Stress σ_x at the top free edge was 103 kPa in the three fiber slice and 360 kPa in the two fiber slice. It is evident that the stress value for the two fiber slice is not comparable to the experimental value. There could basically be two reasons for this. First, the transformed section theory is not totally applicable to a fiber composite material.For example, in the case of reinforced concrete beam, reinforcing steel bars are in tension and the concrete in compression. However, in the present study the reinforcement is not limited to a region in tension or compression and therefore, the overall behaviour may or may not be symmetrical about the neutral axis. Secondly, since the calculation for the loads involved a two-dimensional approach, it does not represent the effects of reinforcement in the adjacent planes. This could be true as the evidence already discussed showed that the stress distribution in the two fiber plane is influenced by the dominating behaviour of the surrounding three fiber plane.

Similarities in the results from both methods indicate that the two techniques can be used in combination. However, for the required three-dimensional finite element results to be directly applicable a much more refined mesh has to be used to model the exact behaviour. The cross-section of the reinforcing fibers have to be modelled accurately rather than making any approximations. This means a large number of nodes and elements are needed which would require a super computer.

Results obtained from the photoleastic analysis indicate that a complete investigation of stresses within a fiber composite is possible provided some modifications are made. Firstly, the material for fibers should be replaced with one having some photoelastic properties. One option would be to use another resin/epoxy with photoelastic properties but a higher Young's modulus. The reinforcing rods could be cast out of this material prior to the casting of the complete composite model. This would result in a fiber composite model that is totally transparent with both the fiber and the matrix having photoelastic properties. This will enable a complete analysis of stresses in a composite model because discontinuities in the fringe orders would be eliminated. Such an analysis would include knowledge of stress distributions in both the matrix and the fibers. Knowing the stress distribution and the applied loads, it will be possible to derive a theoretical relationship from the experimental data.

For a homogeneous material under bending, stress is given by:

$$\sigma = \frac{M\ c}{I} \qquad (6.1)$$

Therefore, for a composite material the relation can be assumed as:

$$\sigma = k\ \frac{M\ c}{I} \qquad (6.2)$$

where, 'k' is an unknown constant to account for the non-homogeneous behaviour of the composite. Since, 'k' is the only unknown in eqn.(6.2), substituting for known values of stress and load it can be evaluated. Further, by testing composite models with fiber volume fraction varying from 30% to 60% will provide information on change of overall behaviour and in the value for 'k' for variation in fiber volume fraction.

In order to apply the results from the experimentation to the AS4/3501-6 graphite fiber composite, results have to be extrapolated down to the actual size of fibers. It means that scaling factors have to be established. It is proposed that fiber diameters of 3mm, 6mm and 25mm (1/8", 1/4" and 1") be used for a given fiber volume fraction. These sizes are based on physical and practical limitations for photoelastic analysis. Combined with the data from composite models with 12.7mm (1/2") diameter fibers, sufficient data points would be available for an extrapolation curve.

CHAPTER SEVEN

CONCLUSIONS

A three-dimensional stress distribution study was undertaken for photoelastic fiber composite models using photoelasticity and finite element techniques. Results from both of the methods were obtained and discussed. The following conclusions may be drawn:

1. Two identical photoelastic fiber composite models can be used for three-dimensional stress analysis. Slices removed from these models can be combined for overall analysis.

2. The three fiber plane dominates the overall behaviour of the composite model as compared to the two-fiber plane.

3. A material with photoelastic properties for reinforcement fibers should be used in the photoelastic composite model. This should provide for a complete analysis of three-dimensional stress distribution in a fiber composite model.

4. Based on experimental photoelastic analysis it is possible to derive a theoretical method of predicting stresses in the composite material under bending loads.

5. Results from photoelasticity and finite elements show good correlation. It indicates that the two techniques can be used in conjunction with each other for better results and accuracy.

6. Under pure bending, the shear stress, τ_{xy}, is zero in the matrix part of the fiber composite model.

7. Fringe pattern in the photoelastic material was very sensitive to the heat buildup during slicing and polishing. A constant stream of coolant lubrication has to be maintained for an unaffected fringe pattern.

8. Technique was developed for cutting composite photoelastic model without delamination along fibers.

9. The technique of photoelasticity proved to be a time consuming method. Thus, care must be taken in future work.

CHAPTER EIGHT

RECOMMENDATIONS

Preceeding work done can be considered as groundwork for future studies. Much needs to be done to understand the stress distribution inside a fiber composite. Future work has to be continued on composite photoelastic models. The scaling factors need to be investigated by using composite models with varying fiber diameters. All equipment and instrumentation is now in place for continuation of such work. This equipment and instrumentation was made specially for stress freezing methods and is able to withstand higher temperatures for extended periods of time.

It is recommended that a material with photoelastic properties be used for reinforcing fibers in the composite models. It is further recommended that composite models with fiber diameters of 3mm, 6mm and 25mm be used to establish scaling factors. The application of scaling factors and photoelastic experimental data should lead to a theoretical prediction method. Such a prediction equation/method could be verified by using an alternate loading method such as uniform pressure loading or three-point bending.

Other investigations that could be undertaken involve the study of stress distribution between fibers in a diagonal direction. This should help in understanding the influence of reinforcing fibers in adjacent planes on the stresses in the matrix material.

REFERENCES

1. J.W. Dally and W.F. Riley,"EXPERIMENTAL STRESS ANALYSIS", McGraw-Hill (1965).
2. S. Redner,"PHOTOELASTICITY", John Willy (1968).
3. H.T. Jessop and F.C. Harris,"PHOTOELASTICITY - Principles and Methods", Dover Publications (New York), 1949.
4. B.D. Agarwal and L.J. Broutman,"Analysis and Performance of Fiber Composites", John Willy (New York), 1980.
5. I. Le May,"Principles of Mechanical Metallurgy", Elsevier, New York, Oxford, 1980.
6. M.M. Frocht and R. Guernsey Jr.,"A Special Investigation to Develop a General Method for Three-Dimensional Photoelastic Stress Analysis", Selected Papers of M.M. Frocht On Photoelasticity, Pergamon Press, 1969, pp.233-270.
7. K.A. Jacob and K. Chandrashekhara,"Photoelastic Analysis of a Composite Prism Subjected to Partial Compression," J. of Applied Mechanics, vol. 45 no 2, June 1978, pp.436-440.
8. H.Pih and C.E. Knight,"Photoelastic Analysis of Anisotropic Fiber-reinforced Composites", J. of Composite Materials, vol 3, Jan. 1969, pp.94-107.

9. R. C. Sampson,"A Stress-optic Law for Photoelastic Analysis of Orthotropic Composites", Exp. Mechanics, vol 10 no 5, May 1970, pp.210-215.

10. C. W. Bert,"Theory of Photoelasticity for Birefringent Filamentary Composites", Fibre Science and Technology, vol 5 1972, pp. 165-171.

11. J. Cernosek,"On Photoelastic Response of Composites", Exp. Mechanics, vol 11 no 8, Sept. 1975, pp.354-357.

12. R.B. Pipes and J.W. Dally,"On the Fiber-reinforced Birefringent Composite Materials", Exp. Mechanics, August 1973, pp.348-349.

13. C.E. Knight and H. Pih,"Orthotropic Stress-optic Law for Plane Stress Photoelasticity of Composite Materials", Fibre Science and Technology, vol 9, 1976, pp.297-313.

14. H.T. Hahn and D.H. Morris,"Anisotropic Photoelasticity with Application to Composites", Fibre Science and Technology, vol 11 1978, pp.113-125.

15. B.D. Agarwal and S.K. Chaturvedi,"Improved Birefringent Composites and Assessment of Photoelastic Theories", Fibre Science and Technology, vol 11 1978, pp.399-412.

16. E.E. Gdoutos,"Isochromatic Patterns in a Plate with a Rigid Fibre Inclusion", Fibre Science and Technology, vol 15 1981, pp.299-311.

17. J.W. Dally and R. Prabhakaran, "Photo-orthotropic-Elasticity", Experimental Mechanics, vol 11 no 8, Aug. 1971, pp.346-356.

18. R.G. Craig, M.J. Gutzwiller, R.H. Lee and E.O. Stitz,"A Composite Three-dimensional Photoelastic Method", Experimental Mechanics, vol 17 no 11, Nov. 1977. pp.433-438.

19. K. Chandrashekhara, K.A. jacob and R. Prabhakaran, "Towards Stress Freezing in Birefringent Orthotropic Composite Models", Exp. Mechanics, vol 17 no 8, August 1977. pp.317-320.

20. D.R. Sutliff and H. Pih,"Three-dimensional Scattered-light Stress Analysis of Discontinuous Fibre-reinforced Composites", Exp. Mechanics, vol 13 no 7, July 1973. pp.294-298.

21. L.B. Greszczuk,"Interfiber Stresses in Filamentary Composites", AIAA Journal, vol 9 no 7, July 1971. pp.1274-1280.

22. R.H. Marloff and I.M. Daniel,"Three-dimensional Photoelastic Analysis of a Fiber-reinforced Composite Model", Exp. Mechanics, April 1969. pp.156-162.

23. D.F. Adams and D.R. Doner,"Transverse Normal Loading of a Unidirectional Composite", Journal of Composite Materials, vol 7 1967. pp.152-164.

24. I.M. Daniel,"Photoelastic Investigation of Composites," Composite Materials, vol 2 1974, pp.433-489.

25. J. Hancock,"Residual Stresses In The Photoelastic Analysis Of Composite Material", STRAIN, vol 11 no 4, 1975. pp.174-175.

26. H. Pih and D.R. Sutliff,"Effect of Fiber End, Fiber Orientation and Spacing In Composite Materials", Composite Materials, 5th Southeastern Conference On Theoretical and Applied Mechanics, 1970-71. pp.883-913.

27. A.J. Durelli, V.J. Parks, H.C. Fend and F. Chiang,"Strains and Stresses in Matrices With Inserts", Catholic Uni. of America Report, contract No. Nonr2249(06), May 1967.

28. J.G. Goree,"In-Plane Loading in an Elastic Matrix Containing Two Cylindrical Inclusions", Journal of Composite Materials, vol.1 1967. pp.404-412.

APPENDIX A

Table A.1: Properties of materials tested at 116 C.

Material	Young's Modulus (ksi)	Yield Strength (psi)	Tensile Strength (psi)
Matrix:			
PLM-4	2.5	280	280
Fiber:			
Nylon 6-6	40-45	2850-3300	4900-5250
Nylon 101	50.4	4300-4400	4900-5000
Nylatron GS	64-66	2000	4000
Teflon	Melted at 116 C.		

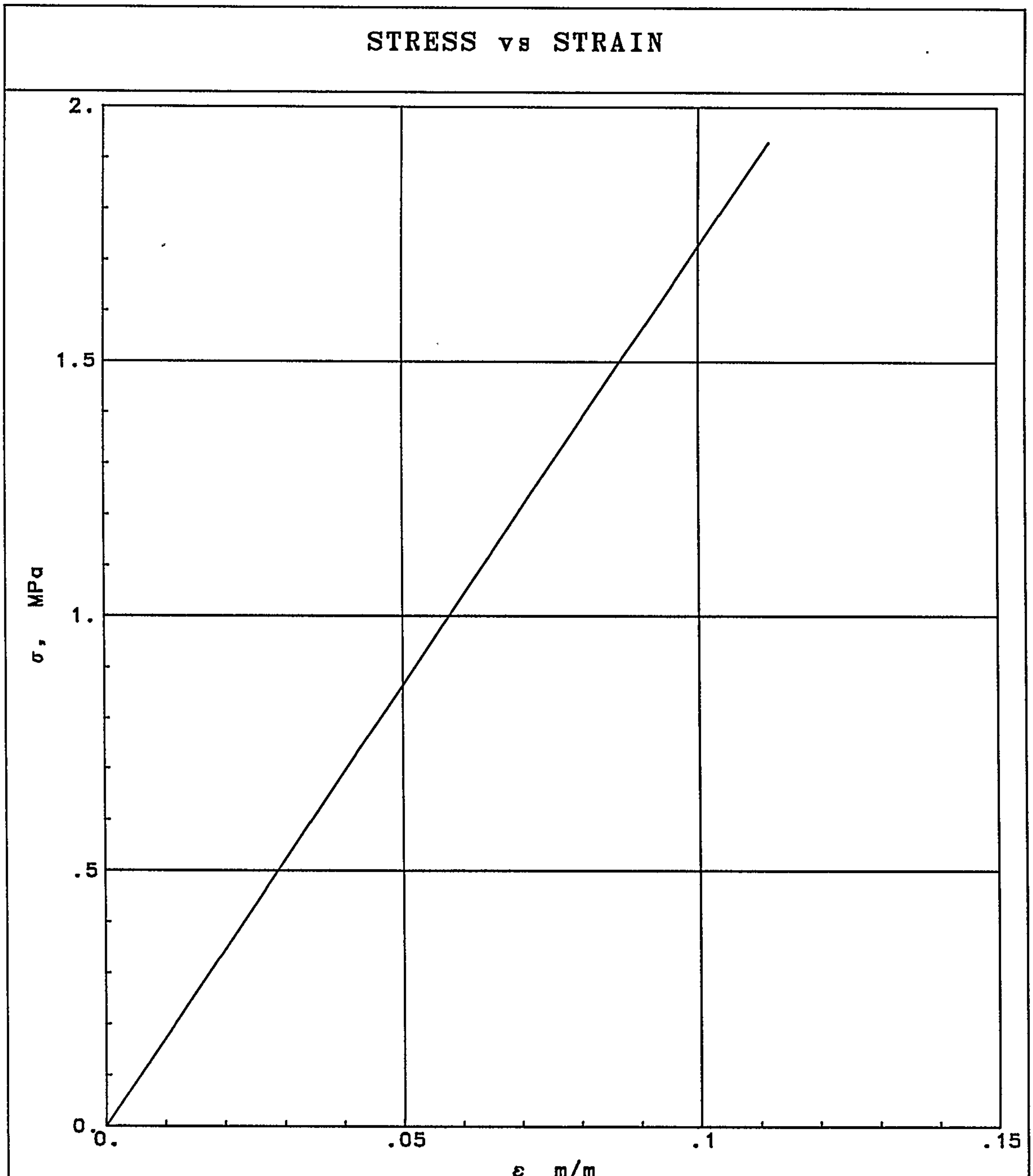

Experimental σ-ε diagram for PLM-4 resin at 116C.

FIGURE A.1

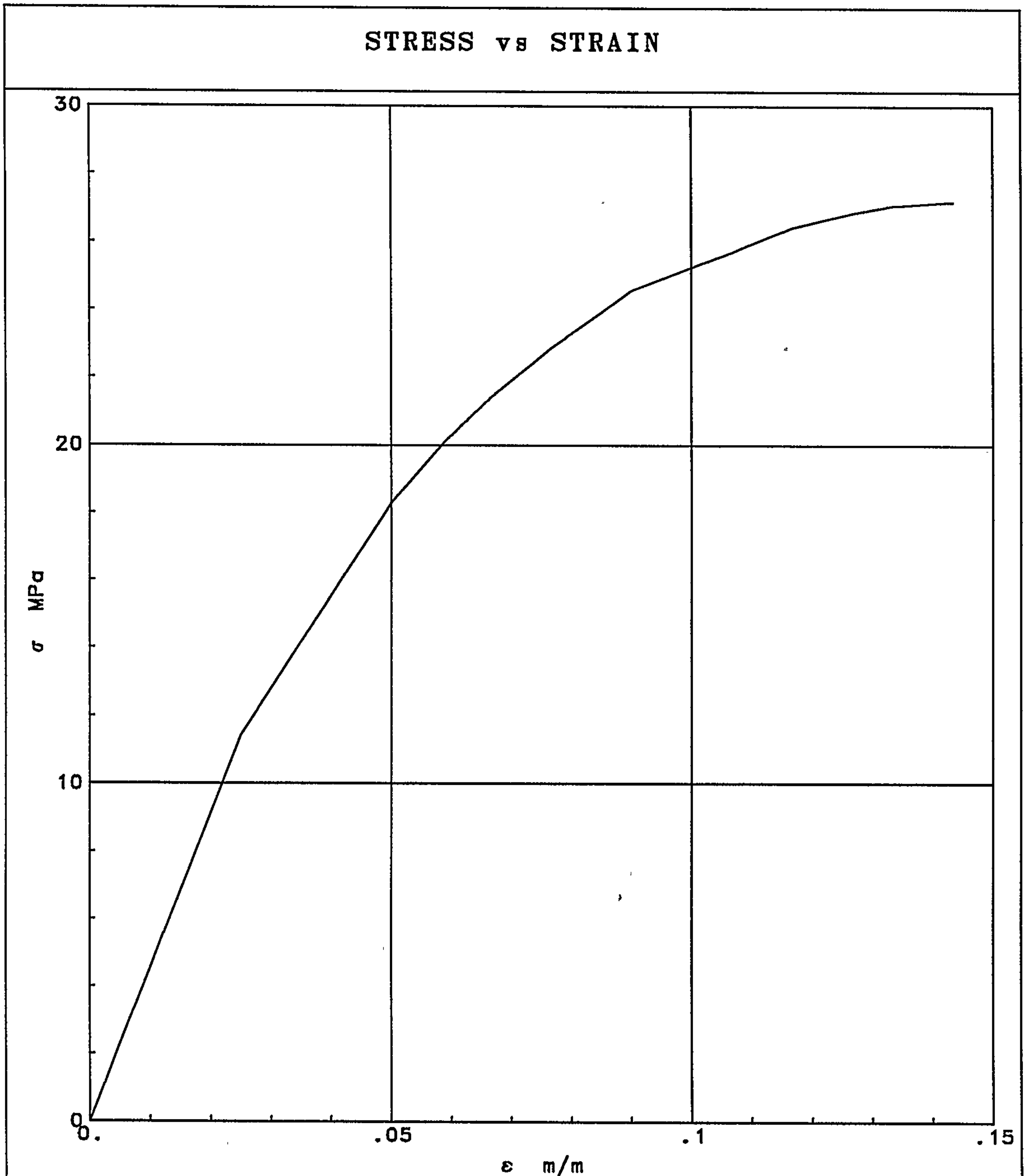

Experimental σ–ε diagram for Nylatron GS rods at 116C
*Upto the yield strength.

FIGURE A.2

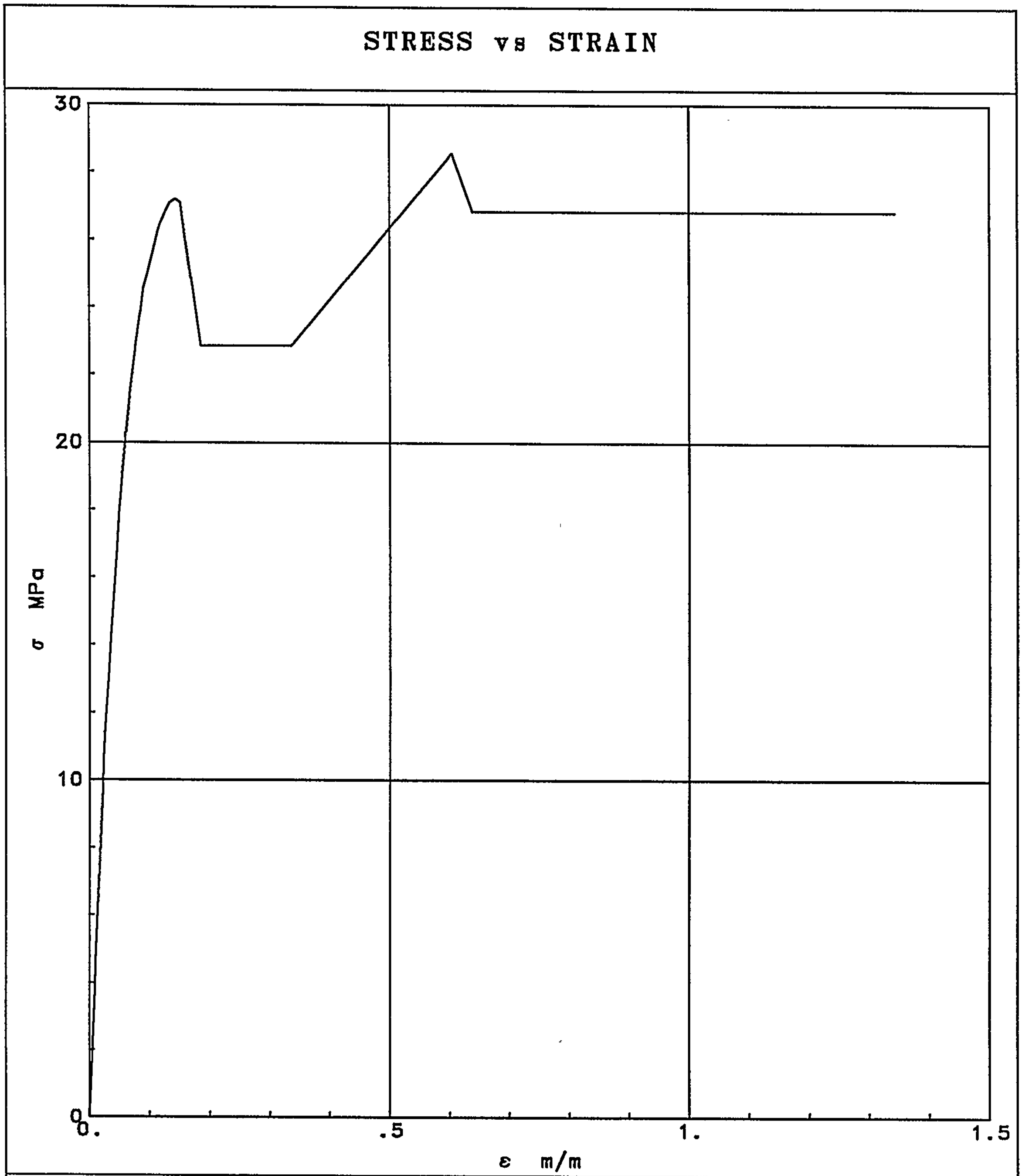

Experimental σ-ε diagram for Nylatron GS rods at 116C

※Upto the final fracture strain.

FIGURE A.3

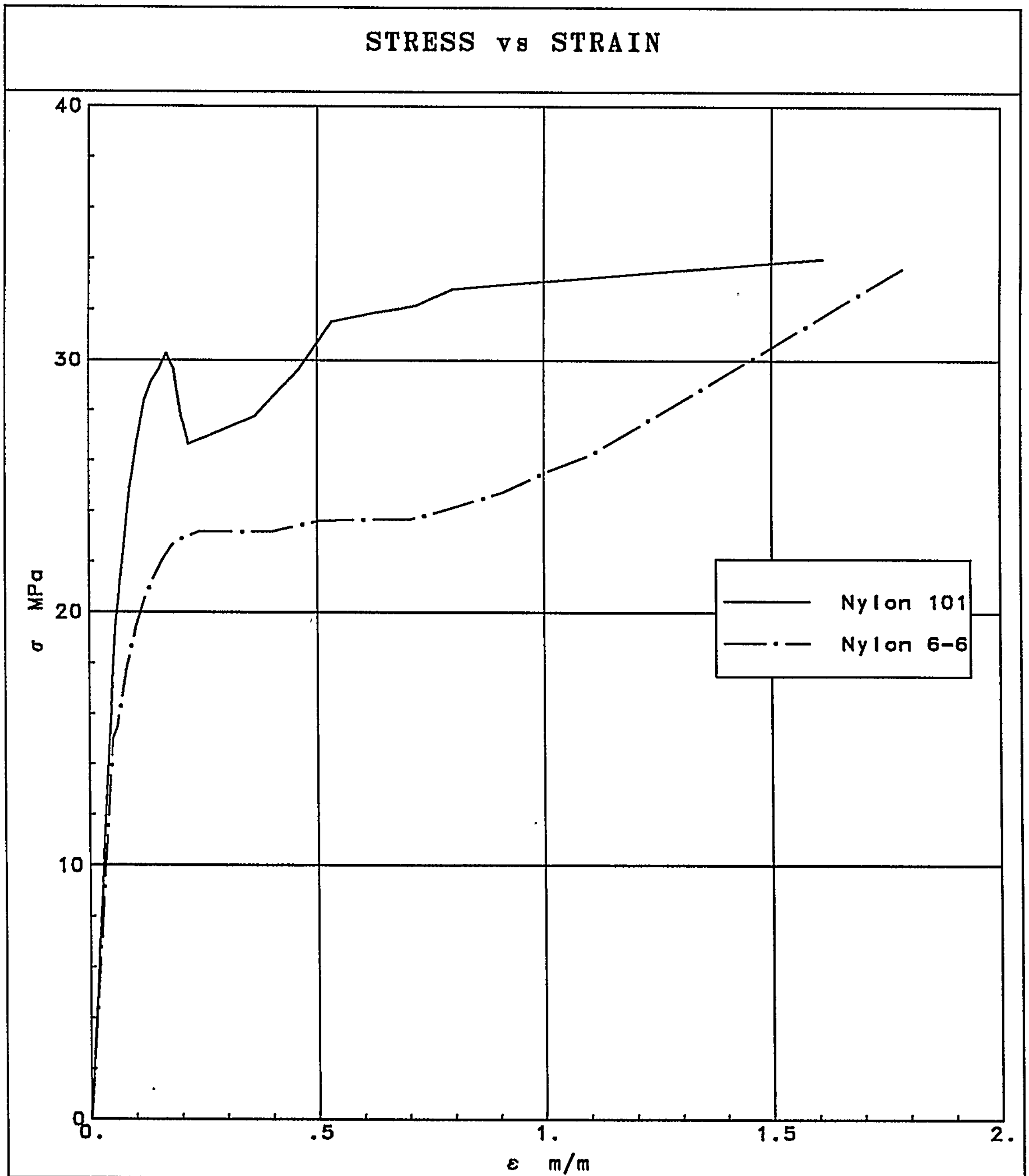

Experimental σ-ε diagram for Nylon rods at 116C

FIGURE A.4

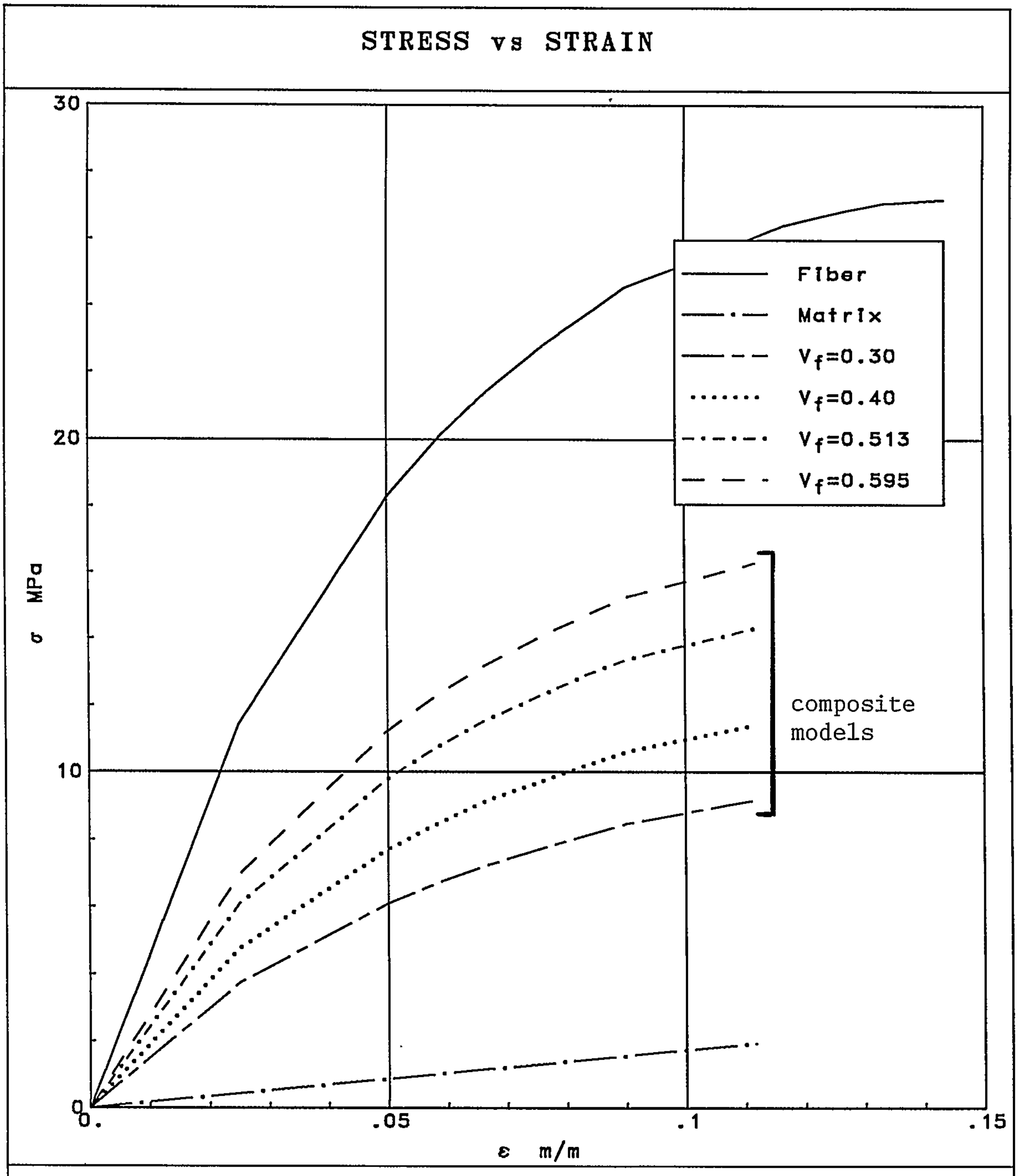

σ–ε diagram for photoelastic composite models at 116C

*Composite model strength based on equation 2.6.

**Matrix and fiber curves are based on experimental data.

FIGURE A.5

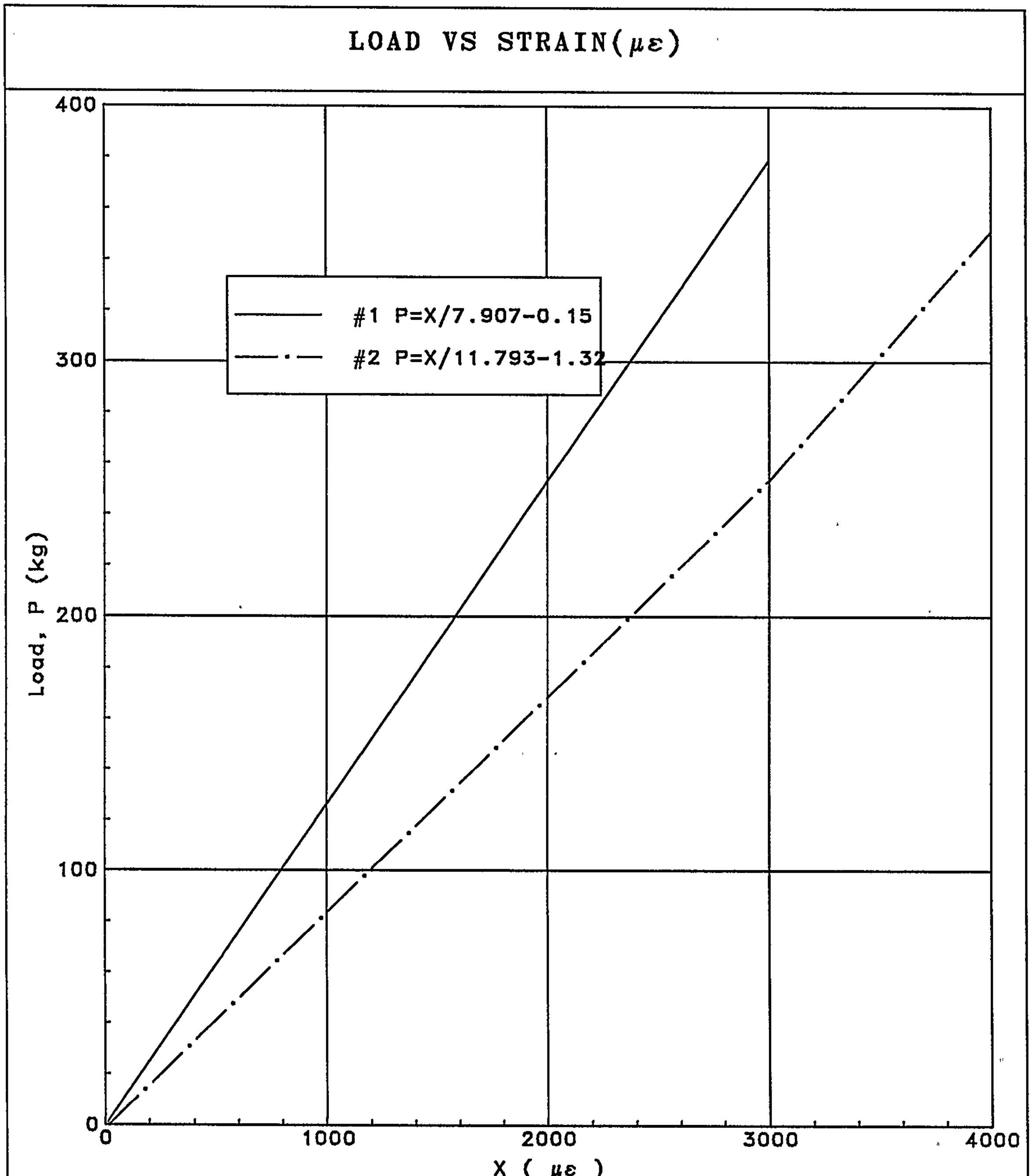

Figure A.6: Calibration curve for load cells.

*Load cells marked #1 & #2 are identical except for the sensitivity.

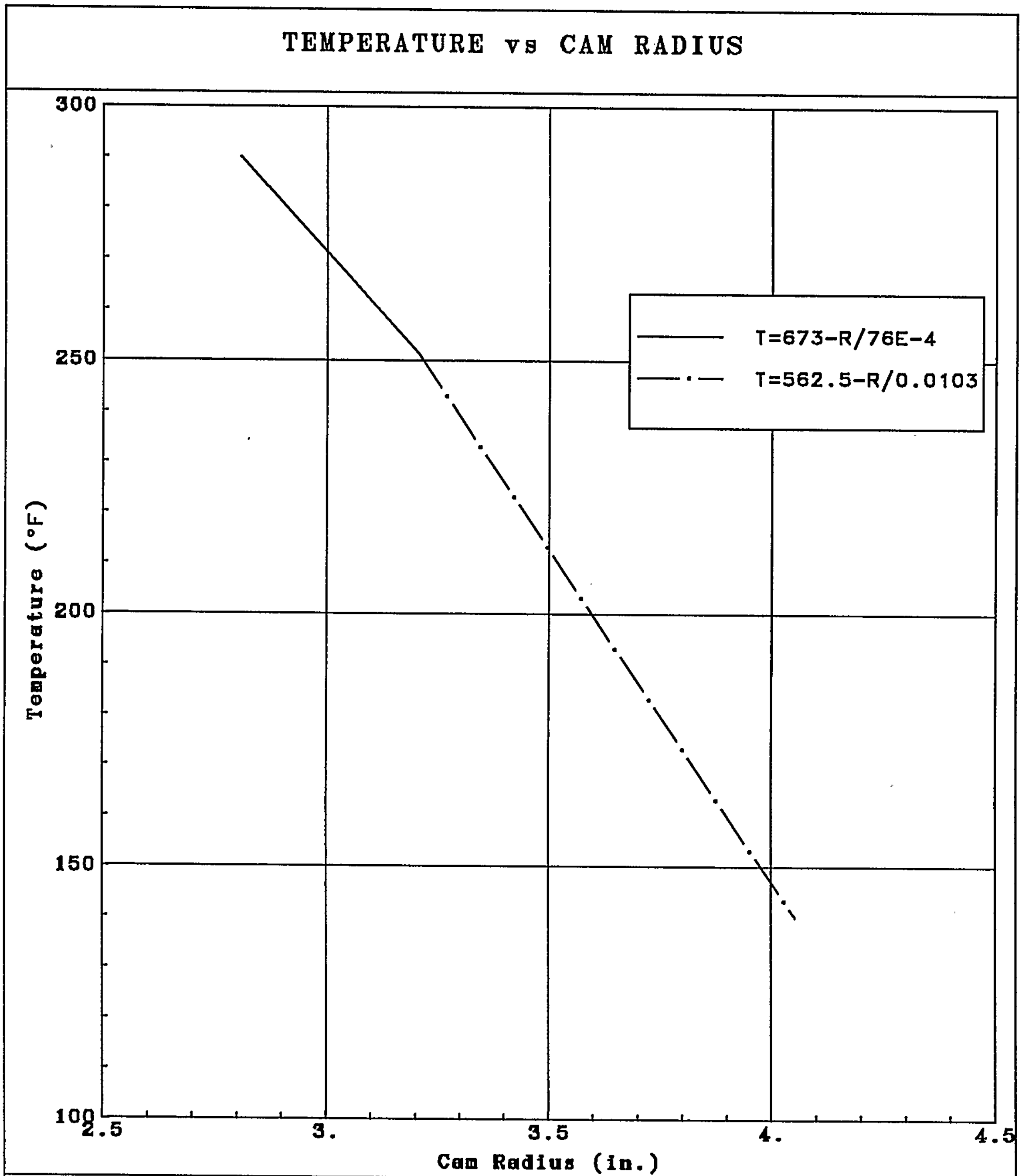

Figure A.7: Calibration curves for Blue-M furnace.